UNIVERSITÀ DEGLI STUDI DI PAVIA

DIPARTIMENTO DI INGEGNERIA
INDUSTRIALE E DELL'INFORMAZIONE

DOTTORATO DI RICERCA IN
INGEGNERIA ELETTRONICA, INFORMATICA ED ELETTRICA

Study and realization of integrated lab-on-chip micro-opto-acousto-fluidic systems

PhD candidate:
Valerio Vitali

Supervisor:
Prof. Paolo Minzioni

CICLO XXXII A.A. 2018/2019

Contents

Introduction

Over the past twenty years, microfluidic techniques and lab-on-chip (LoC) devices have raised a significant interest in the scientific community and opened new scenarios in many different research fields. This success is due to the inherent advantages of LoC systems over conventional technologies and to their ability to handle a significantly small sample volume. Moreover, the great advances occurred in the fields of micromachining and microfabrication technologies currently allow integrating multiple functionalities within a single chip, thanks to the inclusion of different sensors and actuation mechanisms, such as those based on dielectrophoresis, optical, acoustic and magnetic forces. Microfluidics successfully permeated into many different research areas, with particular attention being paid to the development of LoC devices for biological and chemical applications. The capability of working with reduced reagent volumes and parallel operations in the same microfluidic platform opened new perspectives in the field of analytical chemistry. Regarding biophysics and biology, the inherent micro-size characteristic of these devices offers a natural environment to detect, manipulate and even analyze biological samples at single cell level. Another scientific field which has strongly benefited from the advantages offered by microfluidics is rheology. The study of the rheological properties is of essential importance in different fields, ranging from industrial products development to basic research. Assessing the different responses of a material to an external perturbation (viscosity, elasticity, yield stress…) is particularly important not only to fine tune the material response to external conditions, but even to provide a significant insight about its structure, properties and microscale structural organization. The viscoelastic properties of a material can be measured by means of high-precision conventional devices called rheometers, for which a sample consumption of few mL is required. Nevertheless, during the last decades, an increasing interest has been shown to materials requiring to fully characterize very small sample quantities due to reasons such as low availability of precious and biological samples, thus pushing for the development of new techniques able to analyze sub-μL sample volumes with high reliability. This kind of analysis, commonly identified as *microrheology*, is attracting a significant attention in the fields of bio-based and bio-inspired materials study. The typical approach employed in microrheology is to exploit micrometer-sized or nanometer-sized beads dispersed in the material under test, which act as tracers. By monitoring the movement of the tracers, simply due to Brownian motion (passive microrheology) or as a result of an externally applied perturbation (active microrheology), it is possible to determine the viscoelastic properties of the sample under study. In addition to the low sample consumption, another peculiar advantage of microrheology is the capability of investigating heterogeneous

samples as the experiments are carried out with a local probe in a limited region. Microrheology commonly relies on atomic force microscopy, optical or magnetic forces for trapping and manipulating the position of the tracers in the sample under test. Regarding the use of optical forces, microscope-based single-beam optical tweezers have been largely used for materials rheological study and represent nowadays the most common microrheological technique, mainly due to their versatility and relatively easy implementation. Optical tweezers have been largely adopted both in passive and active microrheological measurements on a wide range of materials. The use of optical tweezers is getting more and more important even for *in vivo* measurements in cells and biological samples. Despite all the recent great advances, there are still some main issues which deserve to be addressed in order to further increase the potentiality and the applications of microrheology. First of all, optical tweezers allow applying forces in a restricted range, which is not large enough for investigating all the situations of interest for microrheology. Specifically, the study of the nonlinear response of complex media and of particular classes of viscoelastic materials (e.g. yield stress fluids) requires the application of high forces, which cannot be achieved with conventional single-beam optical tweezers. Moreover, microrheological measurements performed by means of single-beam optical tweezers require a careful alignment of the optical components and lack the integration of the optical and microfluidic part (i.e. the sample chamber filled with the medium to be measured).

In this thesis a fully integrated approach to microrheology exploiting a microfluidic chip and dual beam optical tweezers is proposed. Such an approach is really beneficial in terms of different aspects such as a good calibration and measurement repeatability and stability since no alignment procedure is required. The integrated system here proposed and investigated allows carrying out active microrheological measurements with the application of higher forces when compared to single-beam optical tweezers. The high-level of integration ensures all the advantages of microrheology such as a reduced sample consumption and allows obtaining a stable optical trapping in a large set of conditions. Moreover, the microfluidic approach opens the way to the integration of different types of actuation mechanisms, such as those based on acoustic forces, which have been exploited in the here presented system to easily trap the tracers dispersed in the fluid under test. All these features make the proposed optofluidic microrheometer particularly well suited for studying the linear and nonlinear properties of complex materials. The objective of this thesis work was therefore the realization of an integrated microrheometer, able to measure a wide range of materials (from water and soft gels to stiffer materials), in different rheological regimes (linear and nonlinear) and by accessing a wide range of optical forces, frequencies and temperatures with all the advantages associated to an integrated approach.

In particular, the thesis is organized as follows:

1. Chapter 1 will initially give a general overview of microfluidics and LoC devices, with a particular emphasis on the advantages associated with working in a microfluidic environment. The research field of optofluidics, resulting from the combination of optics and microfluidics, will be then described and a theoretical model for a numerical calculation of optical forces will be presented. The second part of the chapter will instead focus on acoustofluidics which, similarly to optofluidics, combines ultrasonic acoustic waves with the several advantages offered by microfluidics. The femtosecond laser micromachining technology, which was employed for the fabrication of the optofluidic chip used for the rheological measurements, will be briefly described at the end of the chapter.
2. Chapter 2 will be dedicated to the presentation of the fundamentals of rheology, starting from the description of the rheological properties of simple elastic solids and viscous fluids. The chapter will continue with the discussion of viscoelastic materials, as well as the main rheological tests commonly performed to measure their properties. The chapter will end with a comparison between macroscopic and microscopic rheological techniques.
3. Chapter 3 will focus on the development of an integrated optofluidic microrheometer for optical shooting microrheology. The optical shooting experiments consist in exerting a step optical force on a microbead which will move in the surrounding medium stressing it. As previously stated, by monitoring the movement of the tracer it is possible to infer the rheological properties of the surrounding medium. The design and fabrication of the optofluidic chip will be initially presented, together with the experimental setup and the measurement procedure. After the discussion of the microrheometer calibration and validation, the measurements performed on a DNA hydrogel will be reported. The final part of the chapter will be dedicated to the results obtained performing optical shooting-based creep tests on yield stress fluids.
4. Chapter 4 will be centered on the realization of an integrated microrheometer for oscillatory microrheology. Differently from the optical shooting technique, in this configuration a microbead is sinusoidally oscillated at a certain frequency and at a certain stress level. This allows deriving the frequency-dependent viscoelastic properties of the surrounding medium. As it will be shown, the device is realized by connecting in cascade a Mach-Zehnder thermo-optical modulator and the integrated optofluidic chip. After the description of the working principle, the measurement protocol will be illustrated, as well as the microrheometer validation performed by measuring well-known aqueous worm-like micellar solutions.

5. Chapter 5 will finally focus on a theoretical study of the separation efficiency achievable in acoustofluidic systems, a minor project on which I have worked on during my PhD activity. An overview of acoustofluidic separation of microbeads/cells and of the main equations governing the motion of particles subjected to an acoustic field will be initially given. The chapter will then be dedicated to the investigation of the impact of different parameters on the achievable acoustic separation, dividing them in intrinsic and extrinsic factors, i.e. factors related to the samples' properties and to the system design and operation, respectively.

The work reported in this thesis has been carried out in the *Integrated Photonics Lab* (at the *Department of Electrical, Computer and Biomedical Engineering* of the *University of Pavia*), under the supervision of Prof. Paolo Minzioni. Moreover, during my PhD course I also worked for six months as a visiting PhD student in the *Nonlinear Photonics group* (at the *Institute of Applied Physics* of the *University of Münster*) headed by Prof. Cornelia Denz. I have been involved into an ongoing project focused on the measurement of viscoelastic properties of biological samples (such as cells and living tissues) by means of single-beam optical tweezers. The study of the rheological properties of biological specimens such as cells is particularly interesting due to the strong connection between these properties and the cellular health status. However, as the results of this study are still preliminary and need further in-depth analysis, they have not been included in this thesis.

1. Microfluidics and lab-on-chip technology

During the last decades, microfluidics and lab-on-chip technology have attracted the attention of the scientific community and the interest of companies to invest in these promising platforms. The interest in lab-on-chip technology arises from the possibility of integrating in a single small device a lot of functionalities. Different scientific fields significantly benefited from this technological development, as for example biology [1], medicine [2], chemistry [3] and rheology [4–6].

This chapter will firstly give a brief introduction to the field of microfluids and the possibilities offered by this technology. The largest part of the chapter will be then dedicated to the research field of optofluidics and acoustofluidics, which developed from the combination of microfluids with optical and acoustic actuators, respectively. The presentation of these theoretical concepts collected from the scientific literature is necessary for a complete understanding of this thesis.

1.1 Why microfluidics?

According to a diffused definition, microfluidics has been described as the science and technology of systems that study and manipulate small amounts of fluids (10^{-9} to 10^{-18} L) using channels with typical dimensions of tens to hundreds of micrometers [7]. Microfluidics represents the perfect platform for the integration of different functionalities toward the creation of the so-called lab-on-chip (LoC) devices, i.e. integrated systems in which it is possible to perform one or more highly-specialized laboratory functions handling a small fluid volume [8–10]. The extremely reduced sample volume required by LoC devices opened the way to the study of “precious” samples that are available only in very small quantities for different reasons such as production cost and lack of sample consistency. The ability to create micrometer-scale structures triggered a wide range of scientific researches devoted to the study, transport and manipulation of biological and complex samples in a fast, accurate and efficient way. The development of microfluids and LoC technology has been particularly evident in scientific areas like chemistry and biology. The possibility of working with reduced reagent volumes, parallel operations, and shorter reaction times opened new scenarios in the field of analytical chemistry [3,11]. Several emerging applications are becoming more and more important even in biophysics [12,13] and biology [1,14]. For example, LoC devices based on manipulation of living cells by means of optical forces allow studying the mechanical properties of single cells and their relation to cell differentiation, aging and malignant transformation [15–17]. Microfluidic technology is getting more and more interest even in other scientific areas such as medicine,

pharmaceutics, physical sciences, printing technology and rheology, just to name a few. Another advantage offered by microfluidics is the possibility to bring these small devices from one laboratory to another in order to easily build up a new setup.

A last characteristic feature to be mentioned of microfluidics, which is related again to the devices' small scales, is that the physical effects that take place in a microfluidic channel are different from what commonly happens in a "macro"-domain. In particular, the most evident physical phenomena in microfluidic systems is the *laminar flow*, which differs from the *turbulent flow* usually observed in everyday life. In a laminar flow regime all the fluid elements remain parallel to each other during the flow inside a closed space and do not mix during the propagation. The opposite situation is represented by the turbulent flow in which fluids vortex and mixing can happen. Figure 1.1 shows a graphical representation of the two different flowing regimes.

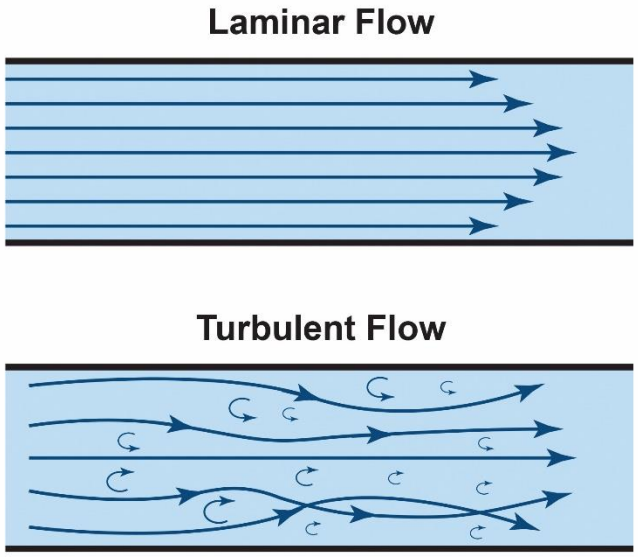

Figure 1.1: Comparison of different flow behaviors for laminar (top) and turbulent (bottom) flow regimes.

A dimensionless parameter usually employed in fluid dynamics to characterize the fluid behavior is the so-called *Reynolds number* Re, which is defined as:

$$Re = \frac{inertial\ forces}{viscous\ forces} = \frac{\rho v L}{\eta} \tag{1.1}$$

where ρ is the fluid density, v is the fluid velocity inside the channel, η is the fluid dynamic viscosity and L is the characteristic length scale of flow (e.g. the microchannel diameter in

case of flow in a pipe). The reference value of $Re = 3000$ is generally considered as the boundary value between turbulent flow ($Re > 4000$) and laminar flow ($Re < 2000$) [18]. In a microfluidic environment the Re number usually assumes very small values in the range 1-100 due to the significantly small length scale of the systems (L). This implies that the laminar flow is usually the dominant regime in microfluidic channels.

In conclusion, a possible reply to the question "why microfluidics?" can be given by reporting all the inherent advantages associated to this technology such as integration, miniaturization, parallelization, portability, low fabrication cost, low sample consumption, laminar flow-related advantages, rapid and high-throughput analysis.

1.2 Optofluidics

Optofluidics is the research field where optics and microfluidics merge to create LoC devices for different applications such as imaging [19] and sensing [20]. This research area is relatively new as suggested by the fact that the first appearance of the "optofluidics" word on Web of Science database dates back to 2005 [18]. However, the interest in this field is growing very fast as confirmed by the large number of papers published and citations given to optofluidic research. Optofluidic applications include LoC devices for diagnostic and sensing [21–24], holographic on-chip microscopy and tomography [25,26], live cell imaging [27,28], optofluidic tunable microlenses [29,30], single-cell protein [31,32] and DNA analysis [33,34], rheology [35], immunoassays [36,37] and applications in the energy research field [38,39].

In this section the basic theory of optical forces and a theoretical model for optical force calculation will be presented as these concepts are necessary in order to have a complete understanding of this thesis.

1.2.1 Optical forces

The optical force is literally the force which is exerted by light on an object. Optical forces have been, and are, extensively used in biology and physical sciences. The main reason for their successful application in these scientific areas is the possibility of employing optical forces for trapping and manipulating micro-beads and cells in a contact-less, gentle and bio-friendly way [40]. A tremendous contribution to the study and application of optical forces for optical trapping and micro-manipulation was given by the pioneering works conducted by Arthur Ashkin [41–46]. Ashkin was awarded half of the 2018 Nobel Prize in Physics "for the optical tweezers and their application to biological systems". He demonstrated the possibility of using a highly focused laser beam to trap and

move micro-particles and cells thus opening the way to different research studies as it is testified by the large number of "optical tweezers labs" around the world.

In order to give a physical description of the optical force we can consider light as composed by a stream of elementary particles called *photons*. Each photon carries a certain energy E given by:

$$E = hf \tag{1.2}$$

where $h = 6.626 \cdot 10^{-34} J \cdot s$ is the Planck's constant and f is the photon's frequency. Moreover, each photon carries a certain momentum p, whose magnitude equals to:

$$p = \frac{E}{c} = \frac{hfn}{c_0} \tag{1.3}$$

where c_0 is the light speed in vacuum, n is the refractive index of the medium where the photon is travelling and c is the light speed in that medium.

An intuitive description of the optical force exerted by light is the following. Let consider a light beam travelling through the interface separating two different media. The light beam will experience reflection and refraction due to the different refractive indices of the two media. These phenomena will change the momentum of the photons in terms of both direction and amplitude. As the total momentum of the system must be conserved, some momentum is transferred from the photons to the interface and hence, by Newton's second law, the interface will be subjected to a force.

For a better understanding, let consider the illustration and calculations reported in the example proposed by *Guck et al.* [15], which can be seen in Figure 1.2. A light beam is propagating in a medium with refractive index n_1 and then it encounters a cube of optically denser dielectric material with a larger refractive index n_2. By considering the momentum conservation, the light beam entering the dielectric medium increases its momentum and hence the interface gets a momentum in the opposite (backward) direction. When instead the light beam leaves the dielectric object exiting the other surface, it loses momentum while the cube surface gets momentum in the direction of the light propagation (forward). The light reflected on both surfaces results in a momentum transfer to both surfaces in the direction of the light propagation. In the considered example, this contribution to the surface forces is smaller than the contribution deriving from the increase of the light's momentum inside the cube. The reason can be found in the small reflection coefficient being the refractive indices difference low in this specific case. Assuming as in the example an incoming beam with an optical power of 800 mW, $n_1 = 1.33$ and $n_2 = 1.37$, the two

forces acting on the cube surfaces are opposite in direction and have magnitudes equal to 105 pN (in the backward direction) and 108 pN (in the forward direction). Considering separately the two forces acting on the cube surfaces, they tend to stretch the object. However, the asymmetry between the surface forces results in a net force that acts on the cube center in the direction of the light propagation. It should be pointed out that in this case the forces acting on the cube surfaces are significantly larger than the net force acting on the cube center.

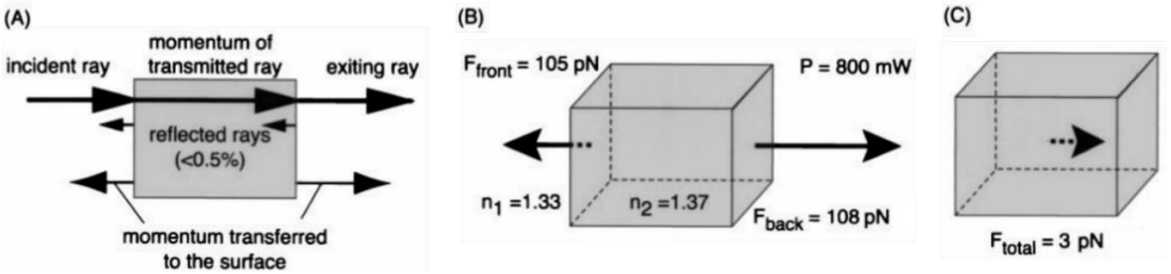

Figure 1.2: Illustration of the optical forces acting on a dielectric cube due to an incoming light beam [15]. *(A) Schematic representation of a single light beam undergoing to reflection and refraction due to the interaction with a dielectric box and consequently partially transfer of its momentum. (B) Considering an incoming light beam with an optical power of 800 mW, the refractive indices of the surrounding medium and of the cube being equal to 1.33 and 1.37, respectively, it is possible to calculate the optical forces acting on the two cube surfaces. (C) Due to an asymmetry of the optical forces acting on the two surfaces, a resulting net force acting on the box center is responsible of its movement along the light propagation direction.*

1.2.2 Theoretical model for optical force calculation

The calculation of the optical force exerted by a laser beam on an object obviously depends on a lot of parameters such as the spatial intensity distribution of the beam, the target object geometry and its dimensions with respect to the light wavelength. In the specific case for this work, a theoretical model for the optical force calculation will be employed for non-focused Gaussian laser beams imping on dielectric particles (which can be modelled as spheres) which are significantly larger than the laser wavelength. In this situation a paraxial ray-optics (PRO) approach can be used for the optical force calculation, which gives reliable results even in the case of a laser beam interacting with a dielectric particle within the beam Rayleigh range [47]. As previously described, when a light ray interacts with a particle, it modifies its momentum due to the reflection and refraction phenomena at the microsphere interface. This results in a momentum transfer from the light ray to the microsphere and hence the microsphere will be subjected to a force. In order to calculate the optical force exerted by a non-focused Gaussian laser beam on a microsphere in the PRO approximation, the first step is represented by an accurate decomposition of the light beam into a distribution of optical rays. Each ray will be

associated with a proper position in space, propagation direction and will carry a certain optical power. Once the optical field distribution is known in each spatial coordinate, it is possible to evaluate the optical force acting on the microsphere by summing all the contributions given by each ray.

The first step, i.e. the decomposition of a non-focused Gaussian laser beam into optical rays, is shown as a sketch in Figure 1.3. The ray-optics decomposition can be obtained by considering the far field (FF) distribution, which can be calculated through an angular spectrum decomposition technique [48] starting from the knowledge of the near field (NF) distribution. Once the FF distribution is calculated, the propagation direction of each ray, which is perpendicular to the wavefronts, can be determined through the spatial phase gradient while the rays' power can be assessed considering the FF amplitude. In particular, the power associated to each ray which intercepts the z coordinate at a distance ρ_0 from the beam axis can be determined as the result of the integral of the FF intensity as a function of the radial coordinate ρ, in the region of the annulus determined by $\Delta\rho$, as schematically sketched in Figure 1.3 a). Specifically, by adopting the PRO approximation, the optical field of a non-focused Gaussian laser beam can be described according to the following analytical expressions [49]. Considering the optical beam having a minimum waist w_0 at a position $z = 0$, it is possible to calculate the electric-field amplitude (A) and the radius of curvature (R) of the wavefronts as:

$$A(\rho, z) = A_0 \frac{w_0}{w_z} exp\left(-\frac{\rho^2}{w_z^2}\right) \tag{1.4}$$

$$R(z) = z + \frac{z_R^2}{z} \tag{1.5}$$

where A_0 is the electric-field amplitude at the position $z = 0$, z_R is the Rayleigh range and w_z is the beam width as a function of the propagation direction z, which are given by the following expressions:

$$z_R = \frac{\pi w_0^2 n}{\lambda} \tag{1.6}$$

$$w_z = w_0 \sqrt{1 + \left(\frac{z}{z_R}\right)^2} \tag{1.7}$$

By considering the previous equations it is possible to calculate a proper beam decomposition into a countless number of optical rays according to the PRO approximation. The amplitude $A(\rho, z)$ can be used to determine the optical power associated to each ray, while the radius of curvature $R(z)$ can be employed to assess the propagation direction, which is perpendicular to the wavefronts [50]. This step allows determining the optical field distribution for a non-focused Gaussian laser beam as a function of the space coordinates. Figure 1.3 reports a graphical representation of the electric-field amplitude and radius of curvature as a function of ρ and z.

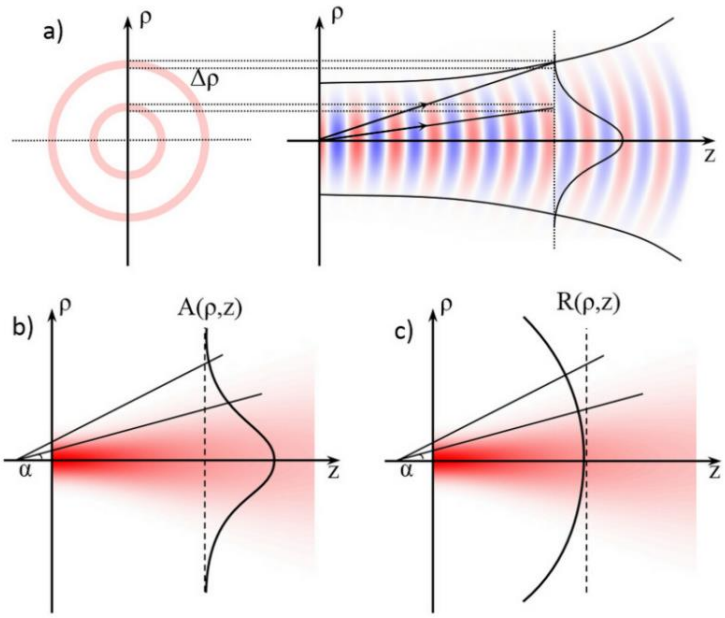

Figure 1.3: Scheme of the method used to calculate the optical field distribution in the PRO approximation [49]*. a) The power associated to each optical ray is calculated as the integral of the intensity of the beam, as a function of* ρ *in the area of the annulus determined by* $\Delta\rho$*. At each position along the* z *axis the b) electric-field amplitude and c) the radius of curvature of the Gaussian beam are calculated. These quantities are respectively used to calculate the power and the propagation direction associated to each ray.*

Once the spatial distribution of optical rays corresponding to the Gaussian beam is determined, the optical force exerted on the microsphere can be calculated as the sum of all the force contributions given by each ray. Figure 1.4 shows the interaction of a single ray from a Gaussian beam with a microsphere [49]. Each optical ray undergoes multiple reflections and refractions each time it interacts with the microsphere boundary. For each phenomena an optical force is induced on the microsphere surface. If the microsphere has a larger refractive index with respect to the surrounding medium, it can be shown that each force contribution is perpendicular to the microsphere surface and points away from the microsphere center.

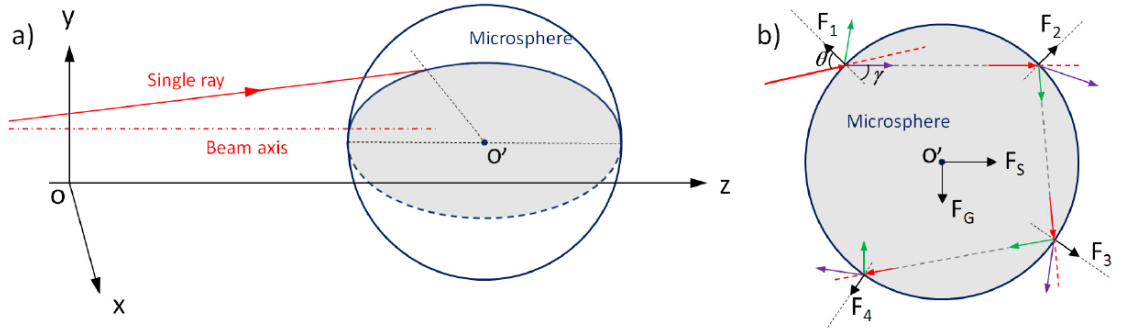

Figure 1.4: Illustration of a single ray interaction with a microsphere having an higher refractive index with respect to the surrounding medium [49]*. a) A single ray hitting a microsphere; the plane of incidence is indicated by gray color. b) The optical ray undergoes to different reflections (green arrows) and refractions (violet arrows) and an optical force (black arrows) is generated on the microsphere surface each time the optical ray interacts with the microsphere boundary.*

By summing all the contributions given by the ray-microsphere boundary interactions the final result is a net force acting on the center of the sphere which can be divided into a scattering component (F_S) and a gradient component (F_G), given by the following equations [42]:

$$F_S = \frac{n_M P}{c}\left\{[1 + Rcos(2\theta)] - T^2\frac{cos(2\theta - 2\gamma) + Rcos(2\theta)}{1 + R^2 + 2Rcos(2\gamma)}\right\} \quad (1.8)$$

$$F_G = \frac{n_M P}{c}\left\{[1 + Rsin(2\theta)] - T^2\frac{sin(2\theta - 2\gamma) + Rsin(2\theta)}{1 + R^2 + 2Rcos(2\gamma)}\right\} \quad (1.9)$$

where n_m is the refractive index of the surrounding medium, P is the power of the optical ray, c is the light speed in vacuum, R and T are respectively the Fresnel reflection and refraction coefficients at the microsphere interface, given a certain incidence angle θ, and γ is the angle of refraction, as shown in Figure 1.4. As it can be seen from the figure, the scattering force F_S is directed along the beam axis and tends to push away the microsphere, while the gradient force F_G is directed perpendicularly with respect to the optical axis and tends to pull the microsphere toward the beam axis in the region of the maximum optical intensity.

Finally, the optical force acting on the microsphere can be obtained by summing all the force contributions given by the single optical rays. Figure 1.5 reports the numerical calculations of the scattering and gradient forces exerted on a PMMA microbead ($n = 1.48$ at 1070 nm) with a radius equal to 5 μm immersed in water ($n = 1.33$ at 1070 nm). A non-

focused Gaussian laser beam has been considered for the calculation, having a wavelength of 1070 nm, a minimum beam waist of 3.8 μm at $z = 0$ and a power of 10 mW. The scattering force, which is shown in Figure 1.5 a), is calculated considering the microbead positioned in the beam center ($\rho = 0$) so as to keep the gradient force constant and equal to zero. Similarly, the gradient force, shown in Figure 1.5 b), is computed considering the microbead positioned at a fixed z position ($z = 0$).

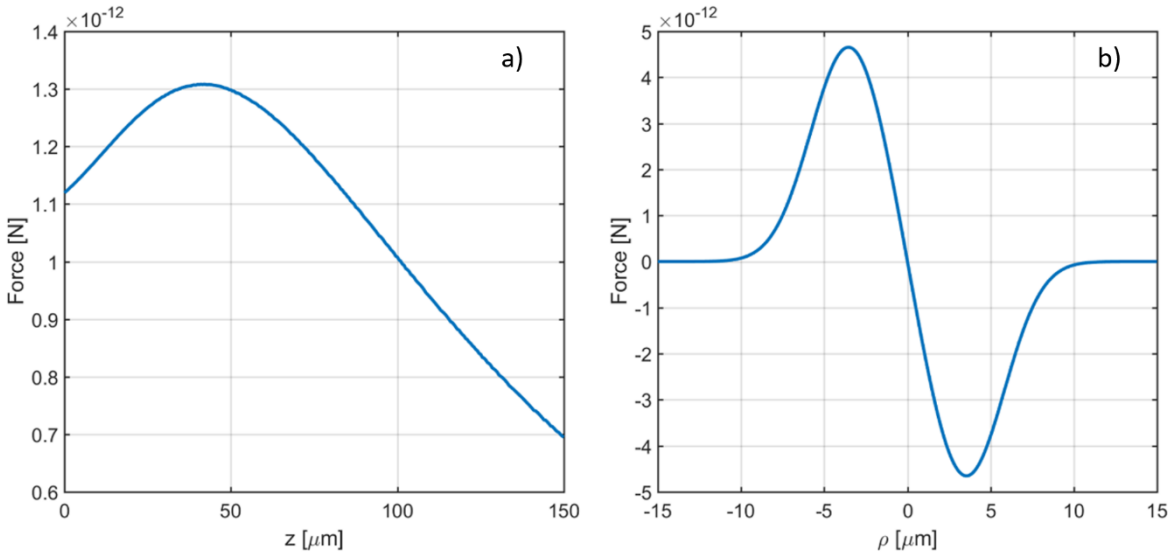

Figure 1.5: Optical force acting on a PMMA microbead with a radius of 5 μm suspended in water. A non-focused Gaussian laser beam has been considered for the numerical calculations, with a wavelength of 1070 nm, a minimum beam waist of 3.8 μm at $z = 0$ and a power of 10 mW. a) The scattering force is calculated as a function of the propagation direction z considering the microbead positioned in the beam center ($\rho = 0$). b) The gradient force is calculated as a function of the ρ coordinate at a fixed z position ($z = 0$).

Some observations can be made observing the shapes of the two forces. The scattering force is initially increasing, it reaches a maximum and then starts to decrease as a function of the z coordinate. In order to explain the origin of this maximum, it must be pointed out that the optical force exerted on the microbead mainly depends on two factors: the optical power P impinging on the microbead and the incidence angle θ formed between the ray and the normal to the particle surface. In particular, the force is an increasing function of P and of θ, as demonstrated in [42]. In the here-considered case, the optical power impinging on the microbead is a decreasing function of z due to the beam divergence. Conversely, the angle of incidence θ formed by the optical rays with respect to the normal to the particle surface is small for small values of z (i.e. closer to the origin), while it increases when z becomes larger. This results in an initial increase of the scattering force due to the increase of θ, while after reaching a maximum the force starts decreasing

because the force behavior starts to be dominated by the decrease of the incident optical power. Observing the profile of the gradient force it can be seen how this force tends to attract the microbead along the beam axis, where the gradient force goes to zero, creating an optical trap along the ρ direction. Another point that can be noticed by comparing the two forces is that the gradient force is acting on a smaller distance scale with respect to the scattering force.

The forces exerted on a microsphere in a multiple beam configuration can be numerically simulated by properly adding more laser sources and summing their contributions to find the overall optical force distribution on the microbead. An interesting configuration that is proposed in this thesis for rheological measurements is a dual beam laser trap consisting in two counterpropagating laser beams which can be exploited to trap and manipulate a single microbead. A graphical representation of this optical trapping system is shown in Figure 1.6.

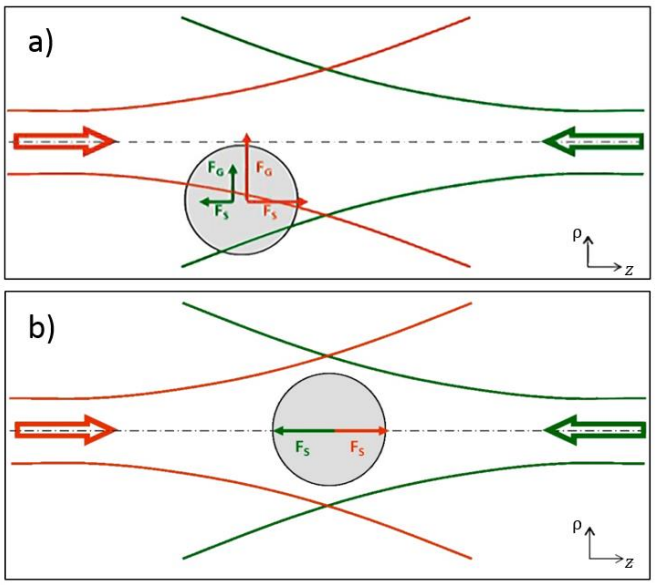

Figure 1.6: Schematic representation of the dual beam laser trap. a) A microbead is subjected to the optical forces exerted by two counterpropagating laser beams. The gradient forces tend to pull the microbead along the optical axis. b) Assuming that the optical beams have the same power, the microbead will be trapped at the channel center where the two scattering forces have the same magnitude.

Let assume to have two optical waveguides emitting two optical beams with the same characteristics (laser wavelength, beam waist, optical power), which interact with a microbead having a refractive index higher than that of the surrounding medium (e.g. a PMMA microbead dispersed in a microfluidic channel filled with water). The microbead will be pulled toward the common beam axis ($\rho = 0$) due to the gradient forces. Once the bead

reaches the optical axis, the gradient forces will go to zero and only the scattering forces will be responsible of the microbead movement. Assuming that the two optical beams have the same power, the microbead will reach a stable trapping position in the microchannel center at the same distance from the two optical sources, where the scattering forces have the same magnitude and opposite direction. This configuration, together with numerical calculations of optical force profiles, will be discussed in more detail in Chapter 3.

1.3 Acoustofluidics

Similarly to optofluidics, on-chip acoustofluidics combines the use of ultrasonic acoustic waves with the advantages offered by microfluidic platforms. This scientific field is acquiring a significant research interest as it is testified by the several review papers [51,52], tutorials [53] and books [54] that have been recently dedicated to it. Acoustofluidics permeated into many different research studies and already found a lot of applications related to micro-particles and cells sorting [55], focusing [56], separation [57–59], mixing [60] and arraying [61–63] to micro-droplets production [64] and manipulation [65,66]. Further applications of acoustofluidics will be presented in more detail in Section 5.1. As for optical forces, the great potentiality offered by acoustic forces relies in the possibility of manipulating micro-particles and cells in contact-less and bio-friendly way.

Following the same line of the previous paragraph, the first part of this section will be dedicated to a short description of the acoustic forces, only for the theoretical points of interest for this thesis. In particular, the acoustic radiation force acting on microbeads suspended in a fluid will be described, as this is the typical situation encountered in acoustofluidics and the one treated in this thesis.

1.3.1 Acoustic resonance in microfluidic devices

Acoustic forces can be employed in a microfluidic environment to trap and manipulate microbeads and cells. The movement of micro-objects induced by acoustic forces is called *acoustophoresis*. Acoustic forces result from the interaction of sound waves with the suspended objects and the surrounding medium. A peculiar advantage offered by acoustofluidics is the possibility of imposing standing ultrasonic waves in a microfluidic channel. The operation of acoustofluidic devices in this resonance mode has the advantage of being stable and highly reproducible, as the standing acoustic wave properties are related to the geometry of the device. This implementation opened the way to the realization of high-throughput, label-free devices for separation of different cell populations. In particular, the formation of an ultrasonic standing wave in a microfluidic

channel gives rise to two distinct contributions to the acoustic forces: the acoustic radiation force, from the scattering of sound waves by the particles, and the Stokes drag force, from the induced acoustic streaming flow [67]. The acoustic radiation force is commonly employed for acoustic pre-focusing and sorting of microbeads and cells. The second force contribution arises from the streaming flow effects produced in the fluid by the acoustic field. This induced streaming flow can result in a Stokes drag force acting on the microbead. In a microfluidic device one force contribution can be dominant over the other one and the crossover from one acoustic behavior to the other depends on different parameters such as the microchannel dimension, the fluid viscosity and density, the microbead radius and compressibility [67]. As the experimental conditions presented in this thesis always allow considering the acoustic radiation force dominant over the acoustic streaming induced drag force, the latter will not be theoretically treated in this section.

In order to manipulate micro-particles in a microfluidic channel thanks to the use of acoustic forces, the ultrasound actuation is typically performed by applying bulk [56] or surface acoustic waves [51]. These waves can be produced by imposing a sinusoidal voltage to an externally mounted piezoceramic in contact with the microfluidic chip [56] or to interdigitated metal electrodes deposited on a piezoelectric substrate [68], respectively. Ultrasonic waves in the low MHz range are usually employed for microfluidic applications cause these frequencies allow easily obtaining an acoustic standing wave in the microfluidic channel, as it will be explained in this section.

The governing equations for the acoustic field and its effect on microparticles suspended in a fluid are well-known and have been extensively reported in the scientific literature [53,69]. Considering the situation of interest for this thesis, we can assume to have a suspension of dielectric microbeads dispersed in a fluid (e.g. water) in a microfluidic channel realized in a glass chip. An external piezoceramic is positioned well in contact under the glass chip. When a sinusoidal AC voltage at MHz frequency is applied to the electrodes of the piezoceramic, it starts to vibrate and induces a time-harmonic ultrasound pressure field $p_1 \exp(-i\omega t)$, where $\omega = 2\pi f$ is the angular frequency and f is the frequency. For the sake of simplicity, the time-harmonic factor is implicitly assumed and only the pressure field amplitude p_1 will be reported. The same consideration applies for the velocity field $\boldsymbol{v}_1$ of the carrier fluid. Before the application of the external ultrasound field, the microbeads suspension and the fluid inside the microfluidic channel are in a quiescent state at a constant uniform pressure p_0 and at a velocity $\boldsymbol{v}_0 = 0$. The viscosity of the fluid in the microchannel has a negligible influence on the acoustic radiation forces and therefore, when the external ultrasound field is applied by actuating the piezoceramic, the pressure field p_1 and the velocity field $\boldsymbol{v}_1$ inside the glass chip and the microfluidic channel are governed by the linear acoustics of inviscid fluids [69].

In particular, the Helmholtz wave equation for the pressure and the potential flow for the velocity can be considered, as given by the following equations:

$$\nabla^2 p_1 = -\frac{\omega^2}{c_f^2} p_1 \tag{1.10}$$

$$\boldsymbol{v}_1 = -\frac{i}{\omega \rho_f} \boldsymbol{\nabla} p_1 \tag{1.11}$$

where c_f and ρ_f are the speed of sound and the density of the carrier fluid, respectively. In order to find the pressure field p_1 which satisfies the previous equations in our situation, we must apply a proper boundary condition. At a boundary characterized by the surface normal vector $\boldsymbol{n}$, three different boundary conditions can be applied: the hard wall (zero velocity) condition, the soft wall (zero pressure) condition and the continuity condition for the velocity and the pressure, which are described by the following equations:

$$\boldsymbol{n} \cdot \boldsymbol{\nabla} p_1 = 0 \text{ (hard wall)} \tag{1.12}$$

$$p_1 = 0 \text{ (soft wall)} \tag{1.13}$$

$$\frac{\boldsymbol{n} \cdot \boldsymbol{\nabla} p_1^{(a)}}{\rho_a} = \frac{\boldsymbol{n} \cdot \boldsymbol{\nabla} p_1^{(b)}}{\rho_b}, \quad p_1^{(a)} = p_1^{(b)} \text{ (continuity)} \tag{1.14}$$

As anticipated, in the situation of interest for this thesis (and in most of the cases commonly encountered in acoustofluidic applications), an acoustically soft fluid inside the microchannel is surrounded by an acoustically hard glass chip. This situation can be modelled by an acoustic cavity, as graphically shown in Figure 1.7. As we are dealing with an acoustic cavity, this implies that it is possible to have an acoustic resonance only for certain specific angular frequencies ω_j, with $j = 1,2,3, \ldots$, as reported in [69]. In particular, when an acoustic resonance is set at a certain angular frequency ω_j, this means that the system is in a condition in which the average acoustic energy density inside the cavity at ω_j is different orders of magnitude larger than at any other angular frequency. By driving the piezo-stage at one of these resonance frequencies, the resulting acoustic forces become strong enough to be employed for moving microparticles suspended in the fluid in a controlled way. The values of the resonance frequencies depend on different parameters such as the density and the speed of sound of the liquid in the cavity and of the surrounding material as well as on the cavity geometry.

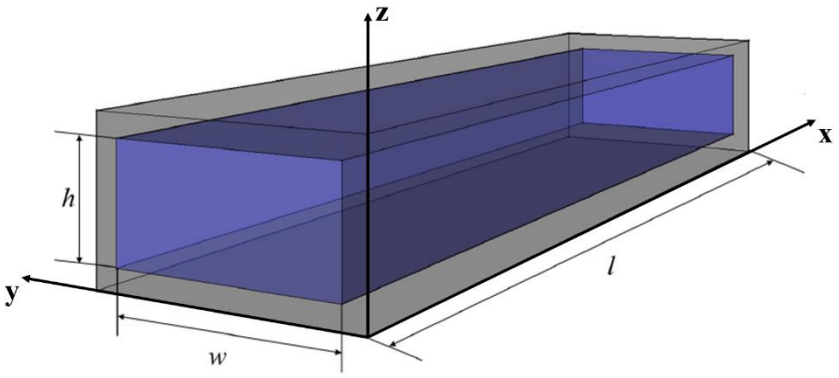

Figure 1.7: Schematic representation of the microchannel geometry considered in this study. A silica glass chip (gray color), having width w, length l and height h, is filled with a fluid (blue color).

Generally, the resonance frequencies can only be calculated through numerical simulations. However, an analytical solution can be easily found by considering a rectangular channel of length l, width w, and height h, as the one shown in Figure 1.7, surrounded by an infinitely hard material. This last condition is satisfied to a good approximation in the considered case of our silica glass chip. Under this assumption, the velocity on all the microchannel walls is equal to zero, which referring to Equation 1.11 is equivalent to the hard wall boundary condition, i.e. $\boldsymbol{n} \cdot \boldsymbol{\nabla} p_1 = 0$. By imposing this boundary condition, and considering a rectangular box (as the one shown in Figure 1.7) placed along the coordinate axes with its opposite corners at (0,0,0) and (l,w,h), the pressure field p_1 solving Equation 1.10 is given by:

$$p_1(x,y,z) = p_a \cos(k_x x)\cos(k_y y)\cos(k_z z), \quad \text{with } k_j = n_j \frac{\pi}{L_j} \text{ and } n_j = 0,1,2,3,\ldots \tag{1.15}$$

where p_a is the pressure amplitude and the microchannel dimensions are given by $L_x = l$, $L_y = w$ and $L_z = h$. An acoustic standing wave can be therefore induced in a microfluidic channel, whose most general expression is given by the previous equation. The corresponding three-index resonance frequencies can be written as:

$$f_{n_x,n_y,n_z} = \frac{c_f}{2}\sqrt{\frac{{n_x}^2}{l^2} + \frac{{n_y}^2}{w^2} + \frac{{n_z}^2}{h^2}} \text{ with } n_x, n_y, n_z = 0,1,2,3,\ldots \tag{1.16}$$

Considering the generic direction j, the nodes of the acoustic standing wave are given by the condition $\cos(k_j j) = 0$, i.e. $k_j j = (2n_j + 1)\frac{\pi}{2}$. Two examples of resonant standing acoustic waves for a water-filled microchannel having length $l = 1000\ \mu m$, width $w = 200\ \mu m$ and height $h = 100\ \mu m$ are shown in Figure 1.8. By considering for example the case reported in Figure 1.8 a), the lowest resonant frequency along the channel width (y direction) is given by $f_{0,1,0} = \frac{c_f}{2w}$. Recalling that $\lambda f = c_f$, the lowest resonant condition in this direction must satisfy the relation $w = \frac{\lambda}{2}$ or $k_y = \frac{\pi}{w}$ and this corresponds to have a single node position at half the channel width.

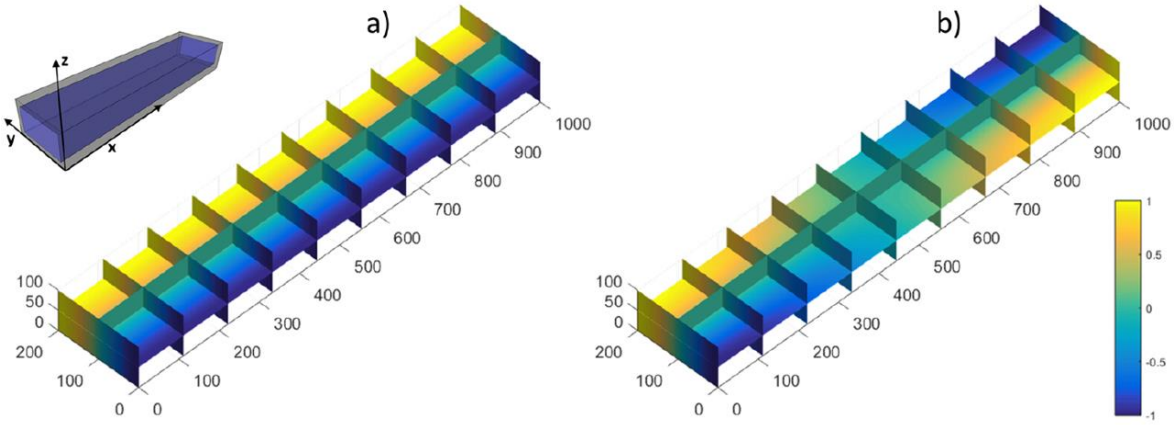

Figure 1.8: Color plot of the pressure field p_1 *at resonance for a microchannel filled with water (speed of sound* $c_f = 1483\ m/s$*) having length* $l = 1000\ \mu m$ *(x direction), width* $w = 200\ \mu m$ *(y direction) and height* $h = 100\ \mu m$ *(z direction) surrounded by an infinitely hard material. The values of the pressure field are normalized to the reported color scale. The resonance conditions are given by a)* $(n_x, n_y, n_z) = (0,1,0)$ *with a resonance frequency* $f_{0,1,0} = 3.7075\ MHz$ *and b)* $(n_x, n_y, n_z) = (1,1,0)$ *with a resonance frequency* $f_{1,1,0} = 3.7809\ MHz$.

1.3.2 Acoustic radiation force

The previously calculated first order pressure field p_1 allows determining the first order velocity field thanks to Equation 1.11. Once both the pressure field and the velocity field are calculated, it is possible to find the acoustic radiation force acting on a microbead with volume $V = (4/3)\pi R^3$, whose radius R is much smaller than the acoustic wavelength λ. This case is well verified for the microbeads dimensions considered in this thesis. The most general expression for the 3D time-averaged acoustic radiation force $\langle \boldsymbol{F}_{ac} \rangle$ is given by the gradient of the acoustic energy potential U_{ac}:

$$\langle \boldsymbol{F}_{ac} \rangle = -\boldsymbol{\nabla} U_{ac} \tag{1.17}$$

where $\langle X \rangle$ denotes the time average over an oscillation period and the acoustic energy potential is given by the following expression:

$$U_{ac} = V\left[\frac{f_1}{2\rho_f {c_f}^2}\langle p_1^2\rangle - \frac{3f_2\rho_f}{4}\langle|\boldsymbol{v}_1|^2\rangle\right] = \\ = \frac{V}{4\rho_f {c_f}^2}\left[2f_1\langle p_1^2\rangle - 3f_2\frac{1}{k^2}\langle|\boldsymbol{\nabla} p_1|^2\rangle\right] \tag{1.18}$$

where k is defined as $k^2 = k_x^2 + k_y^2 + k_z^2$. By observing the previous equation, the acoustic radiation force can be seen as the time-averaged effect of the acoustic pressure field. The terms f_1 and f_2 in the equation are called compressibility and density factors, respectively, and are calculated as:

$$f_1 = 1 - \frac{1}{\gamma\zeta^2}, \qquad f_2 = \frac{2\gamma - 2}{2\gamma + 1} \tag{1.19}$$

with γ and ζ, which are called density ratio and speed of sound ratio, respectively, that are given by:

$$\zeta = \frac{c_p}{c_f}, \qquad \gamma = \frac{\rho_p}{\rho_f} \tag{1.20}$$

with c_p and ρ_p being the speed of sound and the density of the particle, respectively.

An easier formulation of the acoustic radiation force can be derived in the 1D standing wave situation, which is the one treated in this thesis. In the common situations of interest for acoustofluidics, the width w and the height h are significantly shorter than the length l of the microchannel, which corresponds to the flowing direction. In particular, an acoustic standing wave is commonly created along the width and/or the height of the microchannel in order to affect in a controlled way the transversal position of the flowing objects. Therefore, in the following, a resonant condition along the flowing x direction will be no more considered, meaning that $k_x = 0$. By considering for example a 1D acoustic resonance along the y direction, the analytical expression of the acoustic radiation force is:

$$F_{ac}(y) = \left(\frac{4}{3}\pi R^3\right) k_y E_{ac} \varphi sin\left(2k_y y\right) \tag{1.21}$$

where $k_y = n_y \frac{\pi}{w}$ is, as before, the acoustic wave number, $E_{ac} = p_a^2/\left(4\rho_f c_f^2\right)$ is the acoustic energy density in the 1D situation and φ is the acoustic contrast factor, whose expression is given by:

$$\varphi = \frac{5\gamma - 2}{2\gamma + 1} - \frac{1}{\gamma\zeta^2} = \frac{5\rho_p - 2\rho_f}{2\rho_p + \rho_f} - \frac{\beta_p}{\beta_f} \tag{1.22}$$

in which $\beta_p = 1/\left(\rho_p c_p^2\right)$ and $\beta_f = 1/\left(\rho_f c_f^2\right)$ are the compressibility values of the particle and the fluid, respectively.

Referring to Equation 1.21 and considering a microfluidic channel in which some microbeads are dispersed, if an acoustic standing wave is established along the channel width (or similarly along the channel height), the acoustic force, due to the scattering of acoustic waves by the microbeads, will push the microparticles toward the nodes of the acoustic standing wave, provided that the acoustic contrast factor is positive. Among all the possible resonant modes, the lowest order modes $(\mathrm{n_y}, \mathrm{n_z}) = (1,0)$ (resonant frequency $f_{1,0}$) and $(\mathrm{n_y}, \mathrm{n_z}) = (0,1)$ (resonant frequency $f_{0,1}$) can be exploited to obtain a node in the center of the selected channel dimension. For example, the microfluidic system employed in this thesis for the rheological measurements embeds a microfluidic channel having a square cross-section geometry (150 × 150 μm^2). As the microchannel has a square cross-section, the resonant frequencies $f_{1,0}$ and $f_{0,1}$ have the same value, e.g. 4.9434 MHz considering water (speed of sound in water $c_f = 1483\ m/s$). Figure 1.9 shows the instantaneous pressure field (see color plot) and the acoustic radiation force pattern (see vector arrows) for the considered square channel for an acoustic resonance along the a) z direction (channel height) and b) y direction (channel width). By referring to Figure 1.9 a), the microbeads will be pushed by the acoustic force toward the half height of the channel, while in case b) the microbeads will be pushed toward the half width of the channel. As the resonance frequency is the same for both the acoustic resonances, both the contributions will be present simultaneously and the combined effect on the acoustic radiation force pattern in the microfluidic channel is shown in Figure 1.9 c). The result is a single point node position exactly in the channel center, which allows the realization of the so-called *acoustophoretic prefocusing*, as all the microbeads will be pushed toward the center of the microchannel [56].

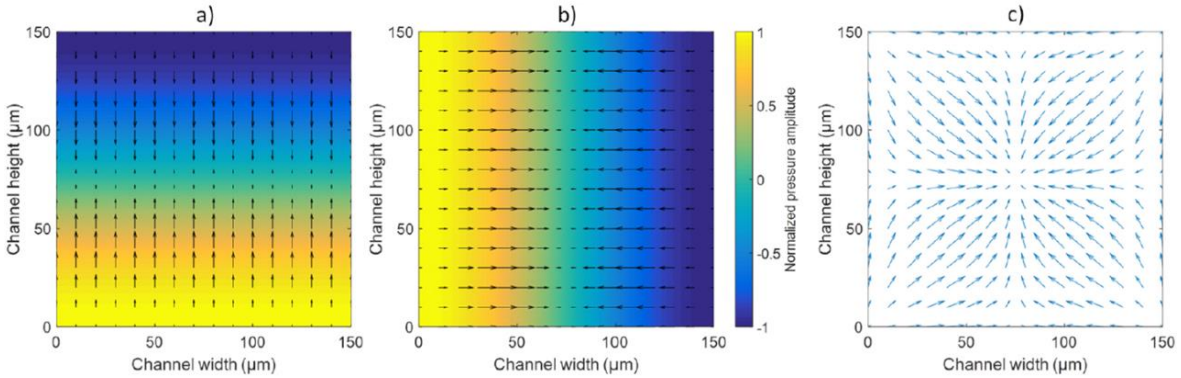

Figure 1.9: Representation of the normalized instantaneous pressure field (see color plot) and of the acoustic radiation force patterns (see vector arrows) for a channel with dimensions 150 × 150 μm^2. The acoustic resonance along the a) height direction and the b) width direction are shown, corresponding to the resonant modes $f_{0,1}$ and $f_{1,0}$. The resulting acoustic radiation force pattern in the microchannel is shown in c).

1.4 Femtosecond laser micromachining for lab-on-chip devices fabrication

As previously discussed in Section 1.1, LoC devices opened the way to a precise control and manipulation of reduced sample volumes for applications such as sensing and imaging. These devices allowed downsizing chemical and biological analysis to small systems, which are characterized by small physical dimensions but high performances. Different techniques have been developed and improved for the fabrication of LoC systems using different materials such as glass, silica and polymers. In particular, the materials employed for the chip fabrication must fulfil some requirements, according to the specific application. Biocompatibility is for example required in case LoC devices are devoted to biomedical and biochemical analysis. Another common requirement is the material optical transparency in the visible range which allows recording videos during the device operation by optical microscopy. A good choice for many applications is represented by glass, which exhibits high-pressure resistance, high optical transparency and it is chemically inert. The main problem represented by glass is related to its high production cost for the fabrication of microfluidic devices. Due to this drawback, new materials have been studied. In particular, polymers offer a good alternative to glass as they are cheaper and require a faster and easier fabrication process. However, the performance exhibited by glass devices are still better in terms, for example, of measurement repeatability and high-pressure operation. For what concerns the fabrication methods, they can be divided in two main categories: *soft photolithography* and *femtosecond laser micromachining* (FLM). In particular, FLM is an emerging technique that has recently attracted a significant attention for the fabrication of microfluidic and optofluidic devices [70–73]. A significant advantage offered by FLM is the possibility to fabricate three dimensional structures in transparent

materials, including for example polymers and glass. In this section the basics of the FLM procedure will be presented.

In general, when a single photon has an energy which exceeds the band-gap energy of a material, that photon can be absorbed and in this way an electron is promoted from the valence band (VB) to the conduction band (CB). This process is called single-photon absorption (SPA) and is shown in Figure 1.10 a). However, when a high-intensity laser pulse (and hence a high density of photons) is focused on a material, it could happen that an electron is promoted by the combined action of multiple photons via virtual states, even if the single photon energy is significantly smaller than the band-gap energy. This particular process is called multi-photons absorption (MPA) and it is shown in Figure 1.10 b). This nonlinear phenomenon, which allows the absorption of highly focused femtosecond laser pulses by transparent materials such as glass, is the basic principle exploited in FLM. It is worth noticing that this light-matter interaction occurs only closer to the focal area where the high optical intensity can trigger the MPA phenomenon.

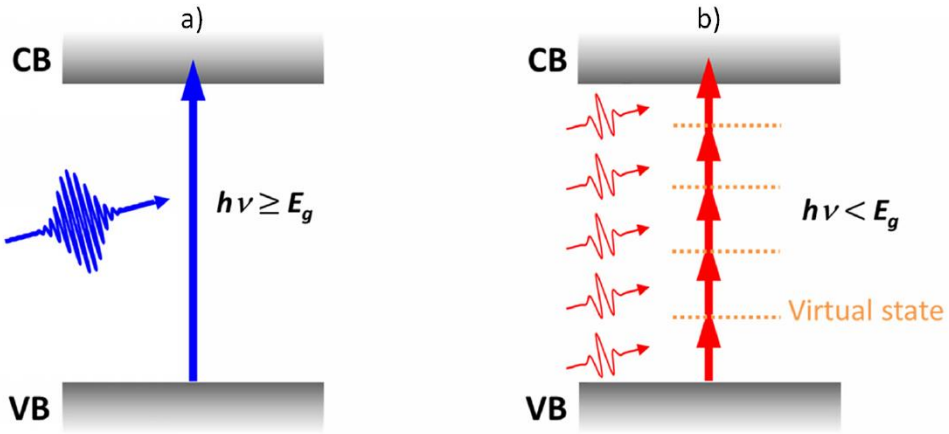

Figure 1.10: Schematic representation of a) single-photon and b) multi-photons absorption [74]. *VB: valence band; CB: conduction band; E_g : band-gap energy; $h\nu$: single photon energy.*

The use of focused femtosecond laser pulses offers several advantages with respect to conventional laser fabrication techniques exploiting continuous wave (CW) lasers or lasers emitting long pulses. The first advantage is related to a significant reduction of the thermal diffusion effects during the material processing due to the fact that most of the energy of the femtosecond laser pulse is absorbed by the electrons and it is not transferred to the material lattice [74]. This is possible thanks to the fact that the femtosecond laser pulse duration is significantly shorter than the electron-phonon coupling time (typically of the order of several to few tens of picoseconds). The result is that the free electron temperature increases rapidly in the focal area of the femtosecond laser pulse and becomes significantly higher than the lattice temperature. The material in this area is

consequently ejected in a short time in the form of hot dense plasma, leaving the local lattice still at a relatively low temperature. This property avoids the formation of heat-affected region, thus allowing the fabrication of three-dimensional structures with micro- and nano-scale features thanks to FLM. Contrarily, for CW lasers and for lasers emitting optical pulses having a duration significantly longer than the electron-phonon coupling time, the radiation energy is initially transferred to the electrons, but then the electrons transfer it to the material lattice before the pulse is terminated. In this way the free electrons and the lattice reach an equilibrium state and the result is that the laser simply heats the solid for all the pulse duration giving rise to a significant thermal diffusion and to a subsequent reduction of the fabrication quality and achievable resolution. Another advantage offered by FLM is given by the possibility of realizing a 3D internal processing in a transparent material, which cannot be made by exploiting CW or long laser pulses. The possibility of writing structures internally results from the fact that MPA only occurs in the beam focal volume of the femtosecond laser, where the light intensity is sufficiently high to trigger the nonlinear effect. A last characteristic to be mentioned is related to the sub-diffraction-limited resolution achievable with FLM. Without entering into details, the effective processing profile achievable with a femtosecond laser beam can be much narrower than its Gaussian intensity profile and this characteristic is again related to the MPA process. The achievable fabrication resolution far beyond the optical diffraction limit opened the way to the realization of novel device architectures with enhanced functionalities.

Considering all the reported advantages, FLM can be employed to fabricate photonic circuits (e.g. optical waveguides, modulators, quantum circuits) and integrated optofluidic systems, combing microfluidic channels and optical elements. As it will be presented in Chapter 3, the optofluidic chip employed for performing the microrheological measurements was realized exploiting the FLM technique by the *Fastgroup* (at the *Istituto di Fotonica e Nanotecnologie*, *Consiglio Nazionale delle Ricerche* of the *University of Milan*) headed by Dr. Osellame.

2. Fundamentals of rheology

Rheology is the branch of physics which deals with the flow and deformation of matter, both in solid and liquid state. The term *rheology* was coined by Eugene C. Bingham, a professor and head of the department of chemistry at Lafayette College, who was a pioneer in this field. This word was inspired by the famous aphorism of Simplicius (often attributed to Heraclitus) *panta rhei*, which literally means "everything flows" and was firstly employed to describe the deformation of solids and the flow of liquids.

The experimental study of the material rheological properties (called rheometry) is of fundamental importance in different fields, ranging from industrial products development to fundamental research. For an industrial point of view, understanding the different response of matter (viscosity, elasticity, yield stress, …) to an external perturbation is important to fine tune the material response to external conditions. Rheology is particularly important in the field of materials science and engineering. The study of the rheological behavior in materials science is a key factor for the optimized production of many industrially important products such as paint, rubbers, plastics and cements, just to report few examples. A large attention is paid to the study of the mechanical response of polymers, which represent the basic materials for the production of rubbers and plastics, that are of vital importance for a large number of industries in the textile, automotive and pharmaceutical field. Moreover, the processing, manufacture and production of food products strongly benefit from food rheology. Rheology permeates even other scientific areas such as biophysics, biology and medicine. For example, it has been shown that the change of the viscoelastic properties of blood are related to different cardiac pathologies [75,76] as well as metastatic cells present different mechanical properties with respect to non-metastatic and healthy cells [17].

This chapter is dedicated to the description of the fundamental concepts of rheology. After an introduction to the main physical quantities used to describe the rheological behavior of a medium, the main material classes will be presented ranging from simple viscous fluids and elastic solids to viscoelastic media. In the last part of the chapter, a comparison between the standard rheological techniques based on the use of a conventional rheometer with the emerging field of microrheology will be presented. Most of the theory presented in this chapter has been taken from [77–79].

2.1 Stress, strain and strain rate

In order to estimate the rheological properties of a material it is possible to study its response to an externally applied perturbation. In rheology, an external perturbation is commonly described by a quantity called *stress*, which will be in the following indicated as σ and which is defined as the force F per unit area A:

$$\sigma = \frac{F}{A} \quad [Pa] \tag{2.1}$$

In particular, the stress depends on the force magnitude, on the extension of the surface where the force is applied and on the spatial relation between the force and the surface itself. In general, it is possible to distinguish between two limit cases represented by the *shear stress* and the *normal or extensional stress*, graphically shown in Figure 2.1. The former is the stress component coplanar with a material cross-section and arises from the component of the force vector parallel to the material cross-section. The latter component results from the contribution of the force perpendicular to the material surface on which it acts, and it accounts for the typical case of compression and traction.

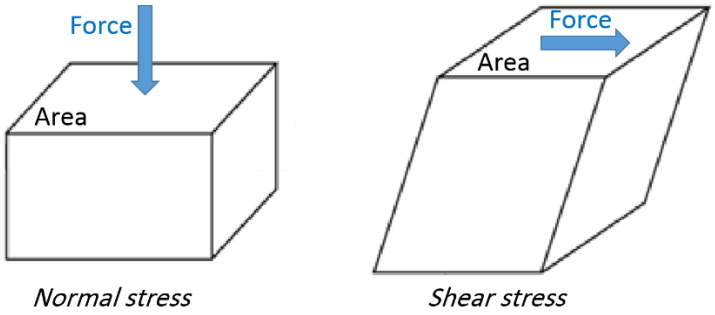

Figure 2.1: Graphical representation of normal stress (left) and shear stress (right) acting on a material surface.

As a result of the applied stress, the material can undergo to a certain deformation. The ratio of this deformation to the original material dimension gives a relative deformation that is commonly called *strain*, which is a dimensionless quantity and will be indicated in the following with the letter ε (even indicated in the scientific literature with γ). In particular, it is possible to distinguish between the *normal* and *shear strain*, depending on the type of applied stress, as shown in Figure 2.2.

The normal strain is defined as:

$$\varepsilon_{norm} = \frac{\Delta L}{L} \tag{2.2}$$

where ΔL is the material deformation and L is the original dimension along the direction of the force application. The shear strain is instead defined as:

$$\varepsilon_{shear} = \frac{\Delta L}{h} \tag{2.3}$$

where again ΔL is the deformation induced by the shear force while h is the nominal distance between the deformed and undeformed planes, as shown in Figure 2.2.

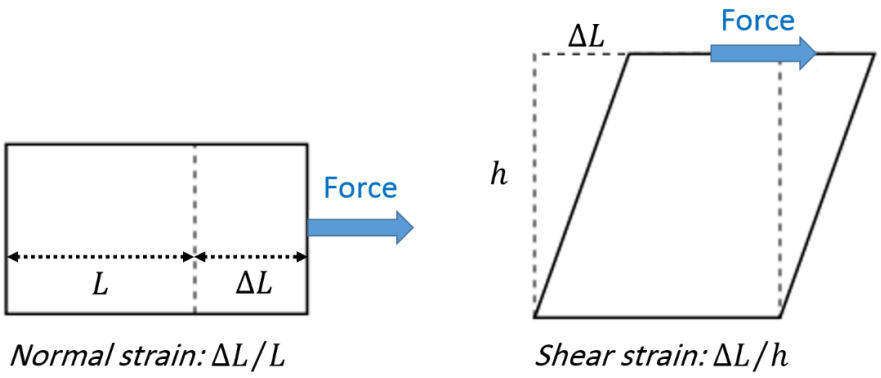

Figure 2.2: Graphical representation of normal strain (left) and shear strain (right) induced by an applied stress.

Another parameter that must be introduced for the study of the rheological properties of a material is the *strain rate*. The strain rate is defined as the rate of change in strain of a material with respect to time and it is generally given by the following expression:

$$\dot{\varepsilon} = \frac{d\varepsilon}{dt} \quad [s^{-1}] \tag{2.4}$$

Depending on the stress application, the strain rate can describe both the rate at which the material is shrinking or expanding (*expansion rate*) in case a normal stress is applied, and even the rate at which the material is being deformed by progressive shearing without modifying its volume (*shear rate*) in case a shear stress is applied. In order to better define

the shear rate, it is possible to refer to the simple situation of the planar Couette shearing flow. This configuration describes the flow of a fluid present between two infinitely large plates. One plate is fixed and cannot move, while the other plate is moving at a constant velocity u, tangentially with respect to the other one, as it is shown in Figure 2.3. By assuming that the speed of the top plate is low enough to avoid turbulence and considering the steady state condition, the fluid particles move parallel to the top surface, and their velocity goes from 0 at the bottom to u at the top surface. In particular, each fluid layer moves faster than the layer just below it. The shear rate can be defined as the derivate of the fluid speed in the direction perpendicular to the plates and is given by:

$$\dot{\varepsilon} = \frac{du}{dy} \quad [s^{-1}] \tag{2.5}$$

In many fluids, the flow speed varies linearly from 0 at the bottom plate to the maximum velocity u at the top. It must be noticed that the fluid applies to the top plate a force directed opposite to its motion, and a force of equal magnitude but opposite direction to the bottom plate. Therefore, an external force must be applied in order to keep the top plate moving at a constant velocity.

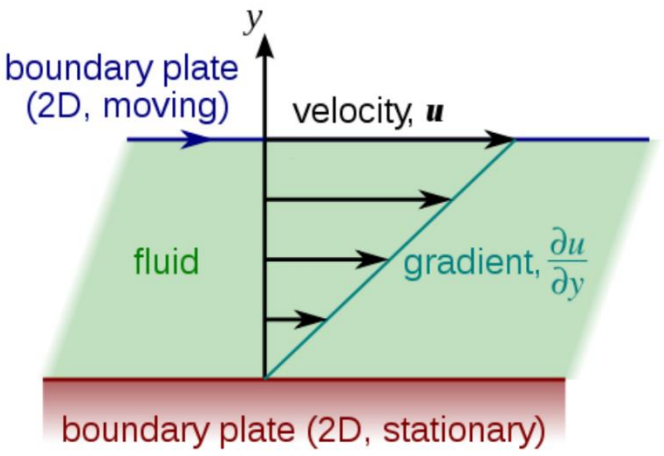

Figure 2.3: Graphical illustration of the planar Couette flow. Since the friction between adjacent layers of the fluid opposes to the shearing flow, a force must be imposed in order to have the upper plate moving at a constant velocity. The magnitude of this force is related to the fluid viscosity.

Lastly, the material rheological behavior and the perception that we have of it strongly depend on the relation between the time of force application and the observation time. This characteristic was well pointed out by Marcus Reiner, a professor at Technion in

Israel, who, referring to the phrase *"The mountains flowed before the Lord"* (Libro dei Giudici, 5, 5) pronounced by the prophetess Deborah, commented in this way [80]:

"Deborah knew two things. First that the mountains flow, as everything flows. But, secondly, that they flowed before the Lord and not before man, for the simple reason that man in his short lifetime cannot see them flowing, while the time of observation of God is infinite."

Reiner observed that given enough time even a solid-like material can flow. Similarly, a fluid-like material can behave as a solid when it is deformed rapidly enough. These observations can be expressed by means of the so-called *Deborah number* [81] De, which is defined by the ratio between the relaxation time t_R, i.e. the time required by the material constitute molecules to respond and adjust to the external perturbation, to the observation time t_{obs} (or, alternatively, the force application time or the measurement characteristic time). For example, the relaxation time t_R vanishes for a purely viscous fluid such as water, while it is infinite for a Hookean elastic solid.

$$De = \frac{t_R}{t_{obs}} \tag{2.6}$$

According to the value assumed by this parameter, it is possible to classify the materials in three main groups, that will be presented in the next sections. A material behaves like a liquid (liquid-like behavior) if it displays a really fast response ($De \ll 1$), while it behaves like a solid (solid-like behavior) if the response is really slow ($De \gg 1$). The situation in which the two times are comparable ($De \sim 1$) is the one described by viscoelastic materials, which shown properties in between purely viscous fluids and purely elastic solids.

2.2 Elastic solids and viscous fluids

This section will briefly report the basic theory and the constitutive equations that describe the behavior of elastic solids and viscous fluids, with particular attention to the description of Newtonian and non-Newtonian fluids.

2.2.1 Elastic solids

The constitutive equation that describes the behavior of a purely elastic solid is given by the Hooke's law, which postulates a linear relation between the stress σ and the strain ε, as it is expressed by the following relation:

$$\sigma = E\varepsilon \tag{2.7}$$

where the proportionality constant E ([Pa]) is called *elastic modulus* (even called *Young's modulus*) and represents the resistance opposed by the solid to the deformation. The reciprocal of the elastic modulus is called *compliance* J ([1/Pa]) and accounts for the ductility of the material. The previous equation is valid for a normal stress. In case a shear stress is applied, a similar relation holds in which E is simply substituted by the *shear modulus* G ([Pa]). It must be noted that the Hooke's law well describes the behavior of an elastic solid only in its linear regime, i.e. the region in which the elastic modulus is independent on the value of the applied stress or imposed strain.

In its linear regime, the response of a purely elastic material can be modelled with an elastic spring with stiffness E. When subjected to a certain stress, the spring will deform immediately according to Equation 2.7 and will store a certain amount of elastic energy, which will be released once the stress is removed. It is worth noticing that the elastic solid has the feature of having its response to an external stimulus perfectly in phase with the stimulus itself. For example, under the assumption of a linear response, if a sinusoidal stress at a certain frequency is imposed on a purely elastic material, the resulting strain will show a sinusoidal response with the same phase and frequency of the stress.

2.2.2 Newtonian and non-Newtonian fluids

As for the elastic modulus in case of an elastic solid, the viscosity η ([Pa·s]) of a fluid represents the resistance of a fluid to flow at a given shear rate. It is possible to divide the fluids in two main categories, according to the dependence of the viscosity on the shear rate. In case the viscosity does not depend on the shear rate, the fluid is called Newtonian and it obeys to the constitute equation called Newton's law of viscosity:

$$\sigma = \eta\dot{\varepsilon} \tag{2.8}$$

Examples of Newtonian fluids are water, glycerol and their mixtures. According to the previous equation, the shear stress and the shear rate have a linear relation and the proportionality constant is given by the viscosity, which represents the slope of the line in

a shear stress-shear rate graph. It is possible to model a Newtonian fluid with a viscous dash-pot, i.e. a piston-cylinder arrangement, filled with a viscous fluid. A strain is achieved by dragging the piston through the fluid by applying a certain stress to it and the system responds as described by Equation 2.8. The flowing behavior is obviously irreversible, therefore, once the stress is removed, the piston does not come back to its original position. This is because the energy is not stored as in the elastic case, but it is dissipated due to the internal friction. Therefore, it is possible to say that in case of elastic solids the energy is stored when subjected to an external stress, whereas in case of viscous fluids the energy is dissipated. Lastly, if a sinusoidal stress at a certain frequency is imposed on a purely viscous fluid, the resulting shear rate will show a sinusoidal response with the same phase and frequency of the applied stress. This implies that the strain is in quadrature of phase with respect to the stress.

In case the fluid viscosity is not constant as a function of the shear rate, the fluid is called non-Newtonian fluid. This class of fluids can exhibit a viscosity which is an increasing or decreasing function of the shear rate. Examples of non-Newtonian fluids can be found among food products: ketchup, for example, becomes less viscous when it is shaken while corn starch mixed with water becomes thicker in response to an external force. Other examples of non-Newtonian fluids are shampoo, blood, mustard and toothpaste. For a non-Newtonian fluid, the relation between the shear stress and the shear rate does not follow the Newton's law of viscosity. Moreover, this kind of fluids can exhibit even a time-dependent viscosity. A simple mathematical relation that is widely used to describe the behavior of these fluids is called *Ostwald-de Waele* (or *power-law fluid*) relationship, which is given by:

$$\sigma = K(\dot{\varepsilon})^n \tag{2.9}$$

where K is called *flow consistency index* ([Pa·s^n]), which is a quantity proportional to the viscosity, and n is a dimensionless number called *flow behavior index.* For this class of fluids it is possible to define an *apparent* or *effective viscosity*, given by:

$$\eta_{eff} = K(\dot{\varepsilon})^{n-1} \tag{2.10}$$

The power-law fluids can be divided in three categories depending on the value assumed by the flow behavior index n. For $n = 1$, Equation 2.9 reduces to Equation 2.8, with K equal to the fluid viscosity η and, in this case, the power-law model is used to describe a simple Newtonian fluid. For $n < 1$ the fluid is called *shear thinning* or *pseudoplastic* and its viscosity is a decreasing function of the shear rate. In the opposite situation, $n > 1$, the

fluid is called *shear thickening* or *dilatant* and it is characterized by a viscosity which is an increasing function of the shear rate. A graphical representation of the three different regimes described by the Ostwald-de Waele relationship is shown in Figure 2.4.

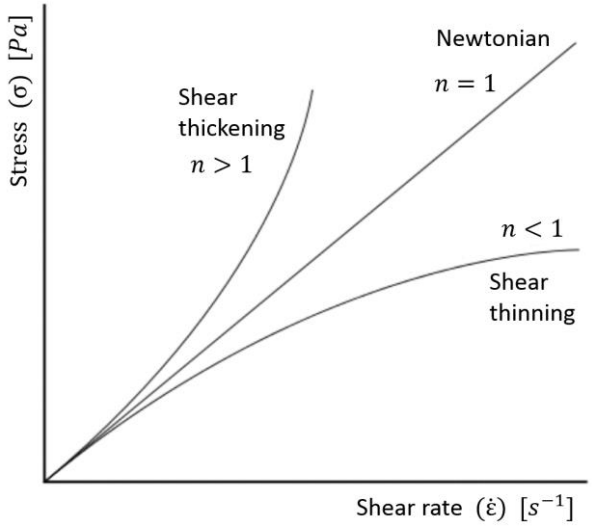

Figure 2.4: Shear stress-shear rate curves and classification of fluids according to the Ostwald-de Waele relationship.

As it can be seen, in case of a Newtonian fluid the shear stress is linearly proportional to the shear rate and the viscosity (the slope of the curve) is constant for different shear rates. Contrarily, for a non-Newtonian fluid the viscosity is not constant as a function of the shear rate, but it increases in case of a shear thickening fluid (increasing slope of the shear stress-shear rate curve) while it decreases for a shear thinning fluid (decreasing slope).

The Ostwald-de Waele relationship is well known and widely used for its simplicity, but it must be observed that it only approximates the behavior of a real non-Newtonian fluid. Considering, for example, a shear thinning fluid with $n < 1$, this model predicts that the apparent viscosity would decrease indefinitely with the increase of the shear rate. This would require a fluid with infinite viscosity at rest and zero viscosity for shear rate approaching infinite, but a real fluid has always a minimum and maximum effective viscosity. Other more precise, but even more complicated, models for describing the entire flow behavior of non-Newtonian fluids can be employed, as it will be discussed in Chapter 3 for a shear thinning fluid.

2.3 Viscoelastic materials

The vast majority of materials shows an intermediate behavior between the purely elastic solids and the purely viscous fluids previously presented. The response of these materials, called viscoelastic materials, depends on different parameters, such as the measurement time scale and the entity of the applied stress, and is characterized by a viscous and elastic contribution. Examples of everyday life viscoelastic materials are food products (ketchup, mayonnaise, yogurt), cosmetics (creams, gels, foams) and numerous other industrial products (inks, paints, rubbers) which display a different behavior depending on the using conditions.

The background theory of viscoelastic materials is really broad and an entire book would not be enough to condensate it. In the following paragraphs the basic theoretical concepts required to have a complete understanding of this thesis will be presented, starting from the description of two well-known viscoelastic models. The rest of the paragraph will be then dedicated to the presentation of two widely-used rheological tests employed to characterize the properties of viscoelastic media. The theoretical background presented in the following has been taken from [78].

2.3.1 Rheological models

As a viscoelastic material exhibits both viscous and elastic behavior, it is possible to build a model of linear viscoelasticity by considering a proper combination of linear elastic springs (for the elastic contribution) and linear viscous dashpots (for the viscous part). In particular, linear viscoelastic materials are characterized by a linear relationship between the stress and the strain at any given time. In the following, two simple and well-known models will be presented. The first model is called *Maxwell model* and it is built considering a spring and a dash-pot in series, as graphically shown in Figure 2.5.

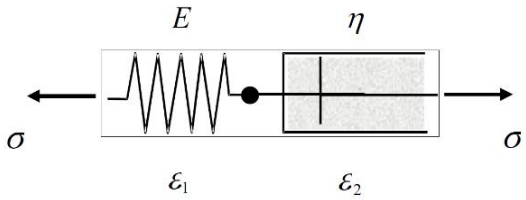

Figure 2.5: Graphical representation of the Maxwell model, built considering a linear spring and a viscous dash-pot in series [78].

Considering applying a certain stress to the system, the equilibrium condition requires that the stress must be the same in both the elements while it is possible to divide the total strain into one contribution for the spring (ε_1) and one for the dash-pot (ε_2). By

recalling the basic equations for the viscous dash-pot and the elastic spring, it is possible to write the following three equations in four unknowns:

$$\sigma = E\varepsilon_1 \quad \sigma = \eta\dot{\varepsilon}_2 \quad \varepsilon = \varepsilon_1 + \varepsilon_2 \tag{2.11}$$

In order to eliminate two unknowns, ε_1 and ε_2, it is possible to differentiate the first and third equations:

$$\dot{\sigma} = E\dot{\varepsilon}_1 \quad \sigma = \eta\dot{\varepsilon}_2 \quad \dot{\varepsilon} = \dot{\varepsilon}_1 + \dot{\varepsilon}_2 \tag{2.12}$$

By substituting the first and second equations into the third one, it is possible to derive the constitutive equation of the Maxwell model, which is given by:

$$\sigma + \frac{\eta}{E}\dot{\sigma} = \eta\dot{\varepsilon} \tag{2.13}$$

The equation is written in its standard form, i.e. the stress terms on the left and the strain terms on the right, the coefficient of σ equal to 1 and an increasing order of derivatives from left to right. The ratio η/E is called relaxation time t_R and it is a characteristic time of the material.

The second two-elements model, called *Kelvin* (or *Voigt*) *model*, consists of a spring and a dash-pot in parallel and it is schematically shown in Figure 2.6.

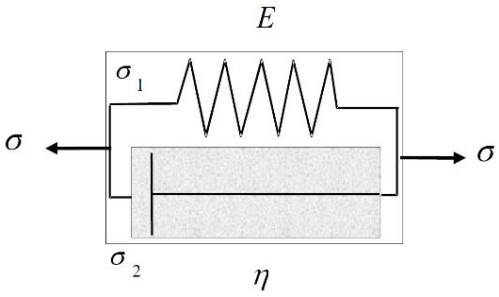

Figure 2.6: Graphical representation of the Kelvin model, built considering a linear spring and a viscous dash-pot in parallel [78].

In this configuration the strain experienced by the dash-pot is the same as the one experienced by the spring, while the total stress is the sum of the stresses in each component.

Recalling again the basic equations for the single elements and considering the expression of the total stress, it is possible to write the following three equations:

$$\sigma_1 = E\varepsilon \quad \sigma_2 = \eta\dot{\varepsilon} \quad \sigma = \sigma_1 + \sigma_2 \tag{2.14}$$

where σ_1 and σ_2 are the stresses on the spring and on the dash-pot, respectively. As before, it is possible to eliminate two of the four unknown variables, σ_1 and σ_2, and find the constitutive law describing the Kelvin model, which is given by:

$$\sigma = E\varepsilon + \eta\dot{\varepsilon} \tag{2.15}$$

The two models just presented are the simplest viscoelastic models as they include only two basic elements. These models are widely used for their simplicity. A more realistic material response can be described using more elements in series or in parallel, at the expense of an increasing complexity. Moreover, it is possible to use non-linear elements to better model the material response in case some non-linearities must be included.

2.3.2 Creep-recovery tests

The *creep-recovery test* consists in loading a material at a constant stress, maintaining the stress for a certain time and then removing it. The curve of the stress as a function of time and the strain response of a typical viscoelastic material are shown in Figure 2.7. In response to the applied stress, the material exhibits an instantaneous elastic straining. After this first phase, an ever-increasing strain over time, called *creep strain*, can be observed for all the time duration of the applied stress. For a large number of viscoelastic materials, the creep strain often increases over time with an ever-decreasing strain rate so that at a certain point a more-or-less constant strain steady-state is reached. However, there are materials for which this constant strain steady-state is never reached, even after a long stress application time. When the stress is removed, there is an instantaneous elastic recovery followed by an anelastic recovery, i.e. a certain strain is recovered over time. This anelastic strain recovery is commonly very small for metals, but it may be significant in materials based on polymeric chains. Moreover, a permanent strain may be left in the material under study, and the difference between the final and the initial strain is an indicator of the energy lost for phenomena associated to the viscous contribution. A test that is focused only on the loading part is simply called creep test.

When the loading is on, it is possible to define the parameter $J(t)$, called *creep compliance*, which is given by the following expression:

$$J(t) = \frac{\varepsilon(t)}{\sigma_0} \tag{2.16}$$

where $\varepsilon(t)$ is the time-dependent strain and σ_0 is the value of the applied stress.

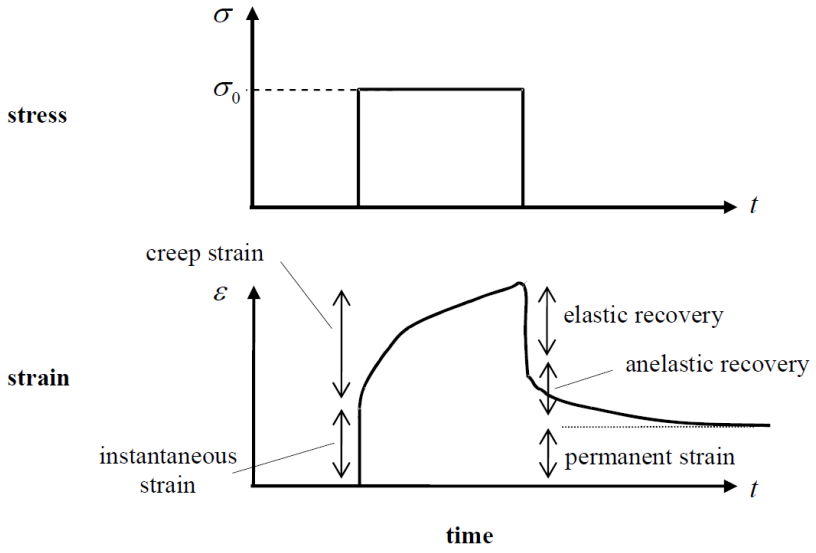

Figure 2.7: Stress and strain as a function of time for a typical viscoelastic material subjected to a creep-recovery test [78].

2.3.3 Oscillatory tests

Creep-recovery tests do not provide all the information concerning the mechanical response of viscoelastic materials. These tests usually give information and provide test data in a time range longer than some seconds, so they are well suited for long-term testing. In order to obtain a viscoelastic material characterization for short time scales, it is better to use an oscillatory approach instead of a static loading approach. This section presents the basic concepts and the main equations behind the *oscillatory tests*, which allow measuring the response of a viscoelastic material in the frequency domain [78].

Let's suppose to apply an oscillatory stress to the material of the form:

$$\sigma(t) = \sigma_0 \cos(\omega t) \tag{2.17}$$

where σ_0 is the stress amplitude while ω is the angular frequency. Under the assumption of measurements in the linear viscoelastic regime, the resulting strain will have the following expression:

$$\varepsilon(t) = \varepsilon_0 \cos(\omega t - \delta) \tag{2.18}$$

where ε_0 is the strain amplitude while δ is a phase term which is called *loss angle*. Therefore, the resulting strain will be oscillating at the same frequency as the applied stress (as the hypothesis of performing measurements in the linear viscoelastic regime was assumed, no higher frequency contributions are expected), but it lags behind by a certain phase angle δ. By expanding the strain trigonometric terms in Equation 2.18 we find:

$$\varepsilon(t) = \varepsilon_0 \cos(\delta) \cos(\omega t) + \varepsilon_0 \sin\delta \sin\omega t \tag{2.19}$$

The first term of the previous equation is perfectly in phase with the input stress while the second term is totally out of phase. If we consider the extreme situation in which $\delta = 0$, then the stress and the strain are perfectly in phase (as the case of a purely elastic solid), whereas if $\delta = \pi/2$ the stress and the strain are completely out of phase (as it happens for a purely viscous fluid).

It is then possible to define the following two parameters:

$$J' = \frac{\varepsilon_0}{\sigma_0}\cos\delta \quad J'' = \frac{\varepsilon_0}{\sigma_0}\sin\delta \tag{2.20}$$

so that it is possible to rewrite Equation 2.19 as:

$$\varepsilon(t) = \sigma_0(J' \cos\omega t + J'' \sin\omega t) \tag{2.21}$$

The quantities J' (called *storage compliance*) and J'' (called *loss compliance*) give a measure of how in phase and out of phase the stress is with respect to the resulting strain, respectively. These two quantities are usually written as the real and imaginary components of a *complex compliance* J^*:

$$J^* = J' - iJ'' \tag{2.22}$$

The same considerations can be derived by considering a stress input in the form of a sine function.

Alternatively, it is possible to consider the strain as the input and the stress as the output. In this case it is possible to write the following equations:

$$\varepsilon(t) = \varepsilon_0 \cos(\omega t) \tag{2.23}$$

$$\sigma(t) = \sigma_0 \cos(\omega t + \delta) = \sigma_0 \cos\delta \cos\omega t - \sigma_0 \sin\delta \sin\omega t \tag{2.24}$$

Even in this case, the loss angle δ is the phase angle by which the strain lags behind the stress. It follows that it is possible to write the same considerations as before for what concerns the in phase and out of phase components. Equation 2.24 can be rewritten by defining the following two new parameters:

$$G' = \frac{\sigma_0}{\varepsilon_0}\cos\delta \quad G'' = \frac{\sigma_0}{\varepsilon_0}\sin\delta \tag{2.25}$$

so that:

$$\sigma(t) = \varepsilon_0(G' \cos\omega t - G'' \sin\omega t) \tag{2.26}$$

Even in this case, these two quantities give a measure of how much the resulting stress is in phase with the input strain. The first term, G', is called *storage modulus*, while the second term, G'', is called *loss modulus*, and they are usually written as the real and imaginary part of a *complex modulus* G^*:

$$G^* = G' + iG'' \tag{2.27}$$

The complex compliance and the complex modulus are related by the following relation:

$$J^*G^* = 1 \tag{2.28}$$

Even in this situation, the same considerations can be derived by considering a strain input in the form of a sine function.

As an example, by considering the constitutive equation of the Maxwell model (Equation 2.13) in case an oscillatory stress (as described by Equation 2.17) is applied, the following expression for the complex compliance can be derived:

$$J^* = J' - iJ'' = \frac{1}{E} - i\frac{1}{\omega\eta} \tag{2.29}$$

Moreover, by taking advantage of Equation 2.28, it is possible to derive the complex modulus described by the Maxwell model in case of an applied oscillatory stress:

$$G^* = G' + iG'' = \frac{(\omega\eta)^2 E}{(\omega\eta)^2 + E^2} + i\frac{\omega\eta E^2}{(\omega\eta)^2 + E^2} \tag{2.30}$$

For "low" values of the angular frequency, the elastic component G' has a square dependence on the frequency while the viscous component G'' has a linear dependence on it. More precisely, for low frequencies the viscous component is dominant over the elastic one up to a certain angular frequency ω_c (inversely proportional to the relaxation time t_R) for which $G' = G''$ and the loss angle δ equals 45°. For angular frequencies larger than ω_c the elastic component increases up to a certain plateau value equal to E while the viscous part starts decreasing proportionally to the inverse of the angular frequency.

2.4 Rheology and microrheology

The rheological properties of a material are commonly measured by using standard devices called rheometers. A large variety of configurations have been proposed, which can be divided in two main categories: rotational and extensional rheometers. As the names suggest, rotational rheometers control the applied shear stress and measure the shear strain (or, alternatively, the opposite), whereas extensional rheometers apply an extensional stress and measure the resulting extensional strain (or, alternatively, the opposite). These devices can be used to measure different materials ranging from simple fluids, semi-solids and gels to solid systems such as polymer networks. Assessing the response of a material to an applied mechanical stress is particularly important for industrial applications in order to fine tune the material response to external conditions, during different phases of the fabrication process, to achieve the desired final performance. Rheometers can be employed for industrial applications to measure the dependence of the viscosity on the shear rate to determine the non-Newtonian behavior of the analyzed fluid or to measure the viscoelastic properties of the sample (G', G'') as a function of frequency, temperature and applied stress.

As previously written, one of the most used configurations is the rotational rheometer. In this case, the sample to be measured is placed between two plates: the lower plate is fixed while the upper plate can rotate imposing a controlled torque (*stress-controlled rheometer*) or a controlled strain (*strain-controlled rheometer*). In a stress-controlled rheometer, the strain is measured as a function of the applied stress, whereas in a strain-controlled rheometer the torque is measured as a function of the imposed strain. The upper element can have different shapes to address different measurement requirements. For example, a geometry with two parallel plates makes it possible to tune the sample thickness between the two plates, thus allowing to explore different deformation regimes as a function of the gap height between the two plates. However, the strain (and the strain rate) is not uniform in this configuration. A geometry allowing to have a uniform strain and strain rate on the measured sample is the cone-plate geometry, consisting in a fixed plate and a rotating cone that, however, must be placed at a fixed distance. These two configurations are sketched in Figure 2.8.

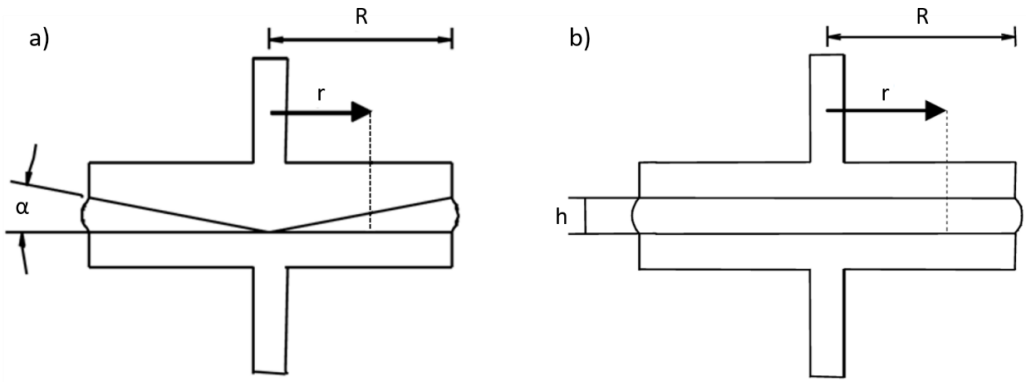

Figure 2.8: Examples of two commonly used configurations of rotational rheometers. a) cone-plate geometry, which allows obtaining a uniform strain field at the expense of a fixed working distance; b) plate-plate geometry, in which it is possible to change the distance h between the two plates, but the strain is not uniform, as it is an increasing function of the distance r from the central axis.

Rheometers allow carrying out different types of tests, such as:

- *Flow curve:* a shear rate which increases as a function of time is imposed to the material and the shear stress required to obtain such a shear rate is measured. Similarly, an increasing shear stress can be applied, and the resulting shear rate obtained from the applied shear stress is measured. Flow curve data may be presented in two different ways: shear stress versus shear rate or, alternatively, viscosity versus shear rate.
- *Amplitude sweep:* a sinusoidal strain of increasing amplitude and of constant frequency is imposed to the material in order to study the limits of the linear

regime and the onset of the nonlinear behavior. In this way it is possible to determine the storage and loss modulus as a function of the strain amplitude, which are constant in the linear regime and start decreasing for larger values of the strain amplitude, when the material enters in the nonlinear regime.

- *Frequency sweep:* a sinusoidal stress (or strain) of fixed amplitude (in the linear regime of the material) is applied and by varying the oscillation frequency it is possible to measure the storage and loss modulus as a function of frequency.
- *Creep and recovery:* a constant stress is applied to the material for a certain time and then the stress is released. The resulting strain allows estimating the conditions and time scale of the material response and relaxation.
- *Stress-relaxation:* a step deformation (strain) is applied to the material and the measurement of the stress relaxation gives information about the relaxation time of the material.

In order to measure the mechanical properties of a material with the use of a conventional bulk rheometer, a sample consumption of few mL is required. However, during the last decades, an increasing attention has been paid to the study of materials with a really low sample availability (for reasons such as high production cost, low availability of precious and biological samples, etc…), thus pushing for the development of new methods able to characterize sub-μL sample with high reliability. This research area, commonly named *microrheology*, is of particular interest for the study of bio-based and bio-inspired materials [82–84]. The common approach employed in microrheology for the investigation of the material mechanical properties is to use microbeads or nanobeads, which get dispersed in the material under study, thus acting as tracers. These tracers can be naturally present in the sample or can be externally added to the material under test. By monitoring the movement of the tracers, it is possible to infer the rheological properties of the material [4,5,85]. In case the Brownian motion of the tracers, without the application of any external force, is exploited to derive the mechanical properties of the sample, the technique is named as *passive microrheology*. This approach is nowadays largely adopted to perform rheological measurements in a wide frequency range (from fractions of Hz to few tens of kHz) on fluids and soft materials. The detection of the beads Brownian motion can be performed with different methods such as direct particle tracking [86,87], Fourier-space image analysis [88] or light scattering techniques [89]. The main limitation of passive microrheology is related to the smallest bead displacement that can be reliably detected with a given acquisition system, thus setting an upper limit to the maximum storage modulus (typically in the order of few tens of Pa) of the sample under study. A more powerful approach allowing to measure stiffer materials and to investigate the nonlinear response of the sample under study is represented by *active microrheology*, which consists in the application of a controlled external perturbation to actively move the beads. Active microrheology commonly relies on atomic force microscopy [90,91], optical forces [92,93]

or magnetic forces [94] to apply a known (and generally time varying) external force on the beads, which consequently stress the surrounding medium. For what concerns the use of optical forces, microscope-based single-beam optical tweezers have been widely employed to trap and move the tracers for materials rheological characterization [95–100]. This approach commonly allows applying forces in a restricted range going from ∼0.1 pN to some tens of pN [5], which is not enough for studying all the situations of interest for microrheology.

In addition to the limited sample consumption (in the order of few μL or less), another advantage offered by microrheology is the possibility of investigating heterogeneous materials, as the measurements are performed with a local probe in a limited area. This characteristic is of particular interest for the study of biological samples that are characterized by an inherent heterogeneity, such as in the case of cells, which cannot be obviously studied by using a bulk rheometer.

An important consideration must be pointed out for the calculation of the mechanical properties of a material in case a micrometer-sized (or nanometer-sized) tracer is used in microrheological experiments. In contrast to the classical cone-plate rheometer, in which a constant strain is applied throughout the sample under study, the strain field in a tracer-based microrheological experiment is inhomogeneous. Therefore, for a proper determination of the rheological properties of the medium, the effective area over which the force is applied and the strain field around the tracer should be calculated. For small displacements, the differential equation for the motion of a spherical tracer (with radius R) subjected to a force $f(t)$ in a viscoelastic medium is approximately given by:

$$6\pi R\eta\dot{x} + 6\pi REx = f(t) \tag{2.31}$$

where η is the viscosity, E is the elastic modulus, x is the tracer position and $\dot{x}$ is the tracer velocity [101]. The first term represents the viscous contribution given by the Stokes law, which expresses the frictional force exerted on a spherical object in a viscous fluid in a laminar flow situation (low Reynolds number). The second term represents the elastic contribution and recovery given by the elastic modulus E. In both cases, the form of the strain field is approximately incorporated in the geometric factor $6\pi R$.

3. Development of a microrheometer for shooting microrheology

After the description of the theoretical background, this chapter and the next one will be dedicated to my main PhD project: the realization of an integrated optofluidic microrheometer. In particular, this chapter will describe the development of an on-chip microrheometer for shooting microrheology realized in an optofluidic platform. The optical shooting procedure consists in exerting a step optical force on a microbead which will move in the surrounding medium stressing it. By monitoring the microbead position it is possible to infer the rheological properties of the surrounding medium. The optofluidic chip and the experimental procedure will be initially described as well as the system calibration with water. The system performance is proved by measuring different viscous media ranging from simple Newtonian fluids such as water-glycerol mixtures to more complex systems like a DNA hydrogel, which showed a strong non-Newtonian behavior. The last part of the chapter will be dedicated to the discussion of the results obtained from the measurement of yield stress fluids, a particular class of materials which exhibit a viscoelastic behavior strongly dependent on the applied stress and time scale of investigation. The proposed microrheometer allows carrying out creep and recovery measurements in an analogous way to a conventional bulk rheometer, with the advantage of requiring a significantly smaller sample volume.

The work regarding the description and validation, by means of water-glycerol measurements, of the optical shooting-based microrheometer has been reported in [102] while the results concerning the DNA hydrogel characterization have been published in [103] in the framework of my PhD activity.

3.1 Experimental procedure

This section is dedicated to the description of the experimental setup and procedure performed for optical shooting rheological measurements. The core element of the setup is an integrated optofluidic chip that has been fabricated by the Fastgroup headed by Dr. Osellame. After the description of the optofluidic chip design and fabrication, the optical shooting protocol will be then presented, and the section will end with the discussion of the optical force profile and theoretical trajectory calculation, which will be then used for the data analysis.

3.1.1 Optofluidic chip design and fabrication

As already described in Chapter 2, optical forces provide a high-precision and contactless tool to trap and manipulate microbeads suspended in a fluid. The use of microscope-based optical tweezers for rheological applications have been extensively reported in the scientific literature [95–97,104]. Optical tweezers, which rely on optical gradient forces to trap micro-objects, represent nowadays the most common microrheological approach to measure the viscoelastic properties of complex systems. In this thesis a different system configuration, based on a dual beam laser trap realized in an optofluidic platform, is proposed. The here-reported device exploits the scattering forces to trap and manipulate the position of a microbead for performing rheological measurements. A schematic representation of the integrated optofluidic chip is shown in Figure 3.1, while a photo of the same device is shown in Figure 3.2. The optofluidic chip is fabricated on a glass substrate by direct inscription of optical waveguides in a commercial microfluidic chip (Translume Inc., Ann Arbor, MI, USA) [56,105]. This commercial microfluidic chip is fabricated by FLM and chemical etching in a fused silica substrate and it embeds a straight microfluidic channel having a square section of 150 µm × 150 µm. The microfluidic channel presents an inlet and an outlet, which allow the injection and flow of the sample. In particular, two connectors are glued on the top surface of the optofluidic chip in correspondence of the microfluidic channel entrances, allowing to connect with plastic tubes the microchannel to an external micropump.

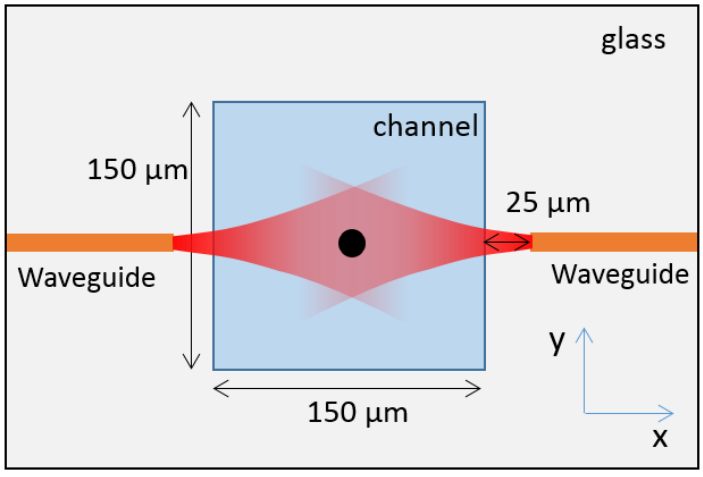

Figure 3.1: Schematic representation of the optofluidic chip used for the microrheological measurements. A microbead is trapped thanks to the optical forces exerted by two counter-propagating non-focused Gaussian laser beams, having the same optical power and emitted by two facing integrated waveguides.

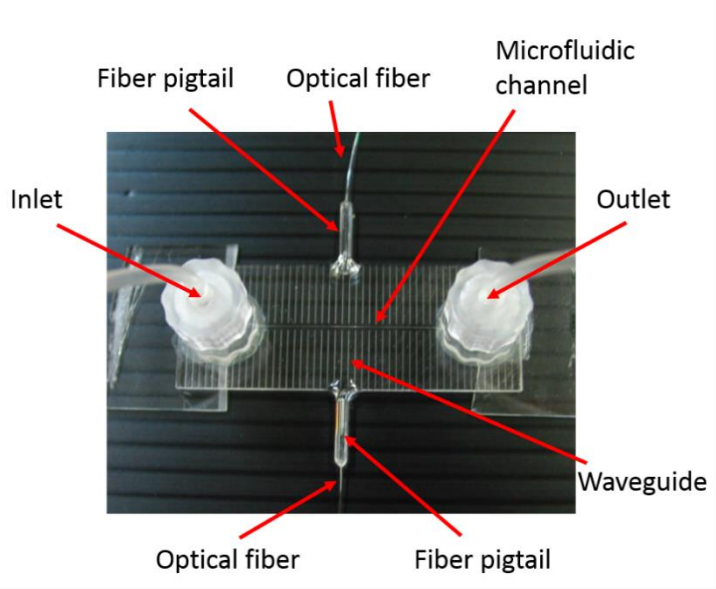

Figure 3.2: Photo of the optofluidic chip employed for the microrheological measurements. The optofluidic chip is fabricated on a glass substrate and it embeds a straight microfluidic channel with a square cross-section and with facing waveguides lying perpendicularly to the channel. Two waveguides, one for each side, are fiber pigtailed to two optical fibers in order to connect the waveguides to a laser source and bring the optical radiation inside the microfluidic channel. The microchannel presents an inlet and an outlet for the sample injection and flow.

Facing waveguides were written by FLM by the Fastgroup. The waveguides were inscribed at half height of the channel (75 µm from the channel floor) on the two sides of the microchannel, as it can be seen in Figure 3.1, which shows the cross-section of the optofluidic chip. The waveguides ending faces are separated by 200 µm, thus having a laser free propagation in the glass layer of 25 µm before the laser beams reach the microchannel section. Therefore, the microchannel results to be symmetrically illuminated from both sides. The optical waveguides were realized by focusing 150 nJ fs-laser pulses through a 50×, 0.6 NA microscope objective and by moving the chip at a scan speed of 1 mm/s (Aerotech FiberGlide translation stages). In this fabrication process it was possible to obtain optical waveguides of very good quality and single mode at 1 µm wavelength, with a mode field diameter (at 1/e) of ∼7.5 µm and propagation losses of ∼3 dB/cm. The waveguide length, on each side of the microchannel, is 8.7 mm. After the waveguides fabrication, the next step was the polishing of the chip lateral surfaces in order to achieve low fiber-to-waveguide coupling losses. Two optical fibers (Corning Hi1060) were pigtailed to the optofluidic chip in correspondence to the desired waveguides with an estimated coupling loss of ∼1.3 dB. The final dimensions of the optofluidic chip are 50.8 × 17.6 × 1.1 (length × width × height, in [mm]). As it will be demonstrated, the high level of integration of the device ensures a high measurement repeatability and stability. Moreover, the portability

of the device makes it possible to easily move it from one lab to another in order to build a new setup. The two counter-propagating optical beams emitted by the two facing waveguides can be used to trap a microbead and manipulate its positions, as shown in Figure 3.1, where a microbead is trapped in the center of the microchannel thanks to the optical forces exerted by two beams carrying the same power. By unbalancing the power emitted by one of the two waveguides it is possible to change the microbead trapping position and hence to move the microbead along the beam axis (x direction) toward the new equilibrium position. This concept will be the conceptual basis for the realization of an integrated dual beam laser trap microrheometer.

3.1.2 Experimental setup

A schematic of the experimental setup for shooting microrheology is shown in Figure 3.3. The sample is prepared by mixing in a vial a small amount of microbeads (of known dimensions and optical properties) into the fluid of interest. A standard micropipette can be used to inject the prepared sample into the microfluidic chip reservoir. A sample volume lower than 1 µL is required for an entire set of measurements. The fluid movement inside the microfluidic channel is governed by capillarity, but it can be precisely controlled thanks to a LabVIEW-driven micropump (MFCS-FLEX 3C, Fluigent), which is connected to a microfluidic channel entrance with a plastic tube screwed to a chip connector. In this way the pressure inside the microchannel can be controlled in real time. The optofluidic chip is positioned on a phase-contrast inverted microscope (Nikon ECLIPSE TE2000-U), which allows monitoring the microbead movement thanks to a charge-coupled device (CCD) camera connected to the microscope. The setup is equipped with a temperature control system, consisting of a small Peltier module placed just below the optofluidic chip and a thermocouple (TC) well fixed on the top surface of the chip, which generates the feedback signal for the Peltier cell. A piezoelectric transducer (a thin piezoceramic disk) is positioned under the chip and it is driven by a function generator (Aim-TTi TG 2000 20MHz) controlled by a LabVIEW program. As discussed in Section 1.3, by driving the piezoelectric transducer at the right resonance frequency, it is possible to generate an acoustic standing wave in the microfluidic channel with a single node in the channel center. The acoustic radiation force will thus push all the microbeads along the central axis of the microfluidic channel (acoustophoretic prefocusing toward the center of the channel cross-section). A better coupling of the acoustic waves from the piezoelectric transducer to the glass optofluidic chip can be obtained by adding a glycerol drop between the transducer and the glass chip. For what concerns the optical part of the setup, a CW Yb-doped fiber laser (YLD-10-1064, IPG Photonics, P_{max} = 10 W at 1070 nm) is employed as optical source and connected to a 50:50 fiber power splitter (FPS). Two single-mode optical fibers are used to couple the radiation in output from the two ports of the FPS to the optical

waveguides integrated in the optofluidic chip, and two fiber-to-fiber U-benches are inserted along the optical paths, allowing a full control of the optical power in the two branches. In particular, a manually-controlled variable attenuator is inserted in one U-bench while the other U-bench is equipped with a beam blocker driven by a motorized stage, which allows to block/unblock the optical beam in a controlled and fast way. The motorized stage, as well as all the other instrumentations, are controlled thanks to a custom LabVIEW program.

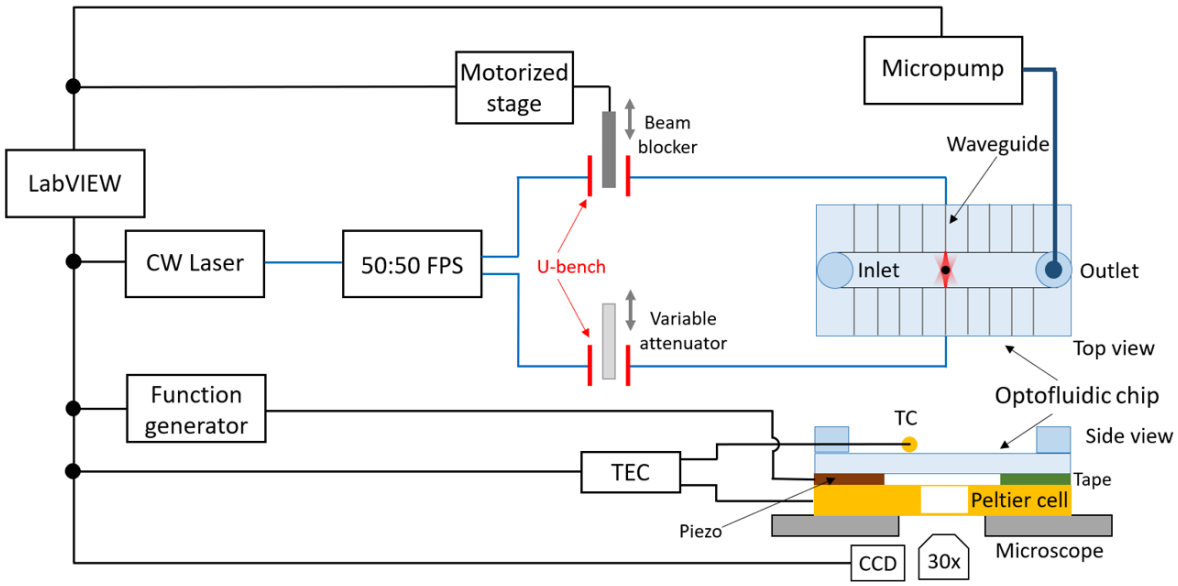

Figure 3.3: Schematic diagram of the experimental setup. The blue lines represent the optical fiber connections while the black lines represent the electrical cables. TEC: temperature controller circuit; CCD: charge-coupled device; TC: thermocouple; FPS: fiber power splitter.

3.1.3 Optical shooting protocol and data acquisition

After the sample injection in the microchannel, the pressure is adjusted by means of the micropump in order to produce a suitable flowing speed of the fluid. The first step consists in trapping a single microbead thanks to the laser radiation emitted by the facing waveguides. Let's suppose to have a dispersion of microbeads in water: the microbeads will tend to sink toward the channel bottom surface due to gravity, with the consequent impossibility to trap them by means of the optical radiation, as the waveguides are located at half height of the microchannel. In order to solve this issue, it is possible to exploit the acoustophoretic prefocusing so that to push the microbeads toward the channel center. A sinusoidal voltage can be applied by means of the function generator to the piezoelectric transducer and by selecting a proper oscillation frequency it is possible to impose an acoustic standing wave in the microfluidic channel with a single node in the channel center, as previously described in Section 1.3.2. In the considered case of a microchannel with a

square cross-section geometry (150 × 150 μm^2) filled with water (speed of sound in water $c_f = 1483\ m/s$), the resonant frequency $f_{1,0}$ and $f_{0,1}$ will have the same value, e.g. 4.9434 MHz. By driving the piezoelectric transducer at around this frequency, both the resonance contributions, along the width and height of the channel, will be present simultaneously and the combined effect is a single node position in the channel center. In this way all the microbeads will be aligned along the central axis of the microchannel and one single microbead can be trapped by means of the laser radiation. Once a microbead is optically trapped, the acoustic radiation is turned off and the flow is stopped by means of the micropump. It must be pointed out that when the microbead is illuminated by the two laser beams, the gradient forces tend to automatically align the microbead along the common beam axis, where the gradient force is zero and only the scattering component of the force is present. Therefore, once the microbead is aligned on the optical axis, only the scattering forces exerted by the two laser beams are responsible of the microbead movement and trapping in the equilibrium position along the common beam axis. This represents a substantial difference with respect to conventional microscope-based single-beam optical tweezers. In the here-proposed configuration, if the two laser beams have the same power, the trapping position is in the center of the microchannel, as shown in Figure 3.4 a). In this situation the two optical beams exert two scattering forces on the microbead which have the same magnitude and opposite direction (represented by the black arrows in Figure 3.4 a)) and hence the net force acting on the microbead is zero, meaning that the microbead is trapped in an equilibrium position.

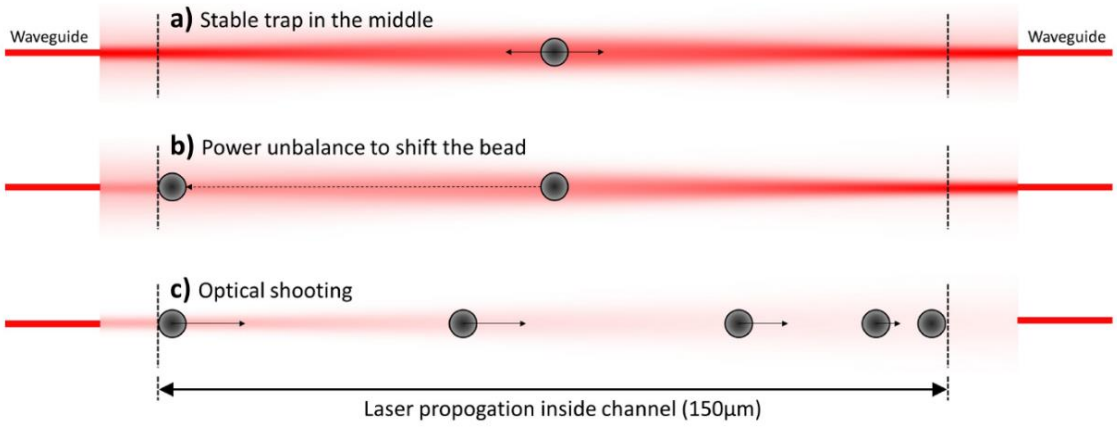

Figure 3.4: Optical shooting experimental procedure. a) A single microbead is trapped by two counter-propagating laser beams carrying the same optical power; b) the trapping position is shifted toward the left border by decreasing the power emitted by the left waveguide; c) once the microbead is stably trapped closer to the left border, the right laser beam is abruptly blocked and the microbead will be pushed by the power emitted from the left waveguide from the left to the right border across the whole channel (optical shooting) [102].

In order to perform the optical shooting experiment, the laser power emitted by the left waveguide is decreased by increasing the optical attenuation in the corresponding U-bench by means of the manually controlled variable attenuator. The microbead consequently moves toward the left border, reaching a new stable trapping position, as shown in Figure 3.4 b). Then, the right laser radiation is abruptly blocked by the beam blocker in the corresponding U-bench, thanks to the actuation of the LabVIEW-controlled motorized stage. The microbead is therefore pushed by the laser power emitted from the left waveguide from the left to the right side, across the whole channel, and we called this procedure optical shooting (see Figure 3.4 c)). By unblocking the right laser radiation, the microbead is pushed back toward the left border, in the previous stable trapping position and the optical shooting can be repeated by inserting again the beam blocker. The optical shooting procedure is repeated several times with the same microbead in order to increase the data statistics. It is then possible to change the fluid temperature thanks to the temperature control system by actuating the Peltier module and waiting some minutes for the fluid temperature stabilization. Optical shooting measurements can be performed at different temperatures to study the viscosity dependence of the fluid under test. After a complete campaign of measurements, the microbead can be released and a new one can be trapped in order to perform measurements with a new tracer.

During the optical shooting procedure, the entire microbead movement is monitored thanks to the CCD camera connected to the inverted phase-contrast microscope. Thanks to the phase contrast mode, the microbead image presents a bright spot in the center, which allows identifying the microbead center and thus tracking the microbead position in an accurate way. The LabVIEW program employed for the setup management also allows the real-time extraction of the microbead trajectory from the optical shooting experiment thanks to a tracking algorithm, as it is shown in Figure 3.5. A stack of some images acquired by the phase-contrast microscope shows the positions sequentially occupied by the microbead during the shooting experiment at equally-space time intervals, as indicated by the red numbers. The corresponding microbead position as a function of time, retrieved with the particle tracking algorithm, is shown in the image below.

An interesting feature offered by the real-time monitoring of the microbead position is that it allows evaluating and solving possible issues affecting the measurements such as an unstable laser power or a residual fluid flow. As it can be noticed, the microbead velocity is not constant along the trajectory across the channel and this depends on the shape of the optical force profile, as it will be discussed in the next section.

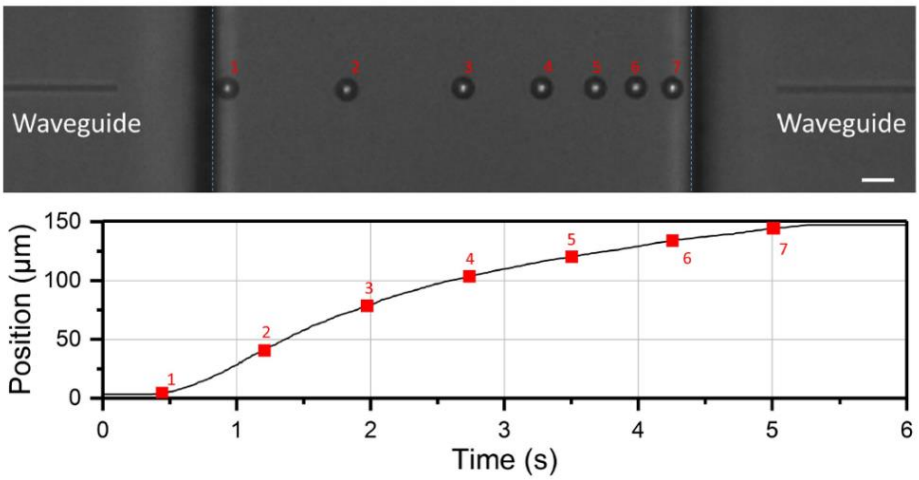

Figure 3.5: Stack of phase-contrast microscope images showing the sequential microbead positions at equally-spaced time intervals during an optical shooting experiment (scale bar: 10 µm). The bright spot in the microbead center allows an accurate tracking of the microbead position. The extracted microbead position as a function of time is shown in the image below [102].

3.2 Governing equations and system calibration

In this section the basic equations for determining the viscosity of the fluid under test will be presented together with the calculation of the optical force profile and the theoretical microbead trajectory. At the end of this section, the calibration of the optical force inside the optofluidic system will be discussed.

3.2.1 Fluid viscosity derivation

As previously explained, during the optical shooting experiment the microbead is pushed by the scattering force F_S exerted by the left waveguide, as shown in Figure 3.4 c). The scattering force profile, its dependence on the spatial coordinate x inside the microfluidic channel and its calculation according to the PRO approximation will be discussed in the next paragraph. When the microbead, pushed by the scattering force, moves inside the fluid, it also experiences the Stokes drag force, a frictional force which opposes to its movement. In case of a spherical object moving in a viscous fluid inside a microfluidic channel, the Stokes drag force F_{drag} is given by the following expression:

$$F_{drag} = 6\pi\eta R\dot{x}/\gamma \tag{3.1}$$

where η is the fluid viscosity, R is the microbead radius, $\dot{x}$ is the microbead velocity and γ is a correction parameter that accounts for the effect of the hard walls of the microfluidic channel and is defined as:

$$\gamma = 1 - \frac{9}{16}\frac{R}{d} + \frac{1}{8}\left(\frac{R}{d}\right)^3 - \frac{45}{256}\left(\frac{R}{d}\right)^4 - \frac{1}{16}\left(\frac{R}{d}\right)^5 \tag{3.2}$$

in which d is the distance from the microfluidic chip surface [106]. For the microbeads radii considered in this thesis, the contribution of γ is always negligible in case the microbeads are at least few micrometers away from the microfluidic chip surface. As the microbead positions closer to the channel walls are always discarded in the data analysis, it is possible to neglect the γ correction, as $\gamma \cong 1$ for microbead positions sufficiently far from the channel wall. In case non-Newtonian fluids are considered, Equation 3.1 can still be used by simply substituting the viscosity η with the proper apparent viscosity η_A of the considered non-Newtonian fluid.

The inertial effects during the movement of the microbead inside the microfluidic channel can be neglected due to the extremely low Reynolds number ($< 10^{-3}$). Therefore, in each position and instant of time during the microbead movement, the optical scattering force will be equal to the Stokes drag force:

$$F_s(x) = F_{drag}(\dot{x}) \tag{3.3}$$

The scattering force $F_s(x)$ presents a spatial dependence on the x coordinate along the beam propagation axis, while the Stokes drag force depends on the microbead velocity $\dot{x}$. Therefore, the microbead will move with a position-dependent velocity that is always equal to the speed limit in the considered medium. Thanks to the fact that the scattering force profile $F_s(x)$ can be calculated by means of numerical simulations based on PRO approximation, and by considering that the microbead radius R is known, it is possible to numerically derive the curve of the microbead position as a function of time by assuming a certain value for the fluid viscosity. This curve, numerically calculated for a certain "guess" of the fluid viscosity, will be named as *theoretical bead trajectory* in the following. The value of the viscosity of the fluid under test can be determined by the best fit of the experimentally measured bead trajectory with the simulated theoretical bead trajectories.

3.2.2 Optical force profile and theoretical bead trajectory

For the optical shooting microrheological measurements, standard PMMA microbeads (Bangs Laboratories, Inc. BB01N), having radius equal to 5 µm and refractive index of 1.48 (@ 1070 nm), were initially used as tracers in different fluids such as milli-Q water and water-glycerol mixtures. In order to perform the system calibration and validation, the scattering force profile must be initially calculated so that to numerically derive the theoretical bead trajectories for fitting the experimental bead curve and hence determining the fluid viscosity. In our system configuration, the bead is automatically centered along the beam optical axis thanks to the gradient force and the scattering force is the only force component responsible of the bead optical shooting. In particular, the laser beam emitted by the optical waveguide inscribed in the optofluidic chip is a non-focused Gaussian laser beam having a wavelength of 1070 nm. Both the waveguides emit an optical beam with a beam waist equal to 3.8 µm (characterized with previous experiments), which diverges upon propagation in the channel. As discussed in Section 1.2.2, the PRO approximation can be assumed for the calculation of the theoretical force profile in the microfluidic channel. Figure 3.6 a) shows the theoretical calculation of the scattering force $F_s(x)$ (as a function of the space coordinate x along the channel width) applied by the left laser beam with an optical power of 10 mW on a PMMA microbead suspended in water ($n = 1.325$ at 1070 nm) and in ethanol ($n = 1.354$ at 1070 nm), respectively. As it can be noticed, a change of the refractive index of the medium significantly impacts the optical force magnitude. In particular, the scattering optical force applied to the microbead is larger when the refractive index difference between the microbead and the medium is higher. It can also be noticed that the optical force profiles in water and ethanol have a similar behavior: the force initially increases, it reaches a maximum and then it continuously decreases. Only a small shift in the maximum-force position can be observed and this is due to a change in the optical beam divergence. In Figure 3.6 b), the scattering force profiles calculated with the same microbeads in water for different values of the optical power are shown. As the total scattering force is obtained by summing the contributions of all single rays, which are directly proportional to the optical power, all the scattering force profiles are simply scaled copies of the same curve.

From the calculated optical force profile, the corresponding theoretical bead trajectory can be derived, as discussed in Section 3.2.1, provided that the viscosity of the fluid surrounding the microbead is known. In Figure 3.6 c), d) the calculated theoretical bead trajectories corresponding to the scattering force profiles reported in Figure 3.6 a), b) are shown, respectively. A first observation is that the starting and ending positions of the bead trajectories are equal to 5 µm and 145 µm, respectively, as the microbead radius equals to 5 µm. Moreover, all the trajectories reported in Figure 3.6 d) can be overlapped by rescaling the time axis by a factor corresponding to the optical power considered in the

force profile calculation. This consideration, which may appear not so important, is particularly significant as it allows monitoring the presence/absence of viscosity changes induced by the laser heating effect, which is due to the absorption of the optical power by the fluid with the consequent material heating. In particular, in case of no laser heating effect and hence constant viscosity in a Newtonian fluid, the experimental optical shooting trajectories measured at different power levels should overlap with a proper rescaling of the time axis, whereas a deviation should be expected in case of laser heating-induced viscosity changes.

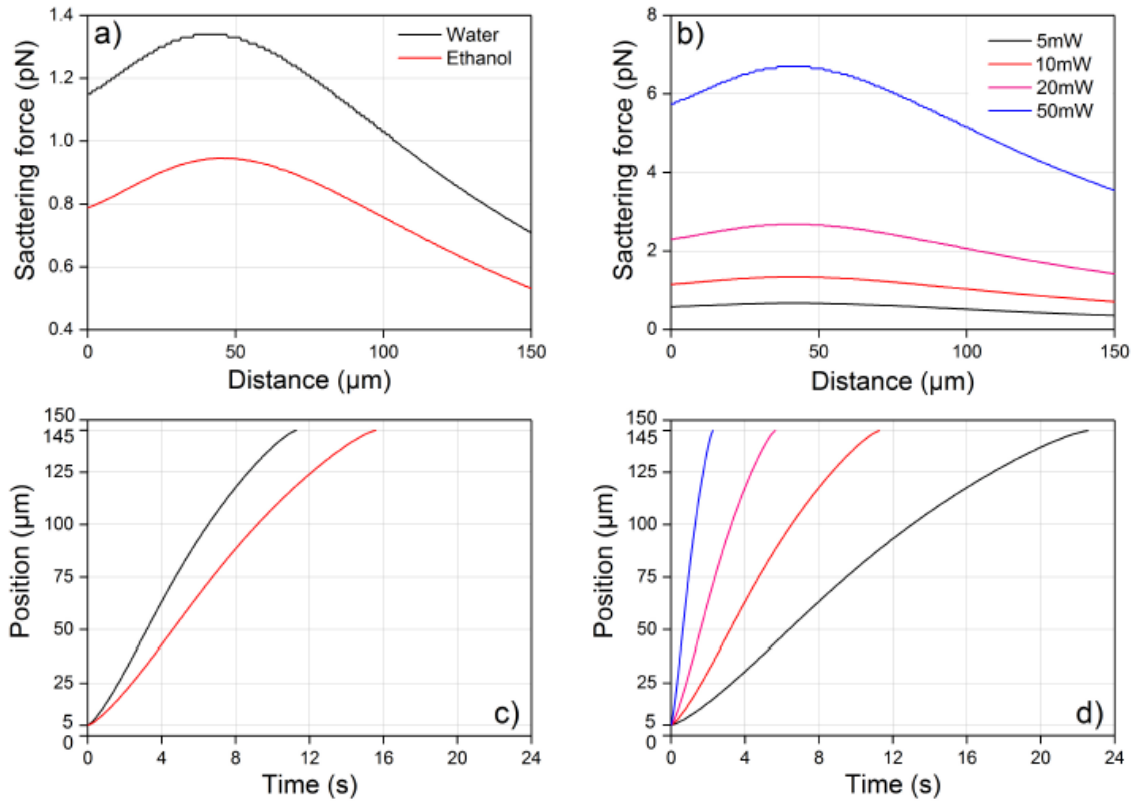

Figure 3.6: Theoretical calculation of the scattering forces exerted by the left waveguide on a 5 μm radius PMMA microbead and corresponding theoretical bead trajectories [102]*. a) Scattering force profile along the microfluidic channel width for a laser beam having an optical power of 10 mW in water and ethanol. b) Scattering force profile in water calculated for different laser powers. c) and d) Theoretical bead trajectories calculated according to the scattering force profiles a) and b), respectively.*

The calculation of the optical force profile resulting from two facing laser beams impinging on a dielectric microbead was then carried out. The same conditions as in Figure 3.6 b) are considered, i.e. a 5 μm radius PMMA microbead suspended in water. Different optical powers from the two facing laser beams are investigated and the results are shown in Figure 3.7. Figure 3.7 a) reports the effect of an unbalanced power level between the

two beams on the overall force profile. The labels next to the force curves indicate the optical powers carried by the left (L) and right (R) laser beams. The nominal power is set equal to 10 mW (L and R refer to an optical beam carrying 10 mW of optical power) and fractions of this reference power are indicated by the curve labels. In case the scattering force is positive, the microbead will be pushed toward the right direction, whereas if the force is negative the bead will be pushed toward the left direction. Stable trapping positions correspond to points where the optical force profile crosses the zero line with negative derivative in the adjacent region. Considering, for example, two counter-propagating laser beams carrying the same power ("L+R" in Figure 3.7 a)), the force profile crosses the zero value, with negative derivative, exactly in the middle of the microfluidic channel. This results in a stable trapping position in the middle of the channel, corresponding to the bead trapping configuration shown in Figure 3.4 a). In order to perform the optical shooting experiment, the microbead trapping position is initially shifted toward the left channel border by introducing an attenuation in the left-branch U-bench, so that the microbead moves toward the new trapping position, paying attention it does not get in contact with the channel wall. The shift of the trapping position toward the left border can be even seen in Figure 3.7 a) for the curve labelled "2L/3+R", for which the left power is decreased with the subsequent left-shift of the stable trapping position. Thanks to this configuration it is possible to obtain a repeatable and precise starting position for all the optical shooting trajectories, even when the optical power emitted by the laser is changed, as the trapping position depends only on the ratio of the power levels from the two sides and not on the absolute value of the power, as it can be appreciated in Figure 3.7 b).

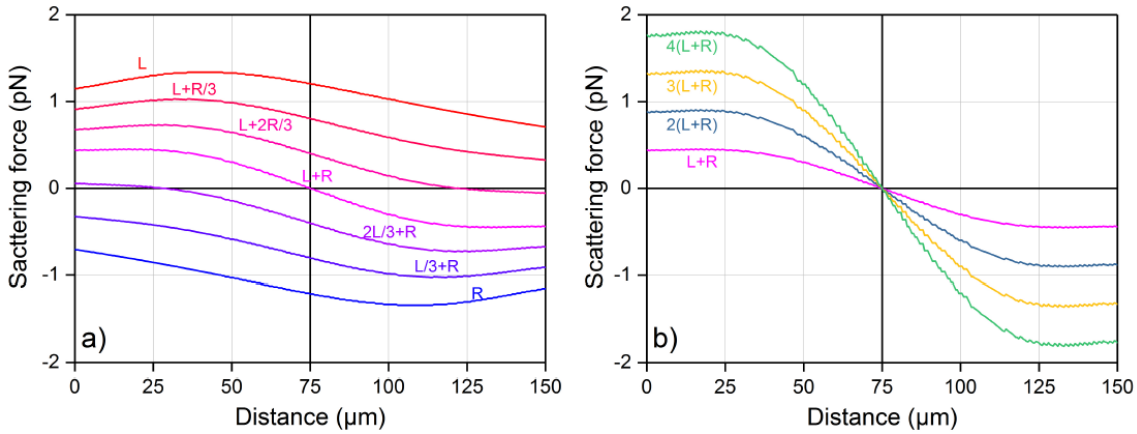

Figure 3.7: Optical force profile, as a function of the position in the microchannel, calculated for two counter-propagating laser beams impinging on a 5 μm radius PMMA microbead suspended in water [102]. *Capital letter "R" stands for the right laser beam while "L" refers to the left laser beam. The optical power carried by the two laser beams is varied as indicated by the labels next to the force curves. The nominal power is set equal to 10 mW ("L" and "R") and fractions of this reference power are indicated by the curve labels.*

3.2.3 System calibration and data fitting procedure

As previously discussed, the scattering force depends on the optical power carried by the laser beam in the microfluidic channel. The optical power emitted by the laser source can be controlled by varying the laser current I_L. However, the optical power inside the microfluidic channel is a priori unknown as the optical power emitted by the laser source undergoes different optical losses due to, for example, the propagation in the optical fibers and in the microchip waveguides. Therefore, a calibration procedure must be carried out in order to determine the optical power P_{chip} effectively present inside the microfluidic channel, which will be related to the set laser current I_L by the relation $P_{chip} = AI_L$, where A is a calibration constant to be found. Obviously, the previous relation is valid only for laser currents larger than the laser current threshold, which is around 0.75 A for the employed laser source. Considering this optical power dependence, the scattering force will be given by the following relation:

$$F_s(x, I_L) = AI_L f(x) \tag{3.4}$$

where $f(x)$ is the optical force profile, which can be calculated numerically. In order to determine the calibration constant A, it is possible to perform optical shooting experiments in fluids of known viscosity such as milli-Q water. Optical shooting experiments allow acquiring the space-time curves $x(t)$ corresponding to the microbead trajectories resulting from the particle tracking. As previously discussed and recalling Equation 3.3, in the considered case of a purely viscous fluid such as milli-Q water, the optical force will be balanced by the viscous friction:

$$F_s(x, I_L) = 6\pi\eta R\dot{x} \tag{3.5}$$

Since the optical force $F_s(x, I_L)$ depends on the bead position x, but not on the time instant t, it is possible to separate the two variables in order to obtain an equation that can be integrated between the initial space-time coordinates (x_i, t_i) and those relative to a generic instant of the shooting experiment (x^*, t^*):

$$\int_{t_i}^{t^*<t_f} dt = \int_{x_i}^{x^*<x_f} \frac{6\pi\eta R}{AI_L f(x)} dx \tag{3.6}$$

where (x_f, t_f) represent the final space-time coordinates of the acquired data and the expression of the scattering force $F_s(x, I_L)$ has been made explicit. The determination of

the calibration constant A can be performed introducing the function $T(x^*, t^*, x_i, t_i, \eta, A)$, which is given by:

$$T(x^*, t^*, x_i, t_i, \eta, A) = \int_{t_i}^{t^*<t_f} dt - \frac{6\pi\eta R}{AI_L} \int_{x_i}^{x^*<x_f} \frac{dx}{f(x)} \tag{3.7}$$

It must be pointed out that in the previous equation the microbead radius is known, as well as the force profile $f(x)$, which can be calculated numerically. The value of the current I_L, at which the optical shooting experiment is performed, is recorded for each measurement and hence it is a known parameter too. By performing experiments on a fluid with known viscosity η (e.g. milli-Q water at various controlled temperatures), it is possible to determine the value of the calibration constant A by minimizing the value of $\int_{t_i}^{t_f} T^2 dt^*$, i.e. by finding the value of A which gives the best fit of the experimentally measured bead trajectories with the simulated ones. The calibration protocol was repeated before and after every measurement campaign to verify the stability of the system. The measurement setup was found to be very stable: the difference between the calibration constant evaluated before and after each measurement campaign was always found to be less than 3%. The main reasons of this measurement repeatability can be found in the laser source stability and in the monolithic integration and alignment between the optical components and the microfluidic device.

Conversely, once the calibration constant A has been determined, the viscosity η of an unknown fluid can be derived through exactly the same minimization procedure, i.e. by determining the value of η which gives the best fit of the measured bead trajectories with the simulated ones.

3.3 System validation: water-glycerol mixtures

After the system calibration with milli-Q water, the integrated microrheometer was tested by measuring water-glycerol mixtures at different concentrations and different temperatures. These solutions are very well studied systems and their viscosity dependence on temperature is well known from literature [107]. Therefore, the comparison of the viscosity measurements with our integrated microrheometer with data from the scientific literature allows testing the performance of the here-proposed device. Water-glycerol solutions have been chosen as benchmark materials to validate the proposed microrheometer for different reasons. First of all, these solutions can be prepared by simply mixing water and glycerol at the desired concentration. Laboratory equipment such as an ultrasonic bath, a magnetic stirrer and a vortex mixer can be used to

properly mix the solutions. Another reason is that by changing the glycerol content in mass it is possible to change the viscosity of the final solution going from the viscosity of water (0% glycerol) to around 1000 times the viscosity of water at room temperature (100% glycerol). Moreover, the viscosity of these solutions exhibits a strong variation with temperature, which can be useful to test the temperature controller circuit in the setup.

Water-glycerol mixtures at different mass concentrations were prepared and measured using 5 µm radius PMMA microbeads as tracers. Optical shooting measurements have been carried out at different temperatures by actuating the Peltier module placed below the optofluidic chip. As in the case of water, the optical shooting experiments were repeated several times with the same tracer for each temperature, and then repeated with new tracers in order to increase the statistics of the acquired data. The data analysis and the viscosity derivation were performed as described at the end of the previous section, after the system calibration with water and the numerical calculation of the scattering force profiles for each water-glycerol mixture. As the refractive index of a water-glycerol mixture changes by varying the glycerol concentration, the numerical calculation of the scattering force profiles for each solution is a fundamental step for a proper estimation of the optical force acting on the microbead. Some examples of the acquired microbead trajectories in case of a water-glycerol mixture at 30% glycerol concentration in mass are shown in Figure 3.8, in which each curve corresponds to a single optical shooting experiment. As it can be observed, the velocity of the microbead increases by increasing the sample temperature. This is because the viscosity of a water-glycerol mixture is inversely proportional to the temperature.

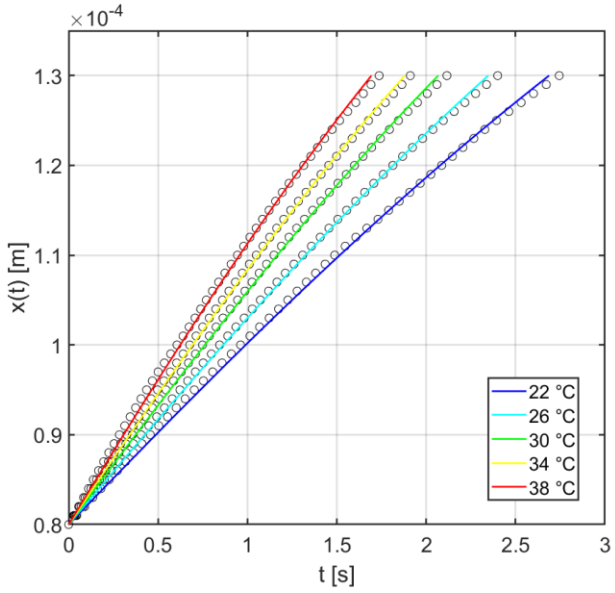

Figure 3.8: Optical shooting experiments performed on a water-glycerol mixture at 30% glycerol concentration in mass: experimentally measured microbead trajectories $x(t)$ at different temperatures (empty circles) and their fitting (colored lines) to determine the medium viscosity.

The measured viscosity values are reported in Figure 3.9 and show a good agreement with data from the scientific literature [107], indicated by the continuous lines for the different mixtures. The measurement uncertainty, calculated as the ratio of the viscosity standard deviation with respect to its average value, was found to be always lower than 8%, thus confirming the good measurement repeatability.

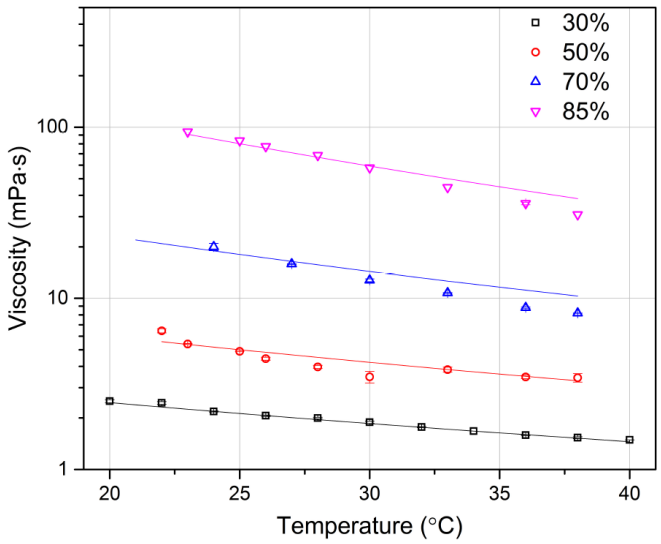

Figure 3.9: Results from the viscosity measurements of water-glycerol mixtures at different mass concentrations and different temperatures. The experimental data, represented by scatter symbols, are compared with theoretical values from scientific literature [107]*, represented by continuous lines. The legend indicates the glycerol percentage in mass for the considered mixture.*

As it can be noticed, a small deviation between our measurements and data reported in the literature can be observed for the solutions at high glycerol concentration (70% and 85%). This small deviation can have different reasons such as a non-perfect mixing of the two liquids, even after multiple cycles of vortex mixing and magnetic stirring. In addition, it must be pointed out that the measurements at high glycerol concentration require a higher optical force (and hence a higher optical power) to move the tracer due to the higher viscosity with respect to mixtures at low glycerol content. This can result in a small laser heating-induced viscosity change, which is more evident in the high glycerol content solutions due to their higher viscosity dependence on temperature change. Another possible source of error can be found in the fact that the temperature readout is performed on the top surface of the optofluidic chip thanks to the thermocouple sensor. This could result in a possible error in the estimation of the real sample temperature inside the microfluidic channel.

3.4 Measurements of a DNA hydrogel

After the system calibration and validation, we decided to employ the microrheometer for measuring the rheological properties of a DNA-based hydrogel, which exhibits a more complex non-Newtonian viscosity. Non-Newtonian viscosity is a typical characteristic of multicomponent, multiscale or structured fluids such as polymer networks and colloidal dispersions. Among these systems, physical gels (e.g. solutions of associating polymers, reversible hydrogels and more generally supramolecular transient networks) commonly show a shear thinning behavior for large shear rates [108–113]. Biomolecular networks belong to this class of systems and their rheological study can give important information about key structural properties of cells and biological tissues [114,115]. Even if it is well-known that the shear thinning behavior of transient networks is related to the strength of the bonds and their internal connectivity, a complete quantitative interpretation is challenging and still missing. This difficult interpretation is due to the inherent complexity of the transient networks, whose microscopic topology, bond lifetimes and interaction energies are usually known only as statistical distributions [116–118]. In this framework, a quantitative study of the shear thinning viscosity of transient networks and its relation to the microscopic network properties could be performed thanks to a model system characterized by a well-defined microscopic topology and mesh size together with a well-known bond strength and density of bonds. In this way it would be possible to clarify the microscopic mechanisms related to the emergence of non-Newtonian viscosity. This section will describe the transition from Newtonian to non-Newtonian regime of a model DNA-based hydrogel, which gives a quantitative interpretation of the shear thinning behavior in transient networks. This DNA hydrogel is composed by a dispersion of DNA nanoparticles that are independent at high temperature, while they interact and bind to create a transient network upon cooling. As it will be described in the next paragraph, the nanoparticles have the shape of 3-arms nano-stars (NS), and each arm terminates with a 6-base-long overhang that represents a sticky spot for mutual interaction and binding [119]. The nanoparticles connectivity and therefore the network creation are related to the strong temperature (T) dependence of the pairing of the overhangs, which can be precisely predicted on the basis of the well-studied thermodynamics of DNA hybridization [120]. As it will be shown, the system transforms continuously and in a reversible way from a dispersion of independent NS to a percolating transient network upon cooling. The non-Newtonian viscosity of this transient network results from the activation of simple, single-class molecular binding events. The complete control of the network structure parameters – including the number of NS arms (coordination number $f = 3$), the bond lifetime (τ_B) and the binding free energy ΔG – allows quantitatively explaining the transition from linear to shear thinning viscosity in terms of the stabilization of the DNA network.

3.4.1 DNA hydrogel

The preparation of the DNA hydrogel was performed by the *Complex Fluids and Molecular Biophysics group* (at the *Department of Medical Biotechnology and Translational Medicine* of the *University of Milan*) headed by Dr. Bellini, who collaborated with my group in this work, both for the sample preparation and the results interpretation. The DNA NS dispersion is obtained by annealing equimolar solutions of three 48-base-long oligomers:

S1: 5'-p CTACTAAGCGTGGGCGTAAAAACGGTAACCGTTGCGTCATCC **CGATCG**-3'

S2: 5'-p GGATGACGCAACGGTTACCGAACTCAAGAAGGTATTTATAGC **CGATCG**-3'

S3: 5'-p GCTATAAATACCTTCTTGAGAATTTACGCCCACGCTTAGTAG **CGATCG**-3'

These three sequences (S1, S2, S3) self-assemble into three-arms NS. Each arm of the NS is constituted by 20-base-pairs-long duplexes terminating with a 6-base-long overhang. In particular, each oligomer binds to the two others in 20-base-pairs-long sections, with the complementary sections highlighted by colored letters in the sequences above. The sequences hybridization results in the 3-arms nanostructure, in which each arm terminates with a 6-base-long auto-complementary sequence (**CGATCG** in the above sequences), as it can be seen in Figure 3.10 a). The DNA oligomers were synthesized by NOXXON Pharma. The DNA was hydrated using NaCl electrolyte solutions in order to yield a total ionic strength of about 20 mM. The NS annealing was done by slowly cooling the sample from 90 °C to room temperature (at a rate of about 0.3 °C/min). It is possible to determine the fraction of resulting NS via gel electrophoresis, as presented in a previous work from the Complex Fluids and Molecular Biophysics group [119]. Solutions in which more than 86% of DNA is aggregated in NS were obtained.

The DNA NS are independent and stable for $40\ °C < T < 60\ °C$, while at lower T the overhangs of different NS hybridize, and the result is that the NS behave as interacting nanoparticles which attract each other with a valence equal to 3 [119]. A DNA NS concentration of 10 mg/mL was considered in this thesis. For this concentration, the DNA NS dispersion progressively and reversibly transforms from a dispersion of independent NS (at high T) into an arrested hydrogel (at low T) without undergoing to any phase separation [121]. This temperature-controlled gelation is an example of an equilibrium gelation, as the network creation is realized by going through different equilibrium states with no discontinuity [121]. Figure 3.10 b) and c) show an example of the T dependence of the DNA NS network formation: by decreasing the T from 35 °C to 20 °C, the fraction of bound terminals p increases, resulting in the system transformation from a solution of dispersed NS or small clusters to a percolating transient network of bound DNA NS.

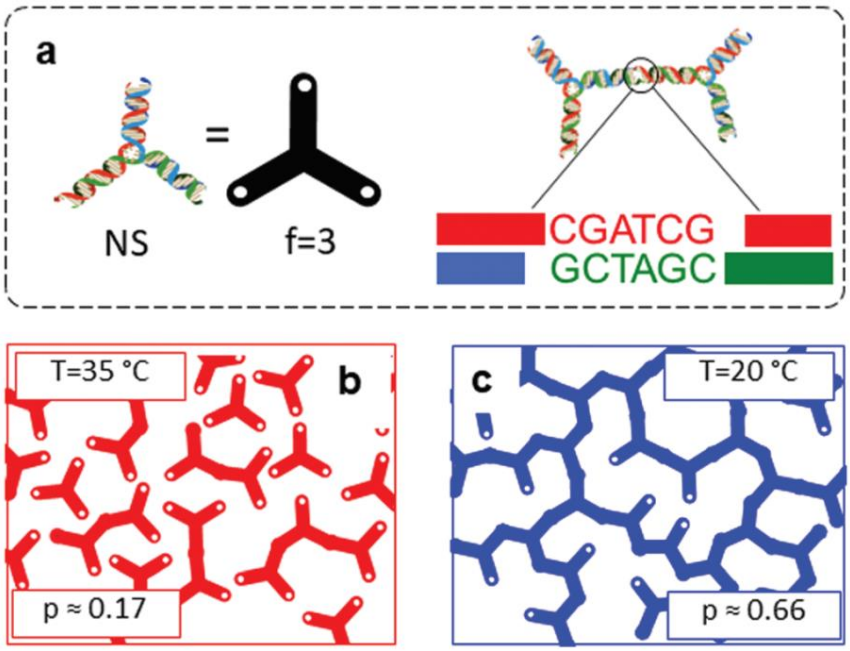

Figure 3.10: Graphical representation of the transient network based on interacting DNA NS [103]. *a) Each DNA nanoparticle has the shape of a 3-arms NS, in which each arm ends with a sticky terminal that provides mutual attraction between the NS so that they can be thought as particles with valence equal to 3* $(f = 3)$. *The sticky spots consist of 6-base-long auto-complementary oligomers (**CGATCG**) that at low temperature hybridize with the overhangs of other NS. b) and c) Pictorial representations showing the temperature dependence of the DNA network creation. The fraction of bound terminals* p *increases going from a temperature of 35 °C to 20 °C, meaning that the system transforms from a solution of dispersed NS or small clusters to a percolating transient network of bound NS.*

3.4.2 Newtonian to non-Newtonian crossover

Optical shooting experiments have been carried out on the DNA hydrogel to investigate the viscous behavior of this material across its liquid-gel transition. The optical shooting experiment represents a stress-controlled microrheological technique that is particularly suited to measure the force-speed ratio and thus to precisely detect the appearance of non-Newtonian behavior. The measurements were carried out by filling the microfluidic channel with a solution of 1 µL of NS dispersed on 20 mM NaCl aqueous solution at a DNA concentration of 10 mg/mL, which corresponds to a NS molarity of 222 µM. A small amount of 5 µm radius PMMA microbeads were dispersed in the DNA solution and used as tracers. A sufficiently long time is waited between two consecutive microbead shootings in order to let the system equilibrate. This condition was verified by checking the dependence of the microbead position $x(t)$ only on T and optical power P_{chip} and not on the repetition rate of the optical shootings. In particular, attention has been paid to perform every shooting experiment in an unperturbed NS dispersion. Optical shooting

measurements have been carried out at different T in the range 20-40 °C and at various optical power P_{chip} (corresponding to optical forces in the range 1-100 pN). Some examples of the acquired microbead trajectories are shown in Figure 3.11 a) (empty dots), in which each curve corresponds to a single optical shooting. As the microbead inertia can be neglected due to the small Reynolds number, the apparent viscosity η_A of the DNA hydrogel can be found from $x(t)$ and $F_s(x, I_L)$ using the Stokes law:

$$\eta_A = \frac{F_s(x, I_L)}{6\pi R v(x)} \tag{3.8}$$

where $v(x)$ is the microbead velocity, which is derived from $x(t)$. Figure 3.11 b) shows η_A as a function of the microbead speed for different T.

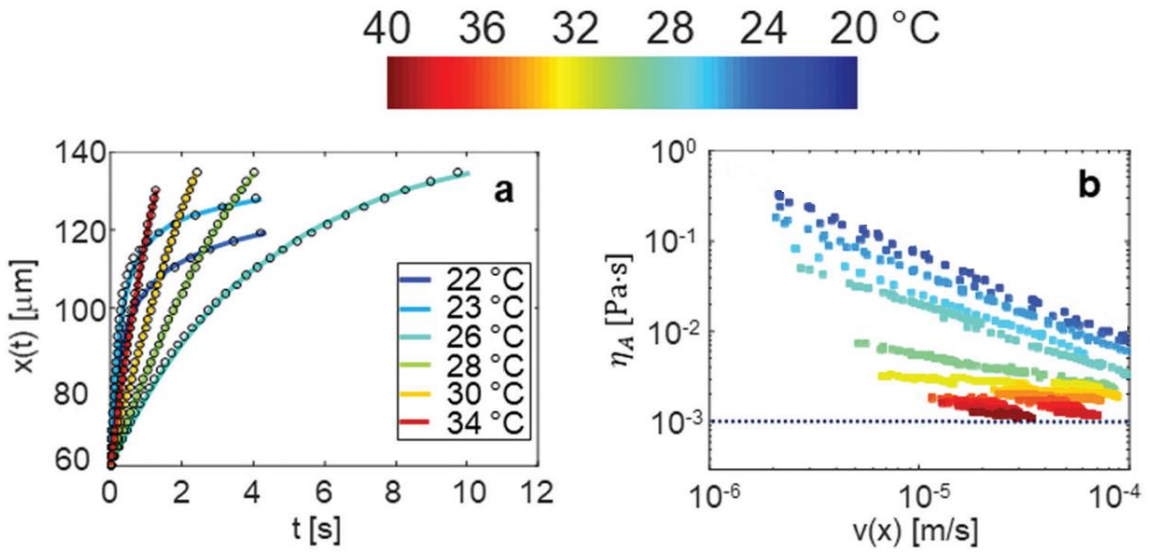

Figure 3.11: Rheological characterization of the DNA hydrogel [103]*. Viscosity measurements have been carried out in a T range represented by the color bar adopted for all the figures. a) Experimentally measured microbead trajectories $x(t)$ for certain T and optical powers (empty dots) and their fitting with the adopted Cross model for the apparent viscosity (lines). b) For each shooting experiment, the microbead velocity $v(x)$ was derived from $x(t)$ and used to determine the apparent viscosity η_A as a function of v (colored points). The dotted line stands for the water viscosity, reported for reference.*

It can be noticed that at the largest T, two different data sets at the same T and at different optical powers were acquired in order to explore a larger force range (and so a larger microbead velocity range). As it can be seen, the viscosity of the DNA solution is Newtonian at high T (red dots) as η_A does not depend on $v(x)$. As T decreases, two different phenomena occur. The first observation is that η_A significantly increases as its value at the lowest microbead velocity grows of almost three orders of magnitude. Secondly, the DNA

solution becomes non-Newtonian and, in particular, η_A shows a marked shear-thinning behavior. In the measured range of velocities, the apparent viscosity shows a power-law behavior that can be described as $\eta_A \propto v^{n-1}$ and thus the force will be of the form $F \propto v^n$, as it can be seen in Figure 3.12, which shows the force-velocity data on a log-log plot. The exponent n, called flow behavior index, goes from 1 (at the largest T, Newtonian limit) to almost 0, as it can be seen by observing the force-velocity data at the lowest T. In particular, the results observed at the lowest T describe the strongest form of shear-thinning viscosity, in which the viscous friction does not depend anymore on the velocity, as it can be appreciated in Figure 3.12.

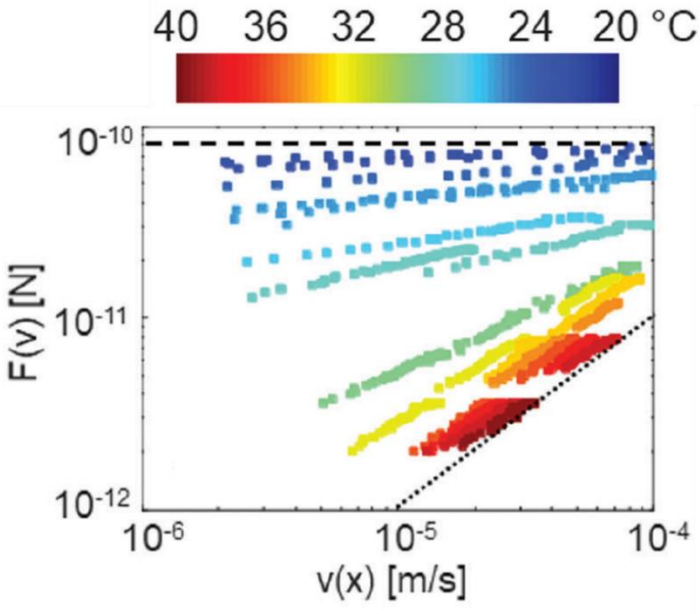

Figure 3.12: Force vs velocity curves from the DNA NS solution measurements acquired at different T, as shown by the color bar [103]*. Dotted line: force-velocity curve in pure water; dashed line: force-velocity curve corresponding to a flow behavior index $n = 0$.*

It must be pointed out that in optical shooting-based experiments a distribution of shear rates is simultaneously probed, differently from conventional cone-plate geometry rheometers, for which the shear rate is uniquely set. In our microrheological experiments, the shear rate distribution is given by the velocity profile of the fluid $v(r, \theta)$ around the microbead, in which r is the distance from the microbead center ($r > R$) and θ is the angle formed with respect to the velocity direction. In case of Newtonian fluids such as water, $v(r) \propto 1/r$ is the dominant term far from the bead [122] that accounts for the Stokes law. When non-Newtonian shear-thinning power-law fluids are considered, for which the viscous friction force is given by $F_{PL} \propto \dot{\varepsilon}^m$ [123], the expression of the velocity profile around a moving microbead is given by $v(r) \propto 1/r^\alpha$, where $\alpha \cong (2-m)/m > 1$ and the viscous friction force on the microbead becomes $F \propto v^m$ [124]. Therefore, despite the

intrinsic inhomogeneity of the shear rate on the fluid induced by the microbead movement, our experimental data suggest that, in the explored T range, the DNA NS hydrogel behaves as a power law fluid, whose exponent is equal to the one controlling the viscous friction force acting on the microbead, i.e. $m = n$.

As discussed in Section 2.2.2, power-law fluid model can be adopted to describe the non-Newtonian shear thinning behavior of fluids, and this approach is usually verified in a limited parameters range. In general, when the shear rate is small enough, every fluid shows a Newtonian behavior. In this condition, the equilibration time of the system, set in our DNA solution by the bond lifetime τ_B, is lower than the characteristic time of the externally imposed stress. The onset of the shear-thinning behavior occurs when the dimensionless product $\dot{\varepsilon}\tau_B$ becomes of the order of unity [125,126], which represents a condition in which the strain rate is sufficiently large to impose a significant tension in the network before it spontaneously opens for the finite lifetime. As in our experiments the shear rate is inhomogeneous, the natural dimensionless parameter to consider for evaluating the onset of the non-Newtonian behavior is $B = v\tau_B/R$ [127], which represents the Deborah number of our measurements. The values of B for the measured DNA NS solution cover four orders of magnitude, as a combination of the small range of experimentally measured microbead velocities and of the significant variation of the bond lifetime that can be obtained as a function of T, as it will be reported in the next figures.

In order to describe the transition from Newtonian to non-Newtonian viscosity in our DNS NS solution, it is possible to adopt the Cross model with exponent equal to 1 [126,128], according to which the apparent viscosity is given by:

$$\eta_A = \frac{\eta_0 - \eta_\infty}{1 + B} + \eta_\infty \tag{3.9}$$

where η_0 and η_∞ are the viscosities in the limit of zero and infinite velocity, respectively. The Cross model describes the transition from a regime of small structural deformations (i.e. high T, small τ_B, small v) in which the system can be described as a Newtonian fluid, to a regime of large structural deformations (i.e. low T, large τ_B, large v) where $\eta_A \propto 1/B \propto v^{-1}$, which coincides with the strong non-Newtonian behavior that is possible to observe in our measurements for the lowest T. The smooth transition between these two different regimes can be interpreted as a family of power-law fluids, each valid in a limited range of B and whose flow behavior index n varies with B as $n \approx (1 + B)^{-1}$. The expression of the apparent viscosity described by the Cross model can be exploited to fit the experimentally measured $x(t)$ (see Figure 3.11 a)) by integrating the equation of the microbead motion with η_∞ set equal to the viscosity of water and with η_0 and τ as fitting variables. It must be pointed out that the data analysis and fitting procedure presented in

Section 3.2.3 cannot be simply extended to shear-thinning fluids, as in this case the apparent viscosity changes with the microbead velocity. Anyway, it is possible to substitute the viscosity η in Equation 3.5 with an apparent viscosity η_A, for which the Cross model has been adopted. By performing this substitution, a quadratic equation of the form $av^2 + bv + c = 0$ is obtained, whose coefficients are given by:

$$a = \frac{\eta_\infty \tau}{R}; \quad b = \eta_0 - \frac{AI_L f(x)\tau}{6\pi R^2}; \quad c = -\frac{AI_L f(x)}{6\pi R} \tag{3.10}$$

As previously explained, it is possible to separate the variables and define a functional T:

$$T(x^*, t^*, x_i, t_i, \eta_0, \tau) = \int_{t_i}^{t^*<t_f} dt - \int_{x_i}^{x^*<x_f} \frac{2a}{-b + \sqrt{b^2 - 4ac}} dx \tag{3.11}$$

The best fit of the experimental microbead trajectories is accomplished by minimizing the functional T with respect to the two parameters η_0 and τ. The results of the fit can be seen in Figure 3.11 a) (colored lines) and the good fit accuracy suggests that all the measured data can be expressed in terms of two dimensionless parameters $(\eta_A - \eta_\infty)/(\eta_0 - \eta_\infty)$ and B, which can be calculated from $\eta_0(T)$ and $\tau(T)$ resulting from the fit of each optical shooting. In particular, by rescaling the $\eta_A(v)$ datasets (see Figure 3.11 b)) using these two dimensionless parameters, they collapse on a universal curve, shown in Figure 3.13. This collapse validates the idea that the entire behavior of the DNA hydrogel can be explained as a single basic microscopic mechanism with the power-law behavior emerging as a cross-over condition. This microscopic mechanism can be even appreciated by observing the T dependence of the best fit results of η_0 (red triangles, right-hand axis) and τ (blue diamonds, left-hand axis), shown in Figure 3.14 as a function of T^{-1}. In Figure 3.14 it is shown even τ_{DLS} (green squares, left-hand axis), which is the lifetime of thermally induced concentration fluctuations that was previously measured by the Complex Fluids and Molecular Biophysics group by means of Dynamic Light Scattering (DLS) measurements on the same DNA NS solution [119,121,129].

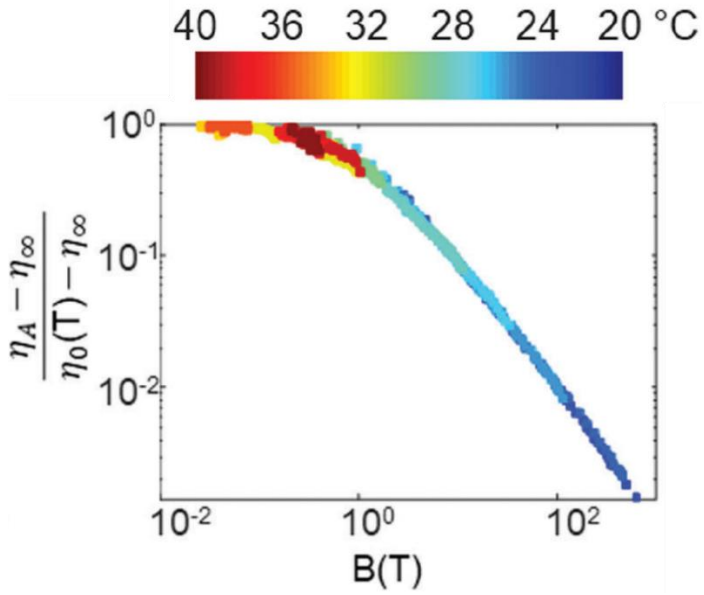

Figure 3.13: The $\eta_A(v)$ datasets are rescaled using two dimensionless parameters based on $\eta_0(T)$ and $\tau(T)$. This scaling of the apparent viscosity results in the collapse of all measured data on a universal curve [103].

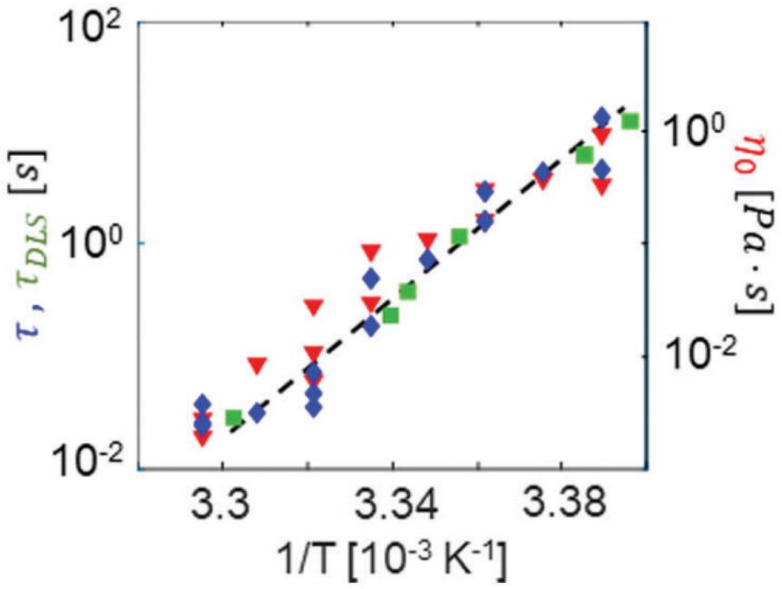

Figure 3.14: The fit of the experimental bead trajectories with the Cross model for the apparent viscosity enabled estimating the values of the viscous characteristic time $\tau(T)$ (blue diamonds, left-hand axis) and the zero-shear viscosity $\eta_0(T)$ (red triangles, right-hand axis) for each optical shooting [103]. *The values of $\tau_{DLS}(T)$ (green squares, left-hand axis) were previously measured via Dynamic Light Scattering experiments by the Complex Fluids and Molecular Biophysics group.*

The results reported in Figure 3.14 suggest that the whole viscous and thermal behavior of the DNA NS solution is determined by a single Arrhenius process. It is possible to determine the associated activation enthalpy ΔH from the slope of the data, represented by the black

dashed line. The measured data give a value of $\Delta H \approx 87\ kcal\ mol^{-1}$, which is compatible with the enthalpy required to break the bonds between the NS [119,121,129]. Moreover, both the T dependence and the absolute values of the viscous characteristic time τ (blue diamonds, left-hand axis of Figure 3.14) are in agreement with the expected inter-NS bond lifetime τ_B (characteristic time of the microscopic bonds), previously estimated from hybridization kinetic studies [130]. In addition to that, η_0, the viscosity in the limit of zero speed, shows the same growing behavior as the characteristic times, according to an equal activation scaling. This characteristic agrees with the theory of network-forming molecular glasses such as silica [131], and it is reasonable because the characteristic energy scale in this system is set by the inter-NS bond enthalpy.

3.4.3 Three regimes and final remarks

The collapse of the optical shooting datasets into a single universal curve that depends on our Deborah number B suggests that the entire DNA system behavior is related to the interplay between the shear stress, which is imposed by the microbead motion in the surrounding network, and the relaxation time of the network itself. According to this observation, it is possible to qualitatively describe the behavior of the DNA network and its dependence on T as the evolution through three different regimes: the "cluster regime" (Newtonian), the "stretched elastic network regime" (Newtonian) and the "network fracturing regime" (non-Newtonian), which are pictorially represented in Figure 3.15. As previously discussed, at high T the NS bond lifetime is short and the NS are independent or aggregated in small clusters. We labelled this phase as "cluster regime", in which the viscosity is similar to the viscosity of water (η_w, black dotted lines in Figure 3.11 b) and in Figure 3.12), increased by a correction factor proportional to the effective volume fraction of suspended NS and NS clusters [132]. Therefore, in this regime, the DNA NS solution basically behaves as a Newtonian fluid similarly to water (Figure 3.15 a1 and a2). As T decreases, a network begins to form and the NS clusters become extended enough to be significantly deformed by the local shear rate resulting from the microbead motion (Figure 3.15 b1 and b2). Due to the imposed deformation, the DNA NS network generates a shear elastic force which is opposite to the microbead movement. However, in this phase that we called "stretched elastic network regime" (Newtonian), the NS bond lifetime is short enough such that the bonds are not directly broken by the microbead during its motion, as they open spontaneously fast enough before reaching their tearing point. By further decreasing the T, the network is long-lived and percolating and in this situation the microbead can move only by breaking the bonds, suggesting the name "network fracturing regime" (Figure 3.15 c1 and c2). In this regime, the work that is spent for the microbead motion must equal the energy required to break the inter-NS bonds opposing the bead movement. Therefore, the frictional force experienced by the microbead during its motion

just depends on the number of broken NS bonds and not on the bead speed, a condition that reflects the strong shear-thinning behavior of the material experimentally measured at the lowest T (see Figure 3.12).

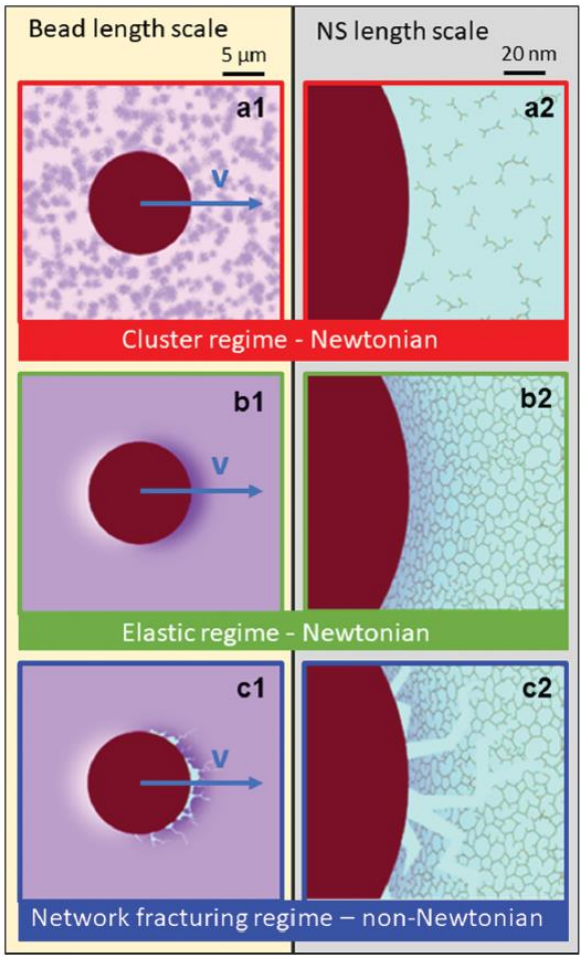

Figure 3.15: Graphical representation of the three different regimes in the transition from Newtonian to non-Newtonian viscosity of the DNA hydrogel [103]. *By decreasing the temperature of the system, the DNA NS solution passes through different regimes, here pictorially represented at the microbead length scale (left-hand side) and at the NS length scale (right-hand side). In the left panel the NS density is represented by purple shading. In the first state, that we called "cluster regime", the system is a dispersion of independent NS or small clusters of NS and it behaves as a Newtonian fluid (a1 and a2). In the second phase, the Newtonian "stretched elastic network regime", a NS network is created, but the NS bond lifetime is short enough such that the DNA network is stressed by the microbead motion, but the bonds are not broken by the microbead as they open spontaneously (b1 and b2). In the third state, the "network fracturing regime", the network is long lived and the NS bond lifetime is long so that the microbead can move in the network only by breaking the NS bonds to create an opening to pass through the network (c1 and c2). This results in a strong non-Newtonian response of the material.*

In conclusion, the model DNA NS hydrogel here-studied by an optical shooting-based active microrheological technique allowed investigating the complex viscous behavior of network forming systems. The most important finding of this study is the experimental observation that the transition from Newtonian to non-Newtonian behavior (strong shear-thinning viscosity) of this model transient network occurs through a continuous set of power-law fluid regimes, covering all the possible shear-thinning flow behavior indices (from 1 to 0 upon lowering the T). In particular, the Newtonian to non-Newtonian crossover going from the "stretched elastic network regime" to the "network fracturing regime" takes place in a really small T range. More specifically, the exponents of these power-law fluids describing the transition vary from $n \approx 0.8$ to $n \approx 0.2$ in a T range of 2-3 °C width around 26 °C. For the lowest T experimentally measured we found a region in which the viscous friction is independent on velocity, i.e. $n \approx 0$ and therefore $\eta_A \propto v^{-1}$.

A key point for this study was the strong T dependence of the NS bond lifetime, by which it has been possible to explore four decades of Deborah number B with a moderate range of shear rates (microbeads velocities) and in a small T range. A last observation is that the here-studied DNA NS hydrogel, which was proposed as a model of strong glass formers for its thermodynamic and equilibrium properties [121], has rheological properties similar to silica, which is considered the archetype of glass forming liquids. Specifically, the collapse of $\eta_A(v)$ once properly rescaled and the proportionality between the viscosity in the limit of zero speed and the relaxation time are characteristics that resemble the rheological behavior of silica.

3.5 Creep tests of yield stress fluids

The last part of this chapter is dedicated to the measurement of a particular class of viscoelastic materials named *yield stress fluids* (even called *viscoplastic fluids*). These materials are characterized by a certain threshold: for values of the applied stress lower than this threshold they behave as elastic solids, whereas for stresses larger than this threshold they flow as liquids [133,134]. However, for values of the imposed stress closer to this critical value the situation is still not clear. Other open questions concerning the response of these materials are related to the dependence of the yield tress threshold on the material microstructure and stress distribution in the material [135]. Examples of yield stress fluids are everyday life products such as toothpaste and cement. More complex systems showing a yield stress behavior are biological and synthetic fibers and biological samples such as blood. The rheological investigation of biological samples and materials which are available only in a limited quantity can really benefit from a microrheological approach, as already pointed out in this thesis. However, surprisingly few microrheological studies have been carried out on yield stress materials [136,137]. The main obstacle for the

investigation of these materials is given by the high stresses required to probe the material response in the different regimes, going from the elastic to the viscous one. In the next paragraphs it will be shown how the optical shooting technique proposed in this thesis can be successfully employed for probing the mechanical response of yield stress fluids in different rheological regimes. A theoretical introduction to yield stress fluids will be initially given in the next section. The chapter will end with the description of the measurement procedure and obtained results.

3.5.1 Yield stress fluids

The peculiar feature of a viscoplastic fluid is that it is characterized by a certain yield stress: the material is able to flow (i.e. deform indefinitely) like a fluid if it is subjected to a stress value larger than its critical threshold, whereas it deforms in a finite way like an elastic solid if the material is not sufficiently stressed. The rheological properties of viscoplastic fluids are difficult to predict as their study involves the rising of transient or permanent solid and liquid regions, whose location in the material structure is difficult to be a-priori determined. A further complication arises when viscoplastic fluids whose rheological properties depend on the flow history are considered. For these materials, which are labelled with the term *thixotropic*, the viscosity depends not only on the shear rate but even on the history of the sample, the aging, the aggregation of various microstructures and their rearrangement due to the sample flow and deformation.

In order to quantify the steady-state flow characteristics of a non-Newtonian fluid the measurement of its complete flow curve is required, as the fluid viscosity depends on the applied stress [135]. As explained in Section 2.4, the flow curve gives the relation between the shear stress σ and the shear rate $\dot{\varepsilon}$. In case a Newtonian fluid is considered, these two quantities are linearly related, i.e. $\sigma = \eta\dot{\varepsilon}$, where η is the viscosity, which is independent on the applied stress. For a viscoplastic fluid, the viscosity strongly depends on the shear rate, $\sigma = \eta(\dot{\varepsilon})\dot{\varepsilon}$, and the flow curve is no more a straight line crossing the origin, as in the case of Newtonian fluids. Different models have been proposed for describing the stress-shear rate relationship for a viscoplastic fluid and the existence of a yield stress value separating the elastic and viscous behavior. The simplest idealization of a viscoplastic fluid, but nevertheless one of the most known and used for its simplicity, is the Bingham model [135]:

$$\begin{aligned} \sigma < \sigma_y&: \ \ \dot{\varepsilon} = 0 \\ \sigma \geq \sigma_y&: \ \ \sigma = \sigma_y + \eta_P\dot{\varepsilon} \end{aligned} \tag{3.12}$$

where $\sigma_y > 0$ is the value of the yield stress and the parameter η_P accounts for the slope of the flow curve in the fluid region, that is defined by $\dot{\varepsilon} > 0$. An equivalent formalization of the Bingham model is given by an effective viscosity, which is asymptotically equal to η_P for large values of the applied stress and it diverges continuously as the stress decreases and approaches the yield stress: $\eta_{eff}(\dot{\varepsilon}) \equiv \sigma/\dot{\varepsilon} = \eta_P + \sigma_y/\dot{\varepsilon}$. The simplicity of this model lies in the fact that it employs only one material-dependent number, the value of the yield stress σ_y, to describe the complex, nonlinear behavior of viscoplastic fluids. A popular generalization of the Bingham model in the shear flow regime is the Herschel-Bulkley equation, which is given by [135]:

$$\sigma \geq \sigma_y: \quad \sigma = \sigma_y + K\dot{\varepsilon}^n \tag{3.13}$$

where K and n are two parameters which can be considered as the flow consistency index and flow behavior index, previously introduced in the description of non-Newtonian fluids. It can be noted that the Bingham model is a specific case of the Herschel-Bulkley equation, which is obtained by considering $n = 1$. The Herschel-Bulkley model describes both the yield stress regime $\sigma \approx \sigma_y$ for low values of the shear rate, and a power-law shear thinning regime $\sigma \approx K\dot{\varepsilon}^n$ for large values of the shear rate, with $0 \leq n \leq 1$.

Different experiments can be macroscopically performed by using a standard rheometer in order to distinguish between the solid and liquid regimes and determine the value of the yield stress. These tests include, for example, creep experiments, flow-curve measurements and amplitude sweep tests. It must be pointed out that different tests often give as a result non negligible differences in the value of the estimated yield stress, underlying again the difficulty in the rheological characterization of these materials. The creep test will be here explained as its microrheological implementation, based on the optical shooting technique, will be presented in the next sections. The creep tests performed with a conventional rheometer consist in recording the material deformation (strain ε) as a function of time for a constant applied stress σ, for different stress values. An example of creep tests performed on a hair gel is reported in Figure 3.16 [138]. As it can be seen, after an initial transient phase the different strain-time curves evolve according to two different behaviors. For values of the stress larger than a critical value (here around 62 Pa), the curves significantly increase with time following a line with slope 1 on the log-log scale, which indicates that the viscoplastic fluid flows at a constant shear rate [134,138]. This situation corresponds to the *liquid regime* of the yield stress fluid. Instead, for values of the stress lower than this critical value, the strain tends to a plateau, as in the case of an elastic solid. However, differently from a purely elastic solid, in this second regime the strain keeps increasing with time, suggesting a really slow flow. Anyway, it can be noted that the slope decrease in time suggests that the apparent shear rate would continuously

decrease toward values even lower without arriving to a situation corresponding to a steady state flow. This apparently limited strain and the continuous decrease of the apparent shear rate with time justify the fact that we can label this regime as a *solid regime*. However, it must be underlined that for values of the stress close to this critical threshold the situation is still unclear: the strain can reach significant values, but the shear rate continuously decreases with time (slope less and less than 1 on the log-log scale). Therefore, this remarks once again that an exact determination of the value of the yield stress is challenging: ideally, the definition of the yield stress is the stress value which implies a steady flow at a shear rate infinitely small, which would require an infinite time to be reached due to the finite material deformation associated to the solid-liquid transition [138].

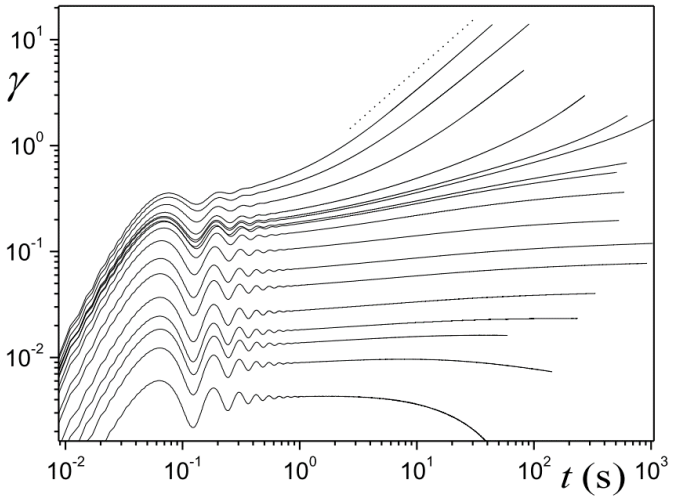

Figure 3.16: Typical behavior of the strain (here indicated with the letter γ)-time curves measured for different stress values (increasing from bottom to top) applied to a hair gel. The stress values are: 0.8, 4, 6, 8, 12, 20, 28, 40, 50, 56, 60, 63.2, 66.8, 70, 80, 90, 100 Pa. The dotted line indicates the curve with slope 1 on the log-log plot [138]. *The data are taken from* [139].

Yield stress fluids present some features which strongly differentiate them with respect to common solid materials. A solid behavior is commonly related to a given material structure, and a solid object breaks or flows in relation to the fact that it is brittle or ductile, respectively, but, in any case, it loses its initial mechanical properties once a critical deformation (beyond the breakage of the initial structure) is reached. Instead, yield stress fluids present different peculiar features: (i) these materials show a solid structure at rest, which may be thought as the structure of a usual solid; (ii) beyond a critical stress, this structure breaks and the material flows as a liquid; (iii) leaving again the material at rest for a sufficient time makes it recover its initial mechanical (solid) properties, with a structure similar to the initial one [138]. These materials are therefore able to change from a solid to

a liquid state, and vice versa, in a reversible way. These properties are the result of the soft interactions between the elements composing the fluid, which can build a jammed structure which resembles the properties of a solid, but the structure itself can also be easily broken if a sufficiently large stress is applied. Examples of materials showing this kind of behavior are foams, gels and emulsions.

3.5.2 Measurement protocol

The previously described optical shooting microrheological setup was employed to characterize some well-known yield stress fluids in order to show the performance of the integrated microrheometer. The measurements performed on these viscoplastic fluids will be compared to creep measurements of a conventional rheometer. As the measured samples show a non-significant change of their rheological properties over the temperatures measurable with our setup, all the experiments were carried out at room temperature, without the actuation of the temperature controller circuit. Some considerations related to the solid behavior at rest of viscoplastic fluids must be pointed out. Due to the material stiffness and rigid structure, the acoustic force cannot be exploited to perform the microbeads acoustophoretic prefocusing as this kind of force is not strong enough to move a microbead in these solid-like materials. Therefore, even the function generator previously used to drive the piezoceramic element is not actuated during these measurements. As significantly high optical forces are required to stress these materials, 5 μm radius polystyrene microbeads (Sigma Aldrich 72986, $n = 1.57$ at 1070 nm) were used as tracers, as they have a higher refractive index with respect to PMMA microbeads ($n = 1.48$ at 1070 nm). In this way, for the same optical power, it is possible to achieve higher scattering forces on the microbead. Although the acoustic force cannot be exploited for the acoustophoretic prefocusing, the intrinsic stiffness of yield stress fluids helps us in finding and shooting a single microbead. Under certain conditions, which are related to the yield stress value of the material, to its density and to the density and radius of the tracer, the material structure is stiff enough to counteract the weight force of a dispersed microbead [140]. Therefore, in this situation, the microbeads remain stuck and do not move toward the channel bottom due to gravity. Some numerical studies have been performed to determine the conditions for which a particle moves in a viscoplastic fluid simply due to the weight force [140]. Without entering into details, in our specific situation polystyrene microbeads remain stuck in the material network and do not sink due to gravity, as even experimentally observed. This implies that, by dispersing a small amount of microbeads in the viscoplastic fluid to be tested and by injecting the prepared sample in the microfluidic channel, the microbeads will be dispersed at different channel heights. Optical shooting experiments can be therefore performed on microbeads positioned around half height of the channel, in correspondence of the optical waveguides which emit

the laser radiation. The gradient force acting on the microbead ensures that the microbead is automatically aligned along the beam axis, where the gradient force reduces to zero and only the scattering component of the force is present. For what concerns the optical shooting experiments, the measurement protocol is different with respect to the one presented in Figure 3.4. The first step consists in finding a microbead suitable for the measurements, i.e. located around half height of the channel. This can be done by simply making the sample flow by actuating the external micropump. Once an appropriate microbead is found, it is not shifted toward the left channel border, as previously shown in Figure 3.4. This is because the here-measured yield stress fluids are significantly stiffer than the materials previously characterized and shifting the microbead position toward the left channel border would require a large force, sometimes even not achievable with the current setup. Moreover, as it will be shown in the next section, the microbead displacement is in the order of few µm or less for each optical shooting experiment, which implies that many measurements can be carried out even without shifting the microbead position toward the left border. Obviously, this is valid just in case the microbead is not too close to the right border. Therefore, the optical shooting experiments can be performed by simply using a single laser beam, let assume the one emitted by the left waveguide, referring again to Figure 3.4. The optical power emitted by the right waveguide is shut down by means of the manually controlled variable attenuator placed in one U-bench. In order to perform the creep and recovery measurements, the force acting on the microbead must be of the form shown in Figure 3.17. The force is initially set to zero in order to retrieve the microbead starting position, then it is increased to a constant value for a certain time and then it is decreased back to zero to estimate the material recovery. During the whole process, the microbead position is recorded by tracking the particle movement as explained in Section 3.1.3. This protocol can be accomplished by initially blocking the power emitted by the left waveguide by means of the LabVIEW-controlled beam blocker placed in the U-bench and setting the laser at the desired emission power. In this way the power emitted by the laser is stable. The microbead position is initially recorded for a time T_1, during which the optical force is equal to zero as the optical beam is blocked. After this initial time, the beam blocker in the U-bench is abruptly removed and hence the microbead will be subjected to a rectangular step optical force, which is maintained for a time duration equal to T_2. Then the optical beam is blocked again and the microbead recovery is recorded for a time duration equal to T_3. The optical force acting on the microbead during time T_2 can be considered almost constant for small microbead displacements, in the order of few µm or less, as the optical force profile of the scattering component slightly varies with the position along the channel width (see for example Figure 3.6 a)). This measurement procedure is highly automatized thanks to a custom LabVIEW program, which allows setting the different time durations.

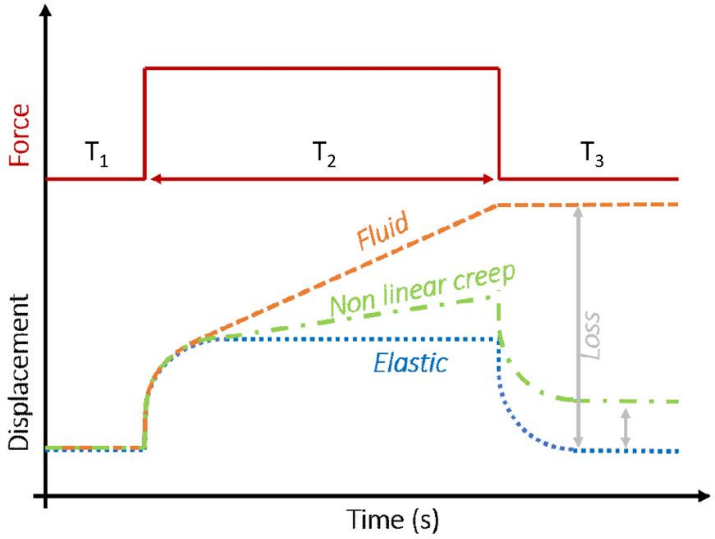

Figure 3.17: Creep and recovery measurement protocol. A step force is applied to the microbead (top panel) and the microbead position is recorded over time (bottom panel). The bead response can follow three different regimes, depending on the value of the applied stress. For an applied stress lower than the yield stress: linear elastic response (blue curve). For an applied stress comparable or slightly larger than the yield stress: nonlinear creep (green curve). For an applied stress significantly larger than the yield stress: fluid regime (orange curve).

The microbead displacement reflects the material response, which can basically follow three distinct behaviors, shown in the bottom panel of Figure 3.17. For stress values lower than the yield stress, the material response is elastic and the microbead displacement will have the same shape of the input force. Once the force is removed, the microbead will completely recover the deformation, coming back to the initial position. This corresponds to the linear *elastic regime*, for which, by doubling the stress value, even the strain will double. For stress values comparable or slightly larger than the yields stress, the material dissipates energy due to an inelastic deformation: the bead displacement does not exactly follow the force step function, but after an initial instantaneous deformation, it keeps increasing with time (*nonlinear creep*). Once the force is removed, the bead displacement is not completely recovered and the difference between the final and initial bead position is related to the energy dissipation. If the applied stress is significantly larger than the yield stress, after an initial instantaneous deformation, the microbead breaks the surrounding region and its position will be a linear function of time with a slope 1 on a log-log scale, as in a viscous fluid (*fluid regime*). When the force is removed, the microbead will not recover its initial position as all the energy is lost due to the viscous friction. It is therefore possible to study the transition between the elastic and fluid regime and estimate the yield stress value by evaluating the change of the strain-time slope as a function of the applied stress. Moreover, it is interesting to estimate the value of the initial instantaneous

deformation as a function of the applied stress, which gives a measure of the storage (or elastic) modulus G' of the material. This is because the elastic component is always in phase with the applied stimulus. The study of G' as a function of the applied stress allows evaluating the transition from the linear to nonlinear regime.

3.5.3 Colloidal fibers preparation

In order to test the performance of the system, the rheological properties of well-studied viscoplastic fluids were investigated. The results of creep and recovery measurements performed using the microrheometer were compared with those obtained by means of a conventional rheometer. The viscoplastic fluids were prepared by the Complex Fluids and Molecular Biophysics group. The same group also performed the macroscopic measurements with the rheometer. The measurements were carried out on a simplified version of a liquid detergent prepared from an aqueous solution of Linear Alkylbenzene Sulphonate (LAS) surfactant, in which a small quantity of fibers composed of Hydrogenated Castor Oil (HCO) is dispersed [141]. At the concentrations commonly used in liquid detergents, LAS is in a worm-like micellar phase, showing a typical Maxwell behavior. The addition of HCO fibers provides solid-like properties and a yield stress behavior to the system, which can be now mechanically modelled by a parallel connection of a Maxwell element and an elastic spring. Specifically, the measured materials are composed of aqueous solutions of LAS neutralized with monoethanolamine (MEA) to pH = 8, and hydrophobic fibers composed of HCO. The HCO fibers were derived by emulsion crystallization of HCO in a solution of LAS at a concentration of [LAS] = 16 wt%. During this process, HCO is emulsified at high temperature and the emulsion is slowly cooled and sheared at the same time. During the cooling process, HCO nucleates within the aqueous surfactant phase and the emulsions droplets operate as a reservoir for HCO in the aqueous phase [142]. It must be noted that the final shape of the HCO-crystallites at the end of this production process strongly depends on the cooling rate and shear rate used. In particular, three main final crystal morphologies have been reported in the scientific literature: irregular crystals, rosettes and fibers [143,144]. The suspensions characterized in this thesis are mainly composed of rigid fibers having diameters of $\sim$ 20 nm and lengths which vary in the range 2-20 μm. The measured samples are produced following two different production protocols for the cooling rate and shear rate used, which have an impact on the length of the resulting fibers and hence on the rheological properties of the final systems. We can identify the two methods referring to the resulting fibers with the term *long* and *short*. The density of HCO fibers approximately matches the density of the LAS surfactant phase, so that gravity effects can be neglected. Samples with LAS concentrations of 5.8 wt% and 10 wt% and HCO concentration of 0.4 wt% were prepared by dilution from a stock

solution containing [HCO] = 4 wt% and [LAS] = 16 wt%. Two different samples were measured:

- long fibers with HCO concentration of 0.4 wt% and LAS concentration of 5.8 wt%, which will be indicated in the following as long fibers 0.4 wt% (HCO) 5.8 wt% (LAS);
- short fibers with HCO concentration of 0.4 wt% and LAS concentration of 10 wt%, which in the following will be indicated as short fibers 0.4 wt% (HCO) 10 wt% (LAS).

3.5.4 Measurements of colloidal fibers

The first measurements were performed on the long fibers 0.4 wt% (HCO) 5.8 wt% (LAS) sample by carrying out creep and recovery experiments at different laser powers with our active microrheological setup. These measurements were compared with creep measurements performed with a conventional rheometer (Anton Paar MCR 302 with cone-plate geometry) by the Complex Fluids and Molecular Biophysics group. The experiments with the rheometer were carried out at different stress levels, as shown in Figure 3.18. In these measurements, the stress is set to a certain value (indicated by the color bar) and it is maintained for all the experiment duration. The strain resulting from the applied stress is recorded as a function of time for all the measurement duration. As it can be seen, by increasing the value of the stress (from blue lines to red lines), the system shows a transition from the elastic regime (constant strain or a slow strain increase as a function of time, after an initial transient phase) to the fluid regime (the strain as a function of time follows a line with slope 1 on the log-log plot).

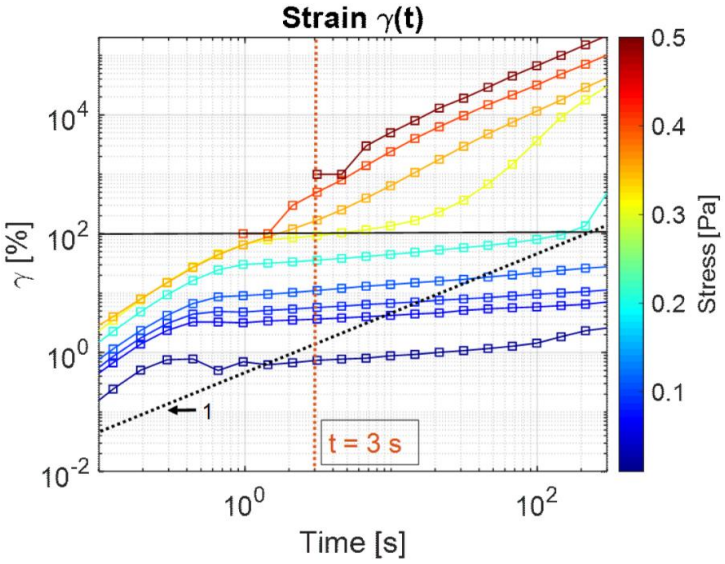

Figure 3.18: Creep measurements performed on the long fibers 0.4 wt% (HCO) 5.8 wt% (LAS) sample with a conventional rotational rheometer. Creep experiments were carried out at different stress values, as indicated by the color bar on the right. The dashed black line represents a line with slope 1 on the log-log graph.

As it was previously anticipated, the exact determination of the yield stress value is not easy, as it appears evident by observing the reported curves. As a first comment, the strain-time curves clearly follow a line with slope 1, after an initial transient phase, for an imposed stress value of 0.35 Pa (orange curve) and larger values (red curves). Therefore, one could say that the yield stress of this material is around 0.35 Pa. However, if we observe the curves behavior for a longer time, even the yellow curve follows a slope 1 after a longer time in which it just shows a nonlinear creep behavior, suggesting that the yield stress value is around 0.3 Pa. This behavior, i.e. the transition to the liquid regime after a nonlinear creep phase, is called *delayed yielding*. As the duration of the creep phase in our microrheological experiments will be set equal to 10 s, we will consider a yield stress value, according to the rheometer measurements, of around 0.35 Pa. The time duration was limited to 10 s in order to limit the heating effects due to the light absorption by the material.

Some of the microbead trajectories acquired from the creep and recovery measurements performed with the integrated microrheometer, as a function of the applied stress (see color bar), are shown in Figure 3.19. In particular, the effective stress σ acting on the microbead is calculated as $\sigma = \langle F_s(x, I_L)\rangle/(12\pi R^2)$, where $\langle F_s(x, I_L)\rangle$ is the value of the scattering component of the optical force averaged over the positions where each optical shooting is performed, for the selected laser current I_L, while R is the microbead radius. The effective area $12\pi R^2$ at the denominator is calculated from the geometric factor $6\pi R$ introduced in Section 2.4 in case of small displacements [101]. It must be noted that this is only an approximation of the strain distribution around the bead.

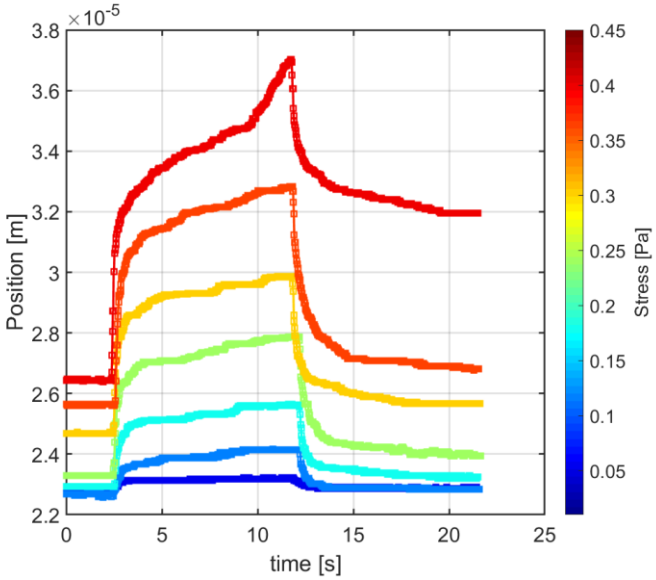

Figure 3.19: Microbead trajectories resulting from the creep and recovery measurements, as a function of the applied stress (see color bar), performed on the long fibers 0.4 wt% (HCO) 5.8 wt% (LAS) sample with the integrated microrheometer.

As it can be seen from Figure 3.19, for each optical shooting experiment, the measurement protocol consists in acquiring the bead initial position for some seconds with no optical force (time T_1), then the optical force is switched on for 10 seconds (time T_2) to perform the creep measurement and finally the optical force is switched off to measure the bead recovery (time T_3). For the bead trajectories at low stress values, the response of the material is in the elastic regime, as it is particularly evident by observing the blue curves. By increasing the optical power, and hence the stress acting on the bead, the nonlinear creep becomes larger and larger and the bead recovery significantly decreases due to a partial energy dissipation. This is particularly evident for the trajectory corresponding to a stress around 0.4 Pa (the red curve), for which the bead recovery is significantly lower with respect to the other trajectories and a significant increase in the slope of the curve can be noticed around 9 s. The same behavior can be better appreciated by observing the percentage strain $\varepsilon(t)$ as a function of time in Figure 3.20 a), which is calculated as $\varepsilon(t) = 100 \cdot (x(t) - x_0)/(2R)$, where $x(t)$ is the bead position as a function of time while x_0 is the initial bead position, before the optical shooting. In order to appreciate the transition from the elastic to liquid regime, it is possible to plot the strain data on a log-log scale, as shown in Figure 3.20 b). It can be observed that the red curve, corresponding to a stress of around 0.4 Pa, assumes a slope 1 at a time equal to around 9 seconds. Therefore, we can say that for this sample the yield stress value estimated with the microrheometer is around 0.4 Pa, which is compatible with the value of 0.35 Pa resulting from the rheometer experiments by assuming the same time scale for the creep measurements (a rectangular step force applied for 10 seconds).

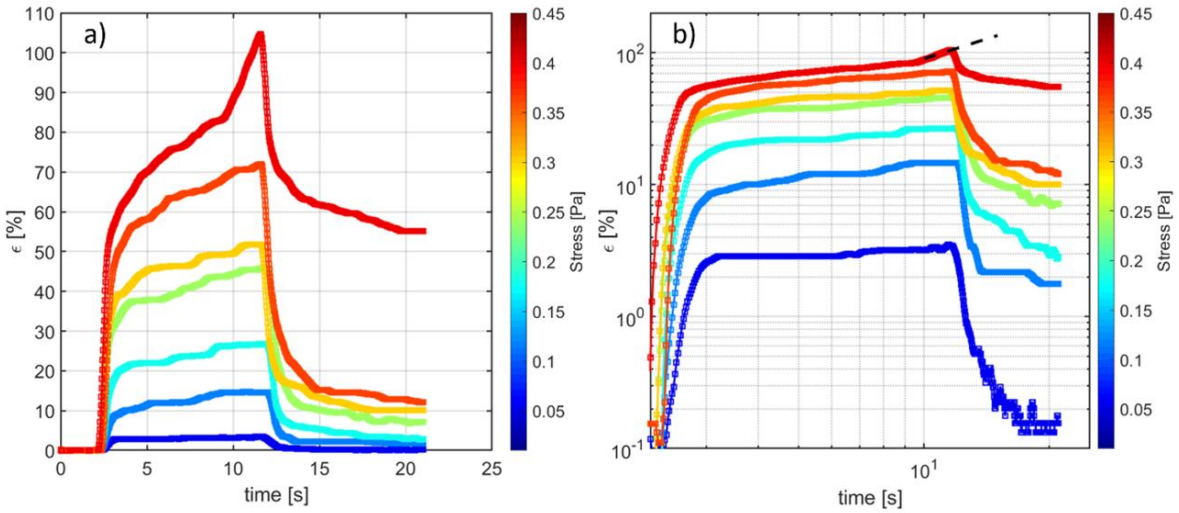

Figure 3.20: Percentage strain curves as a function of time resulting from the creep and recovery measurements, as a function of the applied stress (see color bar), performed on the long fibers 0.4 wt% (HCO) 5.8 wt% (LAS) sample with the integrated microrheometer. The same data are shown in a) a linear scale and in b) a logarithmic scale. The black dashed line in panel b) represents a line with slope 1 on the log-log scale.

It is then possible to quantify the microbead recovery, which is related to the energy stored and dissipated in the material in the linear and nonlinear regime, respectively. By identifying the maximum strain reached during time T_2 as ε_{ON} and the strain recovered during time T_3 as ε_{OFF}, where ON and OFF are related to the laser radiation, it is possible to graphically represent the material recovery by showing the ratio $\varepsilon_{OFF}/\varepsilon_{ON}$ as a function of the maximum strain ε_{ON} (see Figure 3.21). The value of the ratio $\varepsilon_{OFF}/\varepsilon_{ON}$ can vary between 1 and 0: for values closer to 1, the recovery is almost total and the microbead comes back to the original position, whereas smaller values indicate a decrease in the elastic recovery and a transition from the linear elastic regime to a nonlinear regime (creep response and fluid regime). In particular, it is possible to distinguish between the three different regimes theoretically introduced in the previous section. For the blue point, the recovery is larger than 90%, which can be identified with the elastic regime in which the microbead comes back to almost the initial position. For higher levels of stress, the recovery decreases toward 80 %: in this nonlinear regime, after an initial instantaneous deformation, the microbead keeps slowly moving under the effect of the optical force (nonlinear creep), and the result is a significant energy dissipation and a non-complete recovery. For values of the stress larger than 0.4 Pa (red points), the recovery decreases to a value even lower than 30%, suggesting a strong nonlinear response of the material and the beginning of the fluid regime, as confirmed by the slope 1 observed in the strain-time curve in Figure 3.20 b). It is interesting to notice that in our microrheological measurements the strain recovery is never equal to zero in case of material fluidification, as it commonly happens, instead, in the rheometer experiments. We still miss a clear explanation of this behavior and further measurements and analysis must be carried out in order to have a better understanding of this point. We speculate that this feature can be related to the *local nature* of our measurements, intrinsically different with respect to macroscopic measurements performed with a rheometer. Specifically, in a measurement performed with a rotational rheometer, the material breaking and fluidification take place in a large region as all the material is subjected to the applied shear stress. Instead, in an optical shooting experiment, the fluidized region is of the order of the microbead. Once the microbead completely breaks a certain region due to the significantly high stress level, it moves like in a viscous fluid, entering therefore in the liquid regime of the yield stress fluid. Then, after a movement which is of the order of the microbead size, the microbead reaches a new region that needs to be broken again in order to let the microbead pass. Therefore, the region which is subjected to the stress imposed by the microbead is always new and it stores a potential (elastic) energy always different from zero, which is released once the optical force is shut done, resulting in a certain microbead recovery.

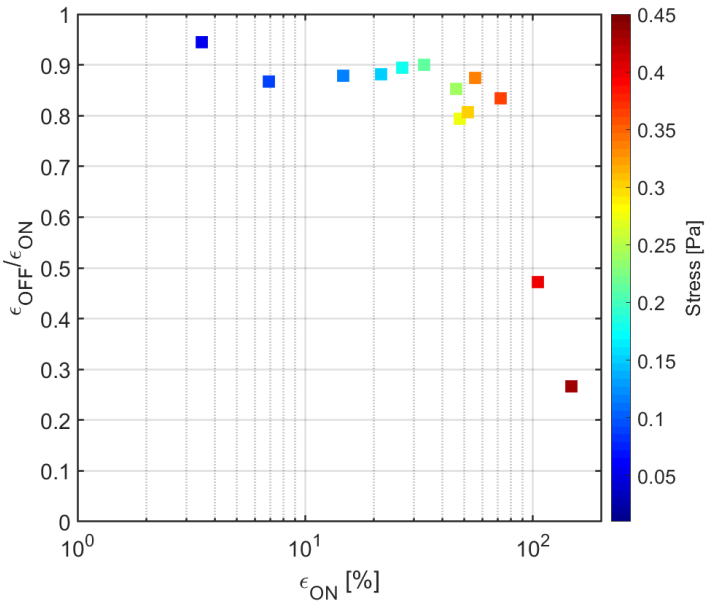

Figure 3.21: Estimation of the microbead recovery resulting from the creep and recovery measurements performed on the long fibers 0.4 wt% (HCO) 5.8 wt% (LAS) sample with the integrated microrheometer. The quantity $\varepsilon_{OFF}/\varepsilon_{ON}$ gives a measure of the microbead recovery: a value equal to 1 means that the microbead comes back to the original position, whereas smaller values account for a decrease of the elastic recovery and a transition to the nonlinear regime (creep response and fluid regime).

From the creep measurements it is then possible to estimate the storage (or elastic) modulus $G'(\varepsilon)$ and compare the results obtained from the microrheological measurements with those obtained from the rheometer. As the name suggests, the elastic modulus is related to the instantaneous elastic response of the material. The elastic modulus is here-calculated, for both the measurement techniques, as $G' = \sigma/\varepsilon$ at a time equal to 3 seconds after that the stress is turned on. Shorter times cannot be considered as the rheometer experiments are characterized by an initial transient phase related to the inertia of the measurement device (see Figure 3.18). Therefore, this can result in a certain error in the elastic modulus estimation as, at that time, a non-negligible creep deformation can be observed. However, a good agreement between the two measurement techniques was found, as it can be seen in Figure 3.22. The agreement is particularly good at low strain levels, whereas for higher values of the strain, the stress (and hence the storage modulus) seems to be overestimated in the microrheological measurements. This can be due to the assumption done in the stress calculation, for which the geometric prefactor $6\pi R$ was considered for the area estimation. This could explain the discrepancy observed in the stress levels, as this geometric prefactor is a good approximation only for small microbead displacements (and hence for small strain and stress levels). The here-proposed optical shooting technique would allow carrying out measurements for a better estimation of the

strain profile around the microbead in the three different yield stress regimes and for different strain levels. Regarding this point, optical shooting experiments are currently underway in this yield stress fluid, in which a significant amount of “small” fluorescent tracers, having sub-µm dimensions, are dispersed together with the usual 5 µm radius “big” polystyrene tracers. The strain profile around the optically shooted polystyrene microbead could be effectively estimated by tracking the movement of the small tracers. These measurements are still in progress and therefore were not included in this thesis. By observing Figure 3.22 it can be noted that the nonlinear regime starts at strain levels very small, between 5% and 10%, and the nonlinear behavior of the elastic modulus becomes more and more evident as the stress level is increased.

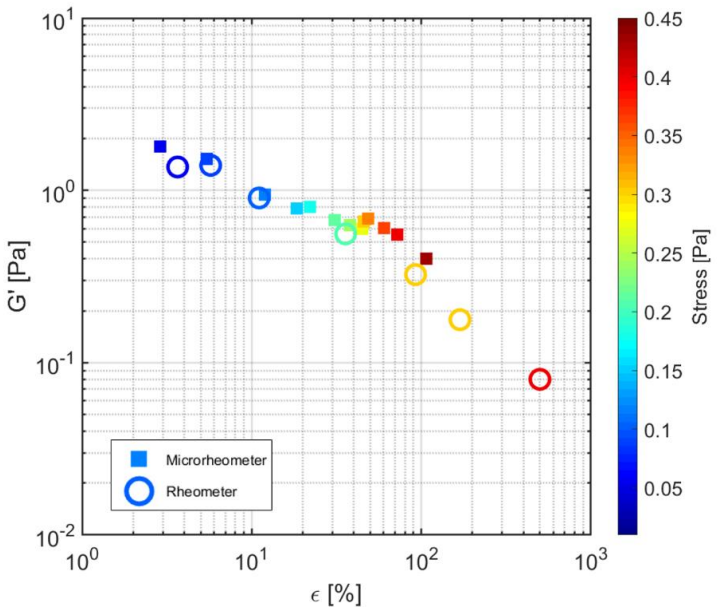

Figure 3.22: Estimation of the elastic modulus G' resulting from the creep measurements performed on the long fibers 0.4 wt% (HCO) 5.8 wt% (LAS) sample with the integrated microrheometer (colored squares) and with a conventional rotational rheometer (colored circles).

Measurements were then performed on the short fibers 0.4 wt% (HCO) 10 wt% (LAS) sample with the same experimental and analysis procedure. Following the same argumentations, from the strain-time curves it was possible to estimate a value of the yield stress of 0.3 Pa from the rheometer measurements and of 0.38 Pa from the microrheological experiments. These values were derived by considering a creep measurement time of 10 seconds. As previously observed for the long fibers, even for this sample the yield stress value derived from optical shooting microrheology is larger than that obtained using a conventional rheometer. Figure 3.23 a) shows the recovery-related quantity $\varepsilon_{OFF}/\varepsilon_{ON}$ as a function of the maximum strain ε_{ON} and of the applied stress (see color bar). It must be noticed that, differently from the long fibers, a significant creep was

measured even for low stress values. The result was that the linear elastic regime was not observed in the short fibers measurements, as proven by the fact that the maximum microbead recovery is equal to around 80 % (blue point). By increasing the applied stress, the material response becomes more and more nonlinear, as shown by the decrease of $\varepsilon_{\mathrm{OFF}}/\varepsilon_{\mathrm{ON}}$, in an analogous way to the long fibers. The same trend displaying the nonlinear behavior of the material can be appreciated even in Figure 3.23 b), which shows the comparison of the elastic modulus G' derived from the macroscopic and microscopic techniques. As before, the elastic modulus is calculated at a time equal to 3 seconds after that the stress is turned on. A good agreement between the two measurement techniques was found. Moreover, the data agree quite well even for high levels of the stress, differently from what observed for the long fibers sample. The reason could be related to the fact that smaller strains have been reached in the short fibers measurement (maximum percentage strain around 60% against a value larger than 100% for the long fibers sample). Therefore, this could result in a better estimation of the area, and hence of the applied stress, as the geometric prefactor $6\pi R$ is a good approximation of the strain field in case of small microbead displacements.

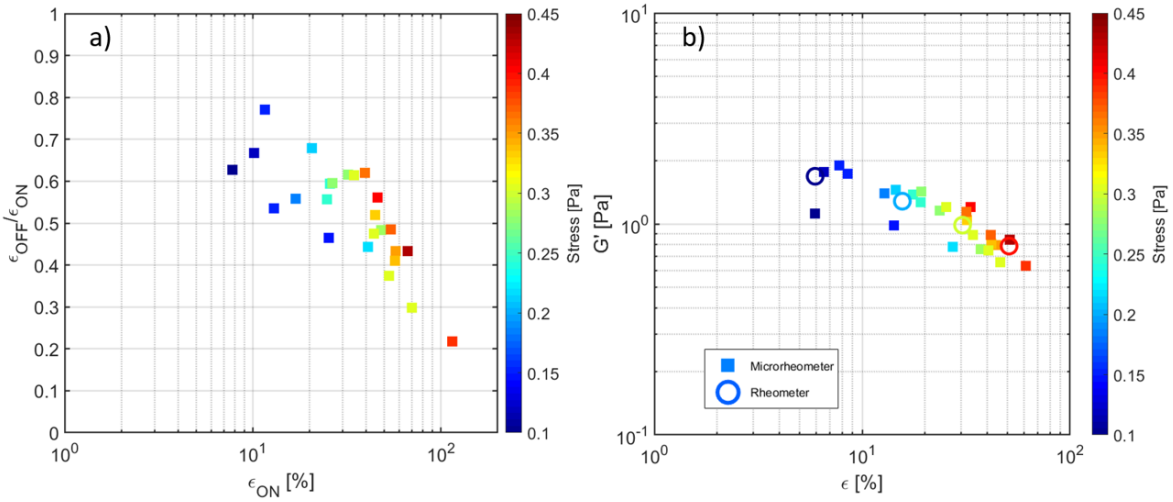

Figure 3.23: Results obtained from creep and recovery measurements performed on the short fibers 0.4 wt% (HCO) 10 wt% (LAS) sample: a) Estimation of the microbead recovery $\varepsilon_{OFF}/\varepsilon_{ON}$ obtained by means of the integrated microrheometer; b) Elastic modulus G' resulting from the creep measurements performed with the integrated microrheometer (colored squares) and with a conventional rotational rheometer (colored circles).

A worth-noticing aspect of the here-presented optical shooting technique is that it allowed studying the nonlinear response of yield stress fluids thanks to the significantly high optical forces that can be applied to a tracer. Specifically, it was possible to apply a maximum force of around 400 pN to a polystyrene microbead, which represents a value

significantly larger with respect to the forces commonly applicable with standard optically-based microrheological techniques such as single-beam optical tweezers.

4. Realization of a microrheometer for oscillatory microrheology

In this chapter the design, realization and validation of an optofluidic microrheometer for oscillatory microrheology will be presented. Differently from the previously described optical shooting procedure, in this new configuration a microbead is sinusoidally oscillated at a certain frequency and stress level. This allows deriving the frequency-dependent viscoelastic properties of the surrounding medium by monitoring the microbead movement in response to the externally applied stress. The optofluidic chip employed for these measurements is the same described in the previous chapter. In order to perform the optical modulation, an integrated Mach-Zehnder thermo-optical modulator is included in the setup. The Mach-Zehnder modulator fabrication and characterization will be initially described. The chapter will continue with the presentation of the experimental setup, the measurement protocol and data processing, with a particular attention to the calibration procedure. The system validation, performed by measuring aqueous worm-like micellar solutions (well-studied viscoelastic systems), will be finally discussed. The measurements were performed at different temperatures and concentrations and were compared with the existing literature and results from experiments performed with a conventional rheometer. As it will be shown, the integrated microrheometer can be exploited to perform active-microrheological measurements by accessing a wide range of frequencies, optical forces and temperatures. In particular, frequency experiments in the range [0.06-60] rad/s have been carried out.

The results of this activity are currently submitted for publication in *Nature-Scientific Reports*.

4.1 Integrated system description

The oscillatory microrheometer is realized by a cascade of two integrated devices: an electrically-driven thermo-optical modulator, based on a Mach-Zehnder interferometer realized on a glass substrate, and the optofluidic chip previously described, based on the counter-propagating configuration. The Mach-Zehnder interferometer can be used to modulate the optical power emitted by the two facing waveguides in a well-controlled manner. In this way it is possible to sinusoidally oscillate a trapped microbead in the medium under study. The microbead is sinusoidally oscillated at a precise frequency thanks to the imposition of a precise force pattern, well known in amplitude and time. The

rheological properties of the surrounding medium can be derived by tracking the microbead movement as a function of time.

4.1.1 Working principle

The two microrheometer fundamental building blocks, i.e. the Mach-Zehnder interferometer and the optofluidic chip, are serially connected by optical fibers. The Mach-Zehnder interferometer allows modulating the optical power emitted by the two facing optical waveguides in the optofluidic chip. All the details about the optofluidic chip fabrication, design and working principle can be found in Section 3.1.1. The Mach-Zehnder interferometer consists of two cascaded 50:50 directional couplers, as shown in Figure 4.1. A gold resistor placed near one of the two straight arms between the two directional couplers acts as an electrically-driven thermal phase shifter.

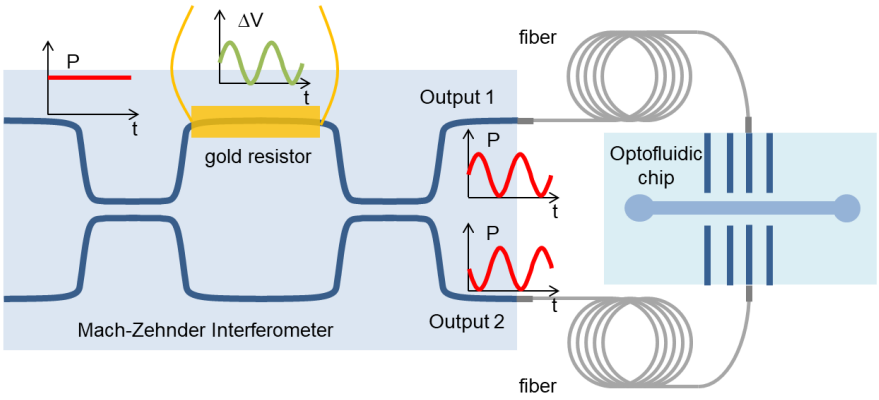

Figure 4.1: Schematic representation of the integrated microrheometer consisting of two cascaded glass chips. The integrated Mach-Zehnder interferometer (on the left) converts a sinusoidally oscillating electrical signal in a sinusoidally oscillating optical power. The two outputs of the modulator are fiber-pigtailed to the optofluidic chip (on the right), in which the oscillating optical power allows sinusoidally moving the trapping position in the microfluidic channel.

Each directional coupler can be thought as a beam splitter which equally divides the incoming optical power in the two output arms, while introducing even a $\pi/2$ phase delay in the light beam that couples to the cross arm. Therefore, in case the interferometer is perfectly balanced (i.e. no phase difference is produced while light travels in the two straight arms), the result will be destructive interference at Output 1. This is because the light beam which propagates without crossing any couplers will have a phase difference equal to π with respect to the optical beam which crossed both the directional couplers. Conversely, the two contributions will be in phase at Output 2, resulting in constructive interference. If a phase shift, in the range $[0, \pi]$, is introduced in one of the two arms, it is

possible to tune the amount of optical power in output from each port of the Mach-Zehnder interferometer, thus allowing to precisely change the power ratio between the two output ports. In our configuration, a relative phase shift between the two arms can be accumulated by taking advantage of the thermo-optic effect (i.e. a change of the refractive index resulting from a temperature variation) in glass. To exploit this effect, a resistive heater is realized next to one of the two interferometer arms [145], as shown in Figure 4.1. The output waveguides of the Mach-Zehnder interferometer are connected to the waveguides of the optofluidic chip by optical fibers, such that by electrically driving the interferometer resistor, it is possible to change the trapping position of the microbead inside the microfluidic channel. Specifically, by properly applying an oscillating voltage (at an angular frequency ω) to the interferometer resistive heater, it is possible to impose an oscillation of the trapped microbead inside the microchannel at the same angular frequency.

4.1.2 Mach-Zehnder modulator: fabrication and characterization

The Mach-Zehnder modulator was fabricated by the Fastgroup. FLM was used both to write the waveguides in the two glass chips and to pattern the gold resistive heater on the interferometer chip surface. A detailed description of the Mach-Zehnder interferometer fabrication process can be found in [145]. The modulator fabrication process basically consists of three different steps: (i) waveguides inscription by FLM, (ii) deposition of a gold layer on the chip surface and (iii) patterning by femtosecond laser of the metallic layer on the surface to define the resistive heater shape. The integrated modulator is fabricated in an alumino-borosilicate glass substrate (Corning EAGLE-XG) by using a Yb:KYW cavity-dumped mode-locked laser oscillator emitting 300 fs pulses at 1030 nm wavelength and 1 MHz repetition rate. The optical waveguides are realized by focusing 240 nJ pulses with a 50× objective (NA = 0.6) at a depth of 30 µm below the glass surface and by translating the sample at 20 mm/s (Aerotech FiberGlide translation stages). The resulting waveguides are single mode at 1070 nm, with a mode diameter of about 8 µm. In order to assess its performance, the Mach-Zehnder optical modulator was initially characterized before its implementation in the microrheological system. Insertion losses, defined as the overall losses introduced by the modulator in the setup, of about 4 dB were estimated. In order to connect the interferometer to the optofluidic chip for performing the rheological experiments, the interferometer output waveguides are pigtailed to a fiber array. This fabrication step increased the insertion losses, which were finally estimated to be around 6.2 dB. The insertion losses increase is caused by a mismatch between the waveguide-to-waveguide distance in the chip and the core-to-core distance in the fiber array. This results in coupling losses significantly higher than those commonly achievable using a single-fiber array. However, this value of the insertion losses can be easily improved

in future fabrications. The optical transmission at the two output ports of the device was then measured as a function of the bias voltage applied to the resistive heater, which is about 125 Ω, and the results are shown in Figure 4.2 a). This characterization is crucial in order to identify the DC-bias voltage which allows to equally divide the incoming optical power between the two modulator output ports.

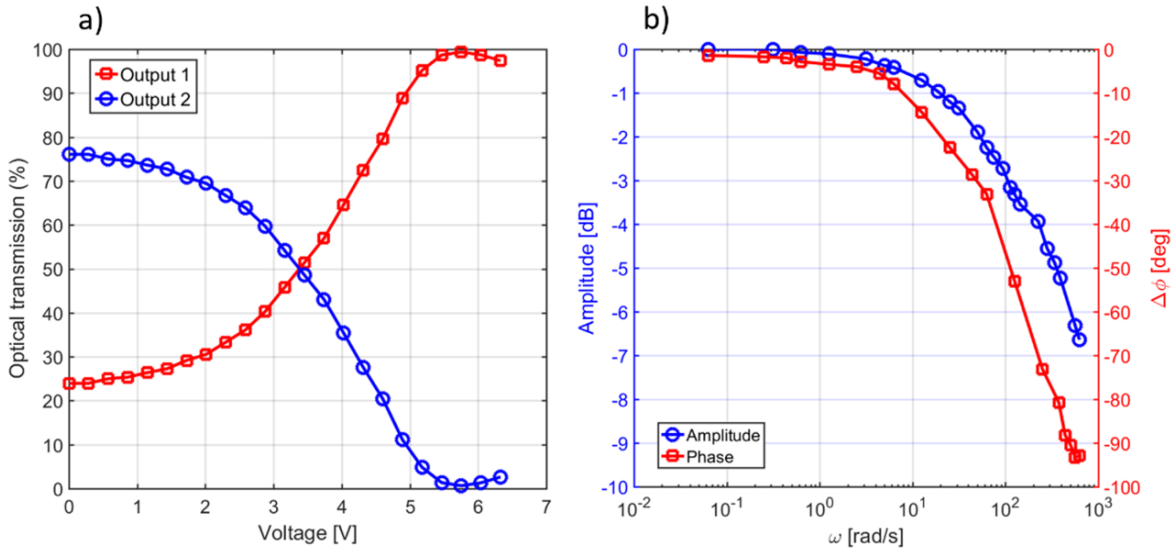

Figure 4.2: a) Optical transmission at the two output ports of the Mach-Zehnder modulator as a function of the applied voltage on the resistive heater. The optical transmission at $V = 0$ does not reach 100% on output 2 due to couplers non-idealities. b) Amplitude- and phase-frequency response of the Mach-Zehnder modulator.

The frequency response of the Mach-Zehnder modulator was then estimated by superimposing a small ($V_{pp} < 1V$) sinusoidal signal, oscillating at different frequencies (from 0.01 Hz to 100 Hz), on the bias voltage. It should be noted that, differently from the commonly employed electro-optical modulators based on $\chi^{(2)}$ materials (such as, for example, Lithium Niobate) [146,147], in the here-presented situation the modulator transfer function is not sinusoidal with respect to the applied voltage V. The reason can be found in the fact that the dissipated electrical power, which is responsible of the phase shift due to the thermo-optic effect, depends on V^2 instead of V. Nevertheless, in our situation, when a small sinusoidal signal is superimposed on the DC-bias, properly chosen to obtain a 50:50 power ratio between the two modulator output ports, the transfer function is sufficiently linear to induce a sinusoidal variation of the optical power at the two outputs. The optical power in output from the Mach-Zehnder modulator was sent to a photodiode connected to an oscilloscope so that to acquire a voltage signal proportional to the modulator output power. Figure 4.2 b) shows the measured amplitude-frequency and phase-frequency response of the modulator. The amplitudes are normalized to the value

acquired at the lowest angular frequency, while $\Delta\phi$ is defined as the phase difference between the voltage signal applied to the resistive heater and the voltage signal recorded by the photodiode. From the obtained results it was possible to estimate the value of the -3 dB cut-off frequency to be around 17 Hz.

4.2 Experimental procedure

In this section the experimental setup and measurement protocol for performing the oscillatory microrheological experiments will be discussed. The last part of this section will be dedicated to the presentation of the fundamental equations and data processing required for the determination of the viscoelastic properties of the sample under test.

4.2.1 Experimental setup

A schematic representation of the experimental setup is shown in Figure 4.3. All the instruments are remotely controlled by a user interface developed in a LabVIEW environment. Concerning the optical part of the setup, a CW Yb-doped fiber laser (YLD-10-1064, IPG Photonics, P_{max} = 10 W at 1070 nm) is employed as optical source and connected to one input of the Mach-Zehnder optical modulator by optical fiber. The modulator is driven by a voltage-function generator (Aim-TTi TG 2000 20MHz) and its two output ports are connected to a 99/1 fiber power splitter (FPS) each. The optical fibers carrying 99% of the optical radiation are connected to the waveguides of the optofluidic chip, in order to trap and manipulate the microbeads inside the microfluidic channel, while the 1% of the power is input to two photodiodes, connected to a National Instruments data acquisition system (NI DAQ). The two photodiodes allow a real-time monitoring and recording of the power levels in the two optical branches of the setup. As for the optical shooting experiments, the optofluidic chip is mounted on a phase-contrast inverted microscope and the microbead movement is recorded by a CCD camera connected to the microscope. Moreover, the setup is equipped with a temperature controller circuit, realized by a Peltier element placed just below the optofluidic chip and a thermocouple (TC) placed on the top surface of the chip, which gives the feedback signal for the Peltier element. The pressure and hence the fluid movement inside the microchannel can be controlled by a LabVIEW-driven micropump, whose tubing is screwed to one of the two connectors glued on the top surface of the optofluidic chip. As in the setup for optical shooting microrheology, a thin piezoceramic disk is placed under the optofluidic chip and is driven by a LabVIEW-controlled function generator in order to generate an acoustic standing wave in the microfluidic channel and hence perform the acoustophoretic prefocusing.

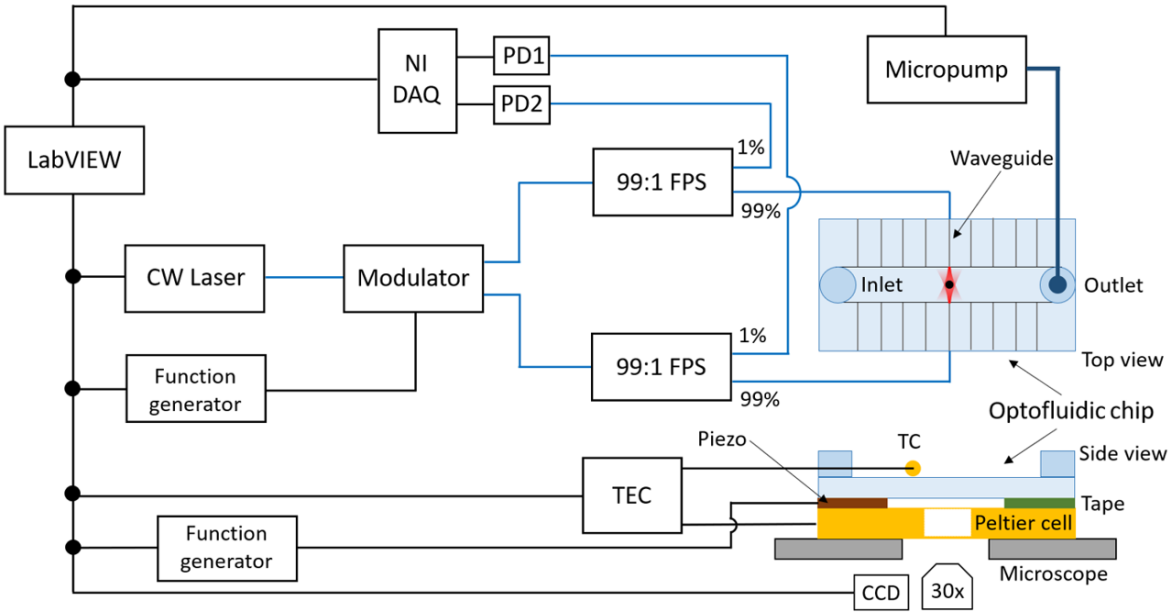

Figure 4.3: Schematic diagram of the experimental setup for oscillatory microrheology. The blue lines represent the optical fiber connections while the black lines represent the electrical cable connections. TEC: temperature controller circuit; CCD: charge-coupled device; TC: thermocouple; FPS: fiber power splitter; PD: photodiode.

4.2.2 Measurement protocol and data acquisition

In an analogous way to optical shooting microrheology, the sample to be characterized is prepared by dispersing a small amount of microscopic tracers into the material under test and is then injected into the microfluidic chip reservoir by means of a standard micro-pipette. Polystyrene microbeads with 5 µm radius (Sigma Aldrich 72986) have been used as tracers. The measurement procedure consists of different steps. After the sample injection, a single microbead is trapped by the optical forces exerted by the two counter-propagating laser beams emitted by the facing waveguides. The pressure is then adjusted thanks to the LabVIEW-controlled micropump in order to have no sample flow inside the microfluidic channel. The DC-bias voltage of the modulator is then properly selected so that the microbead trapping position is exactly in the microchannel center. The temperature can be set to the desired value by actuating the temperature controller circuit, waiting several minutes (typically around 10) in order to thermally stabilize the system. The microbead is then sinusoidally oscillated by adding a small sinusoidal voltage signal to the DC-bias voltage applied to the modulator resistive heater. The viscoelastic properties of the material under test are investigated in the range [0.06-60] rad/s. For each angular frequency measurement, the microbead position and the voltage signals from the two photodiodes (PD1 and PD2 referring to Figure 4.3) are acquired. Specifically, the microbead movement is monitored by a CCD camera, which allows recording the tracer position as a

function of time, thanks to a Lab-VIEW tracking software. The voltage signals from the two photodiodes, which are proportional to the optical power in the two sides of the setup, are instead acquired by the NI DAQ.

4.2.3 Fundamental equations and data processing

As previously discussed, the microbead position, $x(t)$, and the two voltage signals acquired by the photodiodes are recorded while sinusoidally oscillating the microbead at a certain angular frequency. This measurement procedure is repeated several times by oscillating the microbead at different angular frequencies, so as to span the desired frequency-range. The strain $\varepsilon(t)$ can be defined in the usual way starting from the microbead position as $\varepsilon(t) = (x(t) - x_0)/(2R)$, where R is the microbead radius and x_0 is the trapping position corresponding to the oscillation center. The stress acting on the tracer, $\sigma(t)$, depends on the net force resulting from the difference between the optical forces exerted by the two counter-propagating beams on the tracer. As the two voltage signals recorded by the photodiodes are proportional to the optical power carried by the two counter-propagating beams, the difference between the photodiodes voltage signals, $V_{ph}(t)$, allows determining the stress acting on the microbead, which is given by $\sigma(t) = \beta \cdot V_{ph}(t)$, with β being a calibration constant to be found. The determination of the constant β can be performed by calibrating the system with Newtonian fluids of known viscosity (such as milli-Q water), as it will be discussed in the next section. It should be noted that the voltage difference signal, $V_{ph}(t)$, is a sinusoidal signal as resulting from the difference of two sinusoidal signals with the same offset value. As a sinusoidal modulation is applied, the optical stress acting on the tracer will be of the form:

$$\sigma(t) = \beta \cdot V_{ph}(t) = \beta \cdot V_{ph,0} \cdot \sin(\omega t) = \sigma_0 \cdot \sin(\omega t) \tag{4.1}$$

where $V_{ph,0}$ is the amplitude of the voltage difference signal, ω is the angular frequency at which the measurement is performed and $\sigma_0 = \beta \cdot V_{ph,0}$ is the amplitude of the stress. By assuming that the measurements are performed in the linear viscoelastic regime, as it will be proved, the resulting strain, as measured by the bead displacement, can be written as:

$$\varepsilon(t) = \frac{x(t) - x_0}{2R} = \frac{A \cdot \sin(\omega t - \delta)}{2R} = \varepsilon_0 \cdot \sin(\omega t - \delta) \tag{4.2}$$

in which A is the amplitude of the microbead oscillation, δ is the loss angle and $\varepsilon_0 = A/(2R)$ is the amplitude of the strain. The temporal evolutions of $x(t)$ and $V_{ph}(t)$ are acquired over 20 periods for each single-frequency measurement included in the

investigated frequency range. From the recorded signals it is possible to derive the values of ε_0, $V_{ph,0}$ and δ corresponding to the different angular frequencies (ω). In addition, once the calibration constant β is known, even σ_0 can be immediately calculated. Once all these quantities have been determined, it is possible to calculate the complex compliance J^*, as defined in Section 2.3.3:

$$J^* = J' - iJ'' = \frac{\varepsilon_0}{\sigma_0}(\cos\delta - i\sin\delta) \tag{4.3}$$

The complex compliance naturally describes the rheological properties of the material under test in case stress-controlled deformations are applied. Recalling the arguments presented in Section 2.3.3, the storage compliance J' accounts for the elastic contribution while the loss compliance J'' accounts for the viscous component. A good description for several viscoelastic fluids characterized by a single relaxation time and low frequency viscous behavior, as the aqueous worm-like micellar solutions that have been measured for the system validation, is given by the Maxwell model, which is represented by the serial connection of a purely elastic spring and a purely viscous damper. By considering the constitutive equation which describes the Maxwell model, it is possible to write the complex compliance as:

$$J^* = J' - iJ'' = \frac{1}{E} - i\frac{1}{\omega\eta} \tag{4.4}$$

where η is the viscosity and E is the elastic modulus. From these two quantities it is then possible to calculate the relaxation time t_R, which sets the crossover between the viscous and elastic regimes, as η/E. Finally, the viscoelastic properties of the material under test can be expressed in an analogous way in terms of the complex modulus $G^* = G' + iG''$, with the storage modulus G' accounting for the elastic contribution and the loss modulus G'' describing the viscous component. Assuming that measurements are performed in the linear viscoelastic regime, the complex modulus G^* can be simply calculated from the complex compliance J^* by means of Eq. 2.28.

In order to give an estimation of the error resulting from the measurement of the complex compliance, it is possible to sum all the relative errors contributions affecting the quantities appearing in Eq. 4.3, which can be usefully rewritten as:

$$J^* = J' - iJ'' = \frac{A}{2R\beta \cdot V_{ph,0}}(\cos\delta - i\sin\delta) \tag{4.5}$$

Concerning the amplitude of the bead oscillation A, a relative error equal to 3% and 9% was determined (as the ratio between the standard deviation and the amplitude average value resulting from the experiments) at the lowest and highest oscillation frequency, respectively. An uncertainty equal to 2% is considered to affect the radius of the polystyrene beads used in the oscillatory experiments (Sigma Aldrich 72986, R = 5 μm), as specified by the product data sheet. By analyzing the calibration measurements performed in water, whose procedure will be described in the next section, it was possible to assess the uncertainty in the β calibration constant to be 1.5% and the uncertainty in the calculation of the trigonometric functions $\cos(\delta)$ and $\sin(\delta)$ to be 1%. Lastly, the relative error in the measurement of $V_{ph,0}$ was measured to be equal to 0.5% and 2% for low and high oscillation frequency, respectively. Summing all the contributions, the relative error in the measurement of the complex compliance, and hence of the rheological properties of the sample under study, was estimated to be comprised between 8% (at the lowest measured frequency) and 15.5% (at the highest measured frequency).

4.3 Calibration procedure

In this section the system calibration will be discussed. Two calibration procedures were performed: stress calibration and temperature calibration. The stress calibration consisted in finding the previously introduced constant β, which allowed determining the stress acting on the microbead. Thanks to the temperature calibration, it was instead possible to estimate the temperature increase in the microchannel due to the laser heating effect.

4.3.1 Stress calibration

As anticipated, the calibration constant β can be determined by performing oscillatory measurements of materials characterized by known rheological properties such as water. In case of water, the complex compliance J^* simply reduces to its imaginary part J'', which can be written as:

$$J'' = \frac{\varepsilon_0}{\sigma_0}\sin\delta = \frac{\varepsilon_0}{\beta \cdot V_{ph,0}} \tag{4.6}$$

where $\sin(\delta) = 1$ due to the purely viscous nature of water, as it was even experimentally measured.

Considering Eq. 4.4 we have that $J'' = 1/(\omega\eta_{water})$ and by combining this relation with Eq. 4.6 it is possible to determine the calibration constant β as:

$$\beta = \frac{\varepsilon_0}{V_{ph,0}} \cdot \omega\eta_{water} \tag{4.7}$$

Oscillatory experiments performed at different angular frequencies ω gave the same value of the calibration constant β. This confirmed the independence of β on the oscillation frequency. It must be noted that the calibration procedure was performed in water using a low optical power (< 100 mW) in order to avoid a significant laser-induced heating effect. However, this calibration constant depends on geometrical data of the light beam, the refractive index n_P of the microbead and the refractive index n_X of the material under test. While the first two quantities are fixed for all the measurements that employ the same optofluidic chip and microbeads, n_X can obviously change as materials with different refractive indexes can be measured. As the value of n_X significantly affects three different parameters (the single-photon momentum, the beam divergence and the reflection coefficient at the microbead surface), numerical simulations based on PRO approximation were carried out to determine the appropriate force correction factor depending on the material under study.

4.3.2 Temperature calibration

As discussed at the beginning of the chapter, the idea was to validate the oscillatory microrheometer by measuring aqueous worm-like micellar solutions. These viscoelastic media exhibit a strong temperature dependence. In particular, the relaxation time of worm-like micellar solutions significantly changes even with a temperature variation of few degrees. Therefore, in order to validate the integrated microrheometer, a precise knowledge of the temperature inside the microfluidic channel was required. Thanks to the temperature calibration it was possible to compare our experimental results with those obtained using a conventional rheometer, which was set at a temperature equal to the one estimated in the microchannel. This allowed a reasonable comparison between micro- and macro-rheological measurements and hence the validation of the microrheometer.

The temperature reached in the microchannel during oscillatory measurements was estimated to be equal to $T' = T + \Delta T$, where T is the temperature measured by the thermocouple (TC) and ΔT is the temperature increase due to the laser heating effect. In particular, ΔT depends on the optical power in the microchannel and on the sample under test. As discussed in Section 4.2.1, the TC sensor is placed on the top surface of the chip and gives the feedback signal for the Peltier cell, which is used to change the system

temperature. In order to determine the laser-induced ΔT for aqueous solutions, the temperature-dependent fluorescence of Rhodamine B was used. Rhodamine B was employed because it is characterized by a well-studied temperature-dependent fluorescence in the range between 0 and 100 °C [148,149], making it a useful temperature probe for aqueous solutions. An aqueous solution of 0.1 mM Rhodamine B was prepared and injected in the microfluidic channel. Fluorescence imaging of the dye was carried out using the previously described microscope-based setup coupled with a fluorescence equipment consisting of a mercury arc lamp (Nikon C-SHG1) and an appropriate filter cube (TxRed, excitation: 540-580 nm; emission: 600-660 nm). The photobleaching effect was accounted by measuring the decrease of the fluorescence emission intensity due to the excitation light, whose level was kept constant during the acquisition time for all the experiments. The photobleaching estimation was performed by simply measuring the reduction of the fluorescence intensity as a function of time, without laser radiation. This correction was then applied to all the reported data.

First, a calibration curve was derived to accurately determine the dependence of Rhodamine B fluorescence on the temperature in our system. Measurements of fluorescence emission intensity were carried out at different temperatures (in the range from 18 to 45 °C) by actuating the Peltier cell. Reasonably, the temperature displayed by the TC sensor was assumed to coincide with the one in the microfluidic channel, as the laser radiation is switched off during this initial calibration. The resulting intensity (normalized to the value measured for the lowest temperature, equal to 18 °C) versus temperature variation is shown in Figure 4.4. As it can be seen, in the explored temperature range the intensity variation is almost linearly dependent on the temperature variation and the measured values agree with those reported in scientific literature [148].

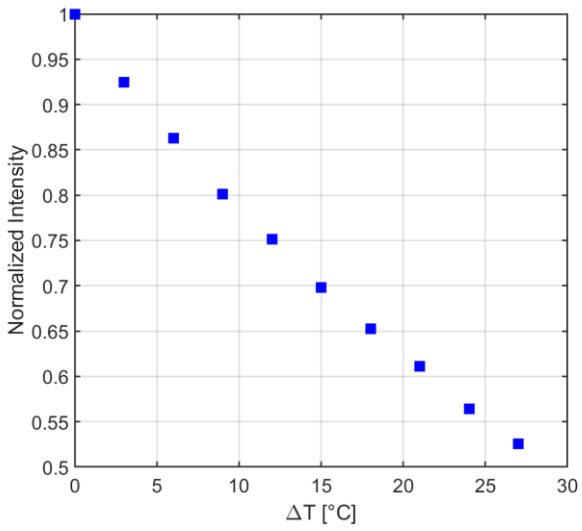

Figure 4.4: Normalized fluorescence intensity as a function of ΔT. All the intensities are normalized to the value acquired at the lowest temperature, equal to 18 °C.

The laser-induced heating was then estimated by measuring the fluorescence intensity variation in the center of the microfluidic channel, as this is the area where the microbead is oscillated during the microrheological measurements. The DC-bias voltage of the modulator was properly set in order to have the same power emitted by the two facing waveguides so that to achieve a symmetric illumination condition. The optical power effectively present inside the microfluidic channel is well known thanks to the system calibration with water. Considering an optical power of 0.5 W in the microchannel, matching the power used in the oscillatory measurements reported in the following part of the chapter, a laser-induced heating ΔT equal to (5$\pm$1) °C was observed. As the optical power was kept constant for all the measurements, a fixed laser-induced offset ΔT of 5 °C, with respect to the temperature T measured by the TC sensor, was considered for evaluating the sample temperature ($T' = T + \Delta T$). It is worth noticing that the estimated temperature increase due to the laser-heating effect is in line with the value of (13$\pm$2) °C/W estimated by Ebert et al. [150] in a similar dual beam laser trap geometry.

As a final consideration, it must be pointed out that the temperature calibration was carried out for oscillatory microrheology but not for optical shooting microrheology for two main reasons. The first one is that an exact determination of the temperature variation in case of optical shooting experiments is more difficult with respect to oscillatory experiments. One reason is that the temporal duration of an optical shooting experiment is significantly short, in the order of few seconds. Moreover, each optical shooting has a different duration, depending on the applied optical force. When an optical shooting is performed, the laser radiation emitted by one waveguide is abruptly blocked and hence a steady temperature could not be reached during the measurement time. Differently, in an oscillatory experiment the microbead is oscillated at a fixed optical power for a certain time before the data acquisition starts and therefore the system can reach a steady temperature. In addition, while in oscillatory experiments the microbead is always oscillated in the microchannel center, in an optical shooting-based experiment the microbead can move along all the channel width. This further increases the complexity of the temperature estimation, as the temperature variation is different along the channel width due to the optical beam divergence. The second and most important reason is that for most of the performed optical shooting experiments the optical power was lower than the one used for the next reported oscillatory experiments. This resulted in a lower laser-induced heating, whose determination was not strictly necessary for the estimation of the rheological properties of the medium. As discussed at the end of the previous chapter, large optical forces (and hence large optical powers) were used to study yield stress fluids. However, as previously mentioned, the measured yield stress fluids are characterized by a negligible temperature dependence in the range of reached temperatures. Nonetheless, if optical shooting experiments at high power need to be carried out in media showing a

strong temperature dependence, the estimation of (13±2) °C/W can be used as a first order approximation for the laser-induced heating effect.

4.4 Oscillatory microrheology measurements of viscoelastic systems

After the system calibration, the performance of the oscillatory microrheometer was tested by measuring viscoelastic solutions of surfactant worm-like micelles and comparing the obtained results with those from macroscopic rheological experiments. Some surfactant molecules in solution can self-assemble into elongated, cylindrical micelles, which are commonly labelled as *worm-like micelles* [151]. These complex systems display distinct rheological properties and are widely used in different consumer products. Worm-like micelles show many analogies to covalently bonded polymers, but they also continuously break and reform and for this reason they are even defined as *living polymers*. Above a critical concentration of surfactant or counterion/surfactant ratio, the worm-like micelles begin to overlap and then create an entangled network, which shows the typical rheological characteristics of a Maxwell viscoelastic material. This micellar network is therefore characterized by an elastic response at high frequency, while at low frequency the system can rearrange and mainly behaves like a Newtonian fluid. The relaxation time which separates these two different regimes results from the combination of two mechanisms for stress relaxation: reversible breakage and reptation, i.e. the constrained diffusion of a micelle within the tube of the neighbouring micelles [152].

4.4.1 Measurements of worm-like micellar solutions

Aqueous worm-like micellar solutions composed by Cetylpyridinium Chloride (CPyCl) and Sodium Salicylate (NaSal) were used to validate the microrheometer performance. The micellar solutions were prepared by the Complex Fluids and Molecular Biophysics group. The same group performed even the rheometer measurements on the same samples. They prepared solutions using CPyCl as a surfactant and NaSal as a counterion in milli-Q water at twice the final concentration and then mixed them at equal volumes to obtain 100 mM CPyCl/50 mM NaSal and 100 mM CPyCl/55 mM NaSal. All the chemicals were purchased from Sigma Aldrich. The final solutions were gently stirred for more than 24 hours and then stored at room temperature. The solutions remained stable over a few weeks without significantly changing their rheological properties. Microrheological experiments were carried out maintaining the system at a controlled temperature thanks to the actuation of the Peltier cell. In these conditions, CPyCl/NaSal micellar solutions display a well-studied rheological behavior [151,153], which can be used to validate the proposed integrated system. Oscillatory measurements were initially

performed on a 100 mM CPyCl/50 mM NaSal solution maintaining the TC temperature $T = 24\ °C$. Considering the average laser-induced heating $\Delta T = 5\ °C$, the sample temperature was estimated to be $T' = 29\ °C$. As expected, the micellar solution displays different rheological regimes depending on the investigated frequency, as it can be seen in the stress-strain (Lissajous) plots shown in Figure 4.5 a). The values of the stress, strain and loss angle δ for each measured frequency can be directly derived from the recorded signals, as previously explained in Section 4.2.3. For low values of the angular frequency, the system behaves as a purely viscous fluid (a circle in the stress-strain plane), whereas for high values of the angular frequency (> 20 rad/s), the micellar solution response is characterized by a strong elastic, in-phase component, which is evident by the fact that the Lissajous plots become elongated, tilted ellipses.

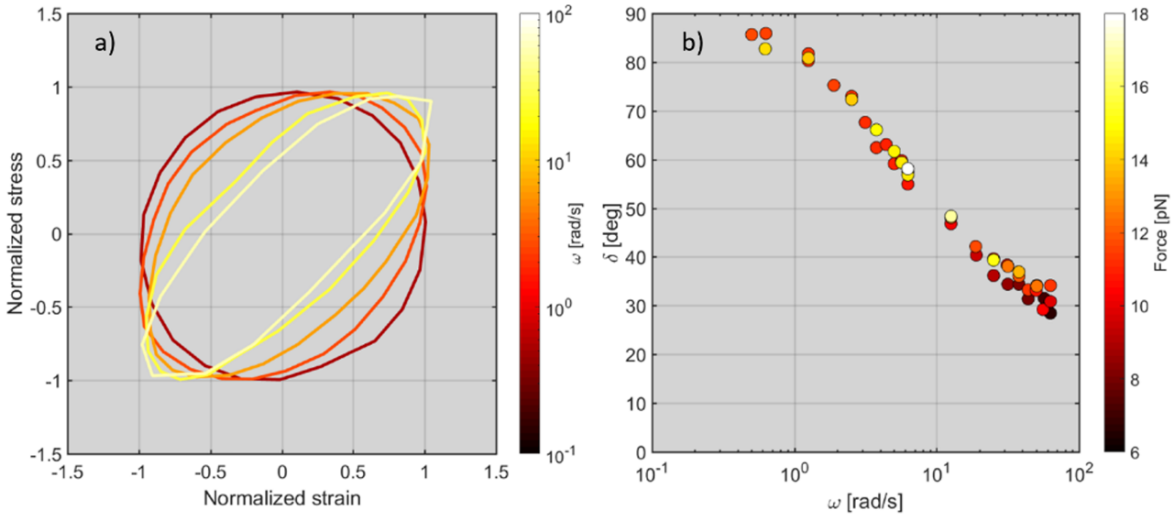

Figure 4.5: Results from the measurements of an aqueous worm-like micellar solution of 100 mM CPyCl/50 mM NaSal at an estimated sample temperature $T' = 29\ °C$. a) Lissajous plots for different angular frequencies. b) Loss angle δ as a function of angular frequency and optical force.

The loss angle δ as a function of ω, which is reported in Figure 4.5 b), quantifies the transition between these two different behaviors, going from almost 90° at low ω (viscosity-dominated regime) to less than 30° for high values of ω (elasticity-dominated regime). By considering the Maxwell model for describing the rheological behavior of this sample, the ω-dependence of the viscosity η and of the elastic modulus E can be derived (see Figure 4.6). As it could be expected, for an increasing angular frequency, the elastic modulus E increases, whereas the viscosity η decreases.

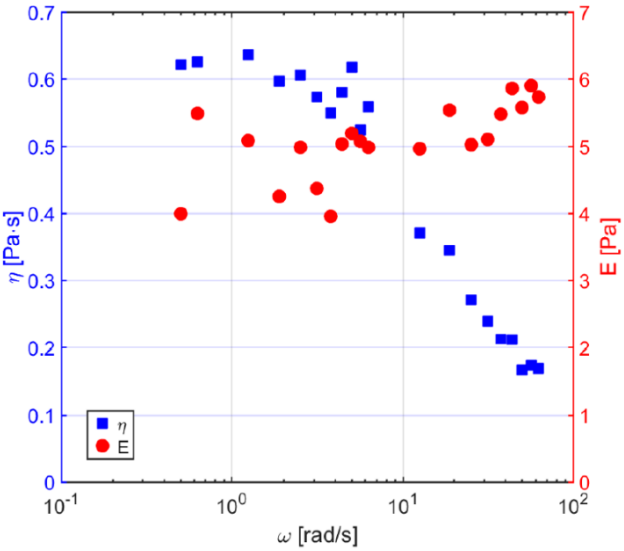

Figure 4.6: Results from the measurements of an aqueous worm-like micellar solution of 100 mM CPyCl/50 mM NaSal at an estimated sample temperature $T' = 29\ °C$. Viscosity η (blue squares) and elastic modulus E (red circles) as a function of angular frequency.

The microbead size is significantly larger than the mesh-size of the micellar network (few nm in our situation) and the limitation on strain linearity is simply set by the relative motion of the tracer [77]. As in the performed microrheological measurements the oscillation amplitude of the microbead was always measured to be within a few % of its diameter, the obtained results are expected to lie within the linear viscoelastic response of the micellar network. Nevertheless, in order to experimentally demonstrate the system linearity, oscillatory measurements at different angular frequencies for various imposed optical forces have been carried out. Various optical forces were applied by changing the amplitude of the small sinusoidal signal imposed to the modulator resistor, while maintaining the optical power in the microfluidic channel equal to 0.5 W. Figure 4.5 b) shows that both the loss angle δ and its ω-dependence are not affected by the applied optical forces, thus demonstrating that all the obtained results lie within the linear-response regime of the material under study.

Figure 4.7 a) shows the same results of the microrheological measurements performed on the 100 mM CPyCl/50 mM NaSal solution at an estimated sample temperature $T' = 29\ °C$ in terms of storage and loss modulus, G' and G'', respectively. As it can be observed, at low angular frequency $G'' \propto \omega$ is dominant over $G' \propto \omega^2$, as expected for a typical Maxwell viscoelastic material. Above a crossover frequency (the inverse of the relaxation time), the storage modulus G' becomes dominant over the loss modulus G'' and G' approaches a plateau value. The measurement uncertainty, calculated as the ratio of G' and G'' standard deviation over their average values, was found to be

around 12% on average, considering the different measured angular frequencies, and always lower than 20%. For this reason, no error bars are reported in Figure 4.7 a), where a logarithmic scale is used. The estimated scaling behavior, the values of the crossover frequency and of G' and G'' closely match values obtained from measurements performed with a conventional rheometer (Anton Paar MCR 302 with cone-plate geometry) at a temperature of 29 °C.

4.4.2 Effects of temperature and counterion concentration

Changes in the concentration of surfactant, type and concentration of counterions, or temperature can significantly alter the flexibility and length of the worm-like micelles, resulting in a change of the elasticity and relaxation time of the network [151]. Oscillatory experiments were then performed on the same micellar solution of 100 mM CPyCl/50 mM NaSal at a stable TC temperature $T = 21\ °C$ (resulting in an estimated sample temperature $T' = 26\ °C$) and the results are shown in Figure 4.7 b).

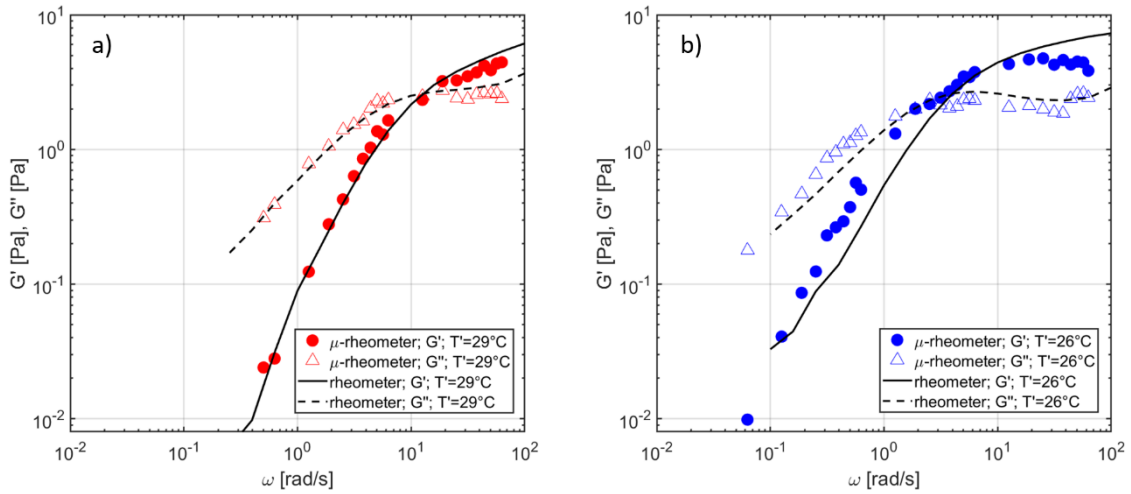

Figure 4.7: Results from the measurements of aqueous worm-like micellar solutions. a) Complex modulus of the 100 mM CPyCl/50 mM NaSal solution measured at a TC temperature $T = 24\ °C$ (estimated sample temperature $T' = 29\ °C$). b) Complex modulus of the 100 mM CPyCl/50 mM NaSal solution measured at a TC temperature $T = 21\ °C$ (estimated sample temperature $T' = 26\ °C$). The measurements carried out with the integrated microrheometer were compared with those performed using a conventional rheometer and the results showed a good agreement between the two data sets.

As it can be seen, the temperature decrease has as a result a shift of the relaxation time to a higher value (and therefore of the crossover frequency to a lower value) due to the fact that it increases the average time for micellar breakage. On the other hand, the temperature decrease has almost no effect on the value of the elastic plateau, which

mainly depends on the mesh size of the network, which is not affected by the increased average length of the worm-like micelles. The measurements performed with the microrheometer were compared with those carried out with a conventional rheometer at a temperature of 26 °C and a good agreement between the two data sets was found even in this case. The small discrepancy (horizontal shift) between the two data sets can be due to a small error in the estimation of the sample temperature in the microchannel.

Further measurements were then performed, by increasing the concentration of counterions, on a 100 mM CPyCl/55 mM NaSal micellar solution and were compared with those carried out on the 100 mM CPyCl/50 mM NaSal micellar sample. Both experiments were performed at the same TC temperature $T = 24\ °C$ (estimated sample temperature $T' = 29\ °C$). The increase of the counterions concentration partially screens the electrostatic repulsion between micelles, and therefore increases the energetic cost of scission. This makes the micelles longer and more flexible, resulting in an increase of the relaxation time and a decrease of the mesh size, which in turn results in an increase of the value of the elastic plateau, as it was experimentally verified from the results reported in Figure 4.8. Even in this situation, the measured trends are in agreement with previously reported results on the same micellar systems [153].

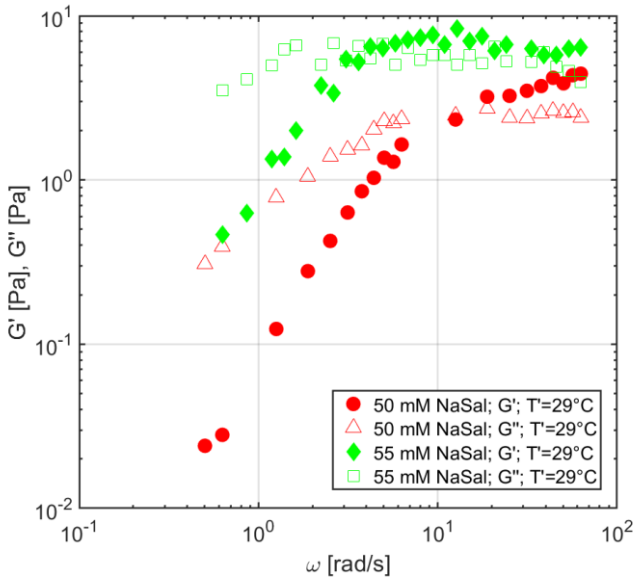

Figure 4.8: Results from the measurements of aqueous worm-like micellar solutions. Complex modulus of two different worm-like micellar solutions (100 mM CPyCl/50 mM NaSal and 100 mM CPyCl/55 mM NaSal) measured at the same TC temperature $T = 24\ °C$ (estimated sample temperature $T' = 29\ °C$).

4.4.3 Final remarks

The performances of a LoC oscillatory microrheometer based on a dual beam laser trap were reported. The integrated device allows performing active microrheological experiments and hence estimating the complex modulus of viscoelastic media in the frequency range [0.01-10] Hz with a very low sample consumption (< 1 µL) and with temperature setting capability. In conclusion, Chapter 3 and 4 highlighted the advantages of the integrated optofluidic microrheometer proposed in this thesis. In addition to the reduced sample consumption, the high integration level of the device ensures several benefits. The monolithic integration of the optofluidic chip provides an excellent calibration and measurement repeatability as no alignment of optical components is required. This represents a significant advantage with respect to microscope-based single-beam optical tweezers. Noteworthy, the chip portability offers the possibility to easily move the microrheological system from one lab to another. The here-presented device allows applying much larger forces with respect to conventional single-beam optical tweezers, as discussed at the end of Chapter 3. In addition, the use of a dual beam laser trap configuration allows trapping microbeads with a higher refractive index when compared to those generally allowed in conventional optical tweezers, thus further increasing the optical force. The wide range and precise control of the applicable optical forces provide a flexible use of the microrheometer, offering the possibility to perform active microrheological experiments, in linear and nonlinear regime, on a wide range of materials, ranging from aqueous polymer solutions and soft gels to stiffer materials and heterogeneous samples. Finally, even if not explicitly discussed in this work, the device can be employed to perform passive microrheological measurements, by simply monitoring the movement of optically trapped particles subjected to Brownian motion.

5. Acoustofluidic separation: a theoretical study

In this chapter a numerical study about the separation of fluid-suspended microparticles (such as microbeads and cells) by acoustophoresis will be presented. This is a minor project I have been working on during my PhD activity. The first part of the chapter will give a general introduction to acoustophoresis-based samples separation and will report the governing equations and parameters used for numerical simulations. The chapter will continue with the investigation of the impact on particle separation of different parameters, which will be divided in two groups: sample's "intrinsic" factors (i.e. the properties of the samples to be sorted) and "extrinsic" factors (i.e. factors related to the acoustofluidic system design and operation). The last section will specifically focus on the impact of both sample launch position and sample distribution at the input of the acoustofluidic system by an analytical study and numerical simulations of realistic configurations. This theoretical study shows how the device performance can be significantly improved by choosing the proper microfluidic channel dimensions and sample launch position, giving useful guidelines for the design of acoustofluidic-based LoC devices. All the here-discussed simulations were performed using custom MATLAB scripts.

The work regarding the impact of intrinsic and extrinsic parameters on the achievable separation efficiency has been published in [154]. The study regarding the impact of the sample launch position and sample distribution on the separation efficiency has been reported in [155].

5.1 Background knowledge

Over the past twenty years, microfluidic techniques and LoC systems successfully opened new perspectives in many different research areas, especially for cytology and chemistry. This success is mainly due to the intrinsic advantages of LoC devices with respect to standard technologies and to their ability to manipulate, detect and analyze biological samples at single cell level [18,156]. As already discussed, one of the main advantages offered by LoC technology relies in the possibility of integrating an increasing number of functionalities and actuators within microfluidic systems, thus increasing even further their possible applications. As an example, an actuation system which is currently attracting a significant attention from the scientific community is that based on the combination of ultrasonic acoustic waves with microfluidic systems for studying, manipulating and separating biological samples. This new research area, currently identified as "acoustofluidics", has recently become an extremely active field as testified by the large number of papers published on this topic. The implementation of acoustic waves into

microfluidic systems can be currently accomplished either as surface acoustic waves (SAW) or as bulk acoustic waves in either a standing or travelling form. As discussed in Section 1.3.1, the force applied to a microparticle inside a fluid by an acoustic wave can be described by the combination of two different contributions: the acoustic radiation force and the streaming-induced drag force, which can be generally neglected in case particles larger than 2 μm are considered [67]. Acoustofluidics offers the possibility to manipulate micro-objects in a bio-friendly and contactless manner and it also allows for easy, programmable operation, fast actuation and high throughput. Therefore, acoustofluidics has been successfully applied to several research fields, including for example droplet production [64] and handling [65,66], microparticle sorting [55], separation [57,58], mixing [60] and assembling [62]. A remarkable attention is also dedicated to the interaction of acoustic waves with cells, which has been demonstrated by several published papers about cells' deformation [157], sorting [158], assays [159], manipulation [160–162], compressibility measurements [17,163] and acoustic prefocusing [56,164]. Among these possible applications, an interesting research direction for acoustofluidics is related to the separation and sorting of cells according to their properties [165–167]. In particular, substantial efforts are currently devoted to the realization of acoustofluidic systems enabling the isolation of circulating tumor cells from human blood samples [168–170]. Several groups already demonstrated the possibility offered by acoustofluidics in isolating target cells (or, in general, target microbeads) from a "background" composed of other suspended microparticles. Some analytical studies of particle kinematics in free-flow acoustophoretic systems have already been reported [171,172]. However, to the best of my knowledge, no systematic analysis has been performed so far in order to investigate the impact of different factors on the separation efficiency achievable in acoustofluidic devices. Understanding the impact of both "extrinsic" and "intrinsic" factors is the starting point to design and realize better acoustofluidic devices, as well as to further increase the separation efficiency.

5.1.1 Overview of acoustofluidic separation

In a microfluidic environment, a laminar fluid flow situation is generally encountered and a suspension of microbeads (or cells) simply moves together with the fluid flow. The application of an external acoustic field to the fluid in the microchannel makes the microparticles experience an additional acoustic force. In this theoretical study, a microchannel with a rectangular cross-section will be always assumed, and the only considered acoustophoretic force will be the one produced by a single node acoustic standing wave resonating along the microchannel width. This standing wave can be excited in the microfluidic channel by putting the chip in contact with a piezoelectric transducer driven at the proper microchannel eigenfrequency. By taking advantage of the acoustic

radiation force, it is generally possible to obtain two different separation regimes, as shown in Figure 5.1: stable separation and transient separation.

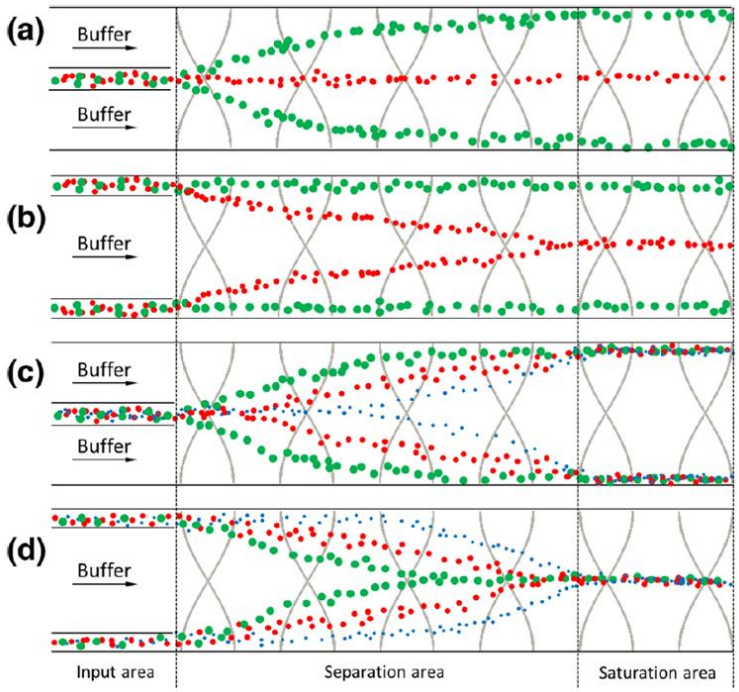

Figure 5.1: Schematic representation of the different acoustic separation regimes of microparticles [154]. *The buffer medium and the sample suspension flow from left to right. The active area of the acoustic field is indicated by the standing acoustic wave patterns. The "separation area" is the portion of the channel where the microparticles effectively change their transverse position and move toward the node or antinode of the acoustic standing wave, while in the "saturation area" the microparticles have already reached their equilibrium position and no significant transverse movement is observed. (a), (b): Stable separation regime. Two sample populations with strongly different properties (indicated by different colors) have different sign of* φ*, resulting in a movement toward the node (*$\varphi > 0$*) or antinode (*$\varphi < 0$*) position. (c), (d): Transient separation regime. The two different sample populations present a small variation of their properties, resulting in a small magnitude difference and same sign of* φ*. Anyway, they show a different response speed to the applied acoustic field. The separation achieved between the different populations in the separation area is not maintained in the saturation area due to the fact that all the microparticles settled to the same node or antinode position.*

The standing wave patterns shown in each panel represent the single node acoustic standing wave resonating along the microchannel width direction. The simplest regime is graphically shown in Figure 5.1 (a), (b). In this situation, a "stable separation" of two sample populations with different properties (represented by two different colors) is achieved: if the sample properties make the two populations have an opposite sign of the acoustic contrast factor φ, then the samples move toward the node or antinode position depending on the sign of φ, making it possible an easy separation and collection of the two different

populations. In the case reported in Figure 5.1 (a), (b), red particles have $\varphi > 0$ and are therefore attracted to the node position, whereas green particles present $\varphi < 0$ and thus move toward the antinode position. Due to the fact that the two sample populations have different equilibrium positions, they begin separating in the "separation area", and then they maintain their transverse separation even after reaching the "saturation area". It must be clarified that the different dot sizes and colors are used just to allow an easy identification of the different population trajectories due to their different properties, but they are not related to any size (or color) difference between the populations. The stable separation regime is ideal in case sample populations with very different properties like very different compressibility or density are considered. However, this is not the case commonly encountered when similar cell samples are considered. For example, even if cancerous cells have a, statistically significant, higher compressibility compared to their normal counterpart [17,163], this difference is relatively small and is not large enough to change the sign of φ. For these considerations and practical issues, the second possible regime of transient separation is commonly considered. As represented in Figure 5.1 (c), (d), sample populations with different properties (indicated by different colors), but characterized by the same sign of φ, move toward the same node or antinode position of the acoustic standing wave, only showing a different velocity. Therefore, in this regime, an initial separation is achieved in the separation area, but after this transient separation condition, all the micro-objects saturate into the same microchannel position once the saturation area is reached. Thus, the only achievable separation in this regime is in the separation area, thanks to the different response speed of the different sample populations. Referring to situations of biological interest, cells usually have $\varphi > 0$ and they move toward the node position. Therefore, in the following study, only the situation shown in Figure 5.1 (d) will be considered. However, it should be noted that the methodology and theoretical analysis proposed in this chapter can be easily adapted to the other situations. Additionally, in this study it will be investigated the challenging situation in which the microparticles to be separated show a relatively small property deviation (between 0 and 20%) from the background objects flowing along the channel, thus focusing the attention on situations in which achieving a good separation efficiency is difficult, as in the cases commonly encountered in the study of biological specimens.

5.1.2 Governing equations

As already discussed in Section 1.3, the acoustic radiation force, resulting from the scattering of acoustic waves by the microparticle, is the time-averaged effect of the acoustic pressure field. One of the main parameters influencing the microbead response to the applied acoustic field is the previously introduced acoustic contrast factor φ, which is given by the following expression:

$$\varphi = \frac{5\rho_p - 2\rho_f}{2\rho_p + \rho_f} - \frac{\beta_p}{\beta_f} \tag{5.1}$$

where ρ_p and ρ_f are the densities of the suspended microparticles and fluid, respectively, and β_p and β_f are the compressibilities of microparticles and fluid, respectively. By considering a 1D acoustic resonance along the y-direction (microchannel width), the analytical expression of the acoustic radiation force F_{ac} acting on the suspended microparticles (microbeads or cells) is given by:

$$F_{ac} = V_p \varphi k_y E_{ac} \sin(2k_y y) = \frac{4}{3}\pi R^3 \varphi k_y E_{ac} \sin(2k_y y) \tag{5.2}$$

where V_p is the volume of a spherical microparticle with radius R, y is the microparticle position along the transverse direction, E_{ac} is the acoustic energy density in the microfluidic channel and k_y is the acoustic wave number, which is equal to $2\pi/\lambda$, with λ being the acoustic wavelength. Considering our situation in which $\lambda = 2w$, with w being the microchannel width, the acoustic wave number can be rewritten as $k_y = \pi/w$. As it is evident from the equation, the sign of φ determines the sign of the acoustic radiation force, and it is therefore responsible for the microparticle movement toward the node or antinode position. Figure 5.2 schematically represents the situation considered in this study: a single node resonant acoustic wave is established along the width of a rectangular microchannel and the acoustic radiation force acts perpendicularly to the flow direction with the resulting transversal movement of microparticles, with a positive value of φ, toward the node position. The transverse movement of microparticles (along the y-direction) is therefore induced by the oscillating pressure field.

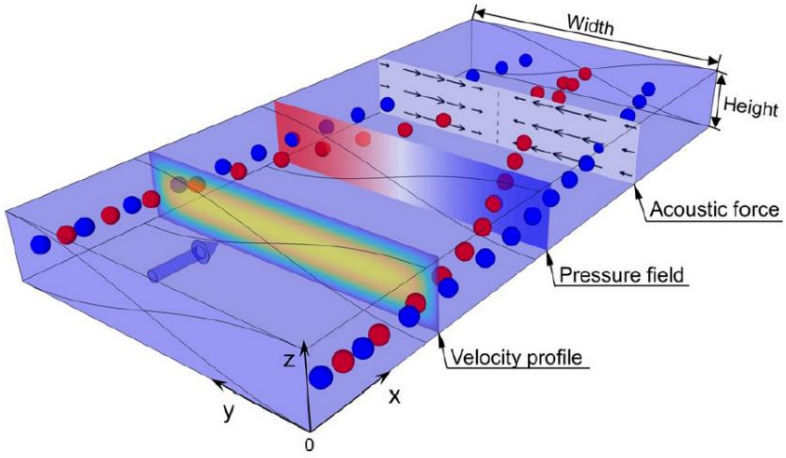

Figure 5.2: Microparticle separation in the dynamic regime considered in this study [154]. *This 3D representation displays that a possible dynamic separation can be achieved considering the flow of two sample populations with different properties (represented by different colors) along a fluid-filled rectangular microfluidic channel with an applied acoustic field. A 1D single node acoustic standing wave along the width direction is considered, as indicated by the pressure field, the acoustic radiation force and the standing wave patterns. The two particle populations both move toward the node position, as they both have* $\varphi > 0$*, but due to the fact that the two populations are characterized by a different response speed, it is possible to design and operate the system to achieve the microparticles separation before they both saturate in the node position.*

The relative motion of the microspheres with respect to the surrounding fluid induces a Stokes drag force F_{drag}, which is given by the usual expression:

$$F_{drag} = 6\pi\eta_f R v_y \tag{5.3}$$

where η_f is the fluid viscosity and v_y is the relative velocity of the microsphere along the y-direction. Due to the fact that in a microfluidic environment the inertial effects can be generally neglected, as given by the fact that the Reynolds number $Re \ll 1$, it is possible to assume that in every instant of the microparticle motion the acoustic radiation force is exactly balanced by the Stokes drag force. Therefore, by imposing $F_{drag} = F_{ac}$, both the transverse speed v_y and transverse position $y(t)$ of the microsphere can be calculated, as given by the following equations:

$$v_y(y) = \frac{2R^2 k_y E_{ac} \varphi}{9\eta_f} \sin(2k_y y) \tag{5.4}$$

$$y(t) = \frac{arctan\left\{\tan\left[k_y y(0)\right] exp\left[\frac{4\varphi\left(k_y R\right)^2 E_{ac}}{9\eta_f} t\right]\right\}}{k_y} \tag{5.5}$$

where $y(0)$ is the microparticle position at a time $t = 0$ (i.e. in the instant of time when the microparticle enters the region where the acoustic field is present). By isolating t from Eq. 5.5 it is possible to calculate the time interval required to move a microparticle from the initial position $y(0)$ to a generic position $y(t)$, as shown by the following equation:

$$t = \frac{9\eta_f}{4\varphi\left(k_y R\right)^2 E_{ac}} ln\left\{\frac{tan\left[k_y y(t)\right]}{tan\left[k_y y(0)\right]}\right\} \tag{5.6}$$

It should be noted that no movement at all could be produced selecting an initial position $y(0) = 0$, which is in any case an unpractical situation as the minimum initial position for a solid microsphere is $y(0) = R$. In an analogous way, due to the tangent function in the equation, an infinite time is required to exactly reach the node position by acoustophoresis (as the numerator would diverge toward infinite), independently from the choice of $y(0)$. For this reason, when the calculation of the "saturation time" for microparticles to move from $y(0)$ to the final node position is required, $y(t) = w/2 \times 0.995$ will be considered as final position. Considering in this study a rectangular microchannel with $w > h$, with h being the microchannel height, the velocity field $v_x(y, z)$ in the microchannel cross-section ($0 < y < w$ and $0 < z < h$) is given by Eq. 5.8 [54]:

$$v_{c,\infty} = \frac{4h^2 \nabla P}{\pi^3 \eta_f} \tag{5.7}$$

$$v_x(y, z) = \sum_{n,odd}^{\infty} \frac{v_{c,\infty}}{n^3} \left[1 - \frac{\cosh\left(n\pi \frac{2y - w}{2h}\right)}{\cosh\left(n\pi \frac{w}{2h}\right)}\right] \sin\left(n\pi \frac{z}{h}\right) \tag{5.8}$$

where ∇P is the pressure gradient. It can be noted that, under the simplifying hypothesis that $w \gg h$ (not assumed in the rest of the chapter unless explicitly specified), the term $v_{c,\infty}$ given by Eq. 5.7 is an approximation of the fluid velocity at the microchannel center (with a ~3% overestimation). Finally, the trajectories of the microspheres dispersed in the microfluidic channel under the action of the fluid flow and acoustic field can be calculated by Eq. 5.8 and Eq. 5.4 together. It must be noted that the acoustic radiation force and the resulting microbead transverse movement occur along the microfluidic channel width

direction (y), which is perpendicular to the direction of the fluid flow (x-direction). Consequently, the distance travelled by the microparticles along the flow direction, $x(t)$, can be simply determined by integrating in time $v_x(y,z)$, assuming that $z = h/2$, i.e. all the microparticles remain at half of the microchannel height while flowing. Until Section 5.4.3, in which a realistic 3D system configuration will be considered, for the rest of the chapter the microparticles position along the z-direction will be always considered at half of the channel height, $z = h/2$, with no vertical spreading in the initial particles position. Moreover, even if in the whole analysis the effect of gravity is neglected, assuming that no significant movement along the z-direction occurs during the time that the microspheres flow along the microfluidic channel, it must be mentioned that gravity can be helpfully exploited to obtain a sample separation in the vertical direction [173].

5.2 Definition of the simulation parameters

Acoustofluidic devices are commonly employed to sort and separate cells or other biological samples. However, as biological specimens are generally characterized by a significant spread of their mechanical properties, in the following part of the chapter polystyrene microbeads will be considered as "dispersed microspheres" and water as flowing medium in which the microbeads are dispersed. It is important to notice that this choice does not affect the validity of the proposed theoretical analysis, which could be extended even to cells dispersed in culture medium, provided that their mechanical properties are statistically known. The physical parameters of the simulated acoustofluidic systems considered in Section 5.3 are reported in Table 5.1.

Table 5.1: Simulation parameters used in the acoustofluidic systems considered in Section 5.3.

Water			
Density	ρ_w	998	kg m^{-3}
Compressibility	β_w	4.48×10^{-10}	Pa^{-1}
Viscosity	η_w	8.94×10^{-4}	Pa s
Sound speed	v_w	1483	m s^{-1}
Polystyrene bead			
Density	ρ_p	1050	kg m^{-3}
Compressibility	β_p	2.49×10^{-10}	Pa^{-1}
Bead diameter	D_p	7.5	μm
Acoustic excitation			
Acoustic half wavelength	$\lambda/2$	600, 500, 400	μm
Channel width	w	600, 500, 400	μm
Channel height	h	100	μm
Pressure gradient	∇P	20	Pa m^{-1}
Acoustic energy density	E_{ac}	1.0	J m^{-3}

Because of the symmetry of the considered acoustofluidic configuration, and of the equations governing the microbeads motion, the trajectories travelled by two identical microparticles input in symmetric positions of the microfluidic channel will remain symmetric with respect to the channel central axis during the flow, as it can be graphically seen in Figure 5.2. Taking advantage of this symmetry, in the following part of the chapter, the theoretical analysis and numerical simulations will be therefore limited to only half of the channel cross-section without any loss of generality.

In real situations, the microparticles in input to the microchannel are generally characterized by a certain distribution of their initial position, which can be wider or narrower depending on the geometry of the considered configuration (e.g. the dimension of the input microchannel) and which is even related to possibly employed prefocusing strategies (e.g. acoustic prefocusing and inertial prefocusing). In order to properly consider this effect, in the here-presented study the initial position of the incoming microparticles is defined by a certain range, which will be indicated as "initial position range" (IPR). This allows better mimicking real situations encountered in acoustic separation experiments. Specifically, in the following analysis the center of the IPR will be indicated as y_0 and the half width of the IPR along the channel width as Δy_0, assuming therefore that all the microparticles enter the microchannel from an initial position included in the range $[y_0 - \Delta y_0, y_0 + \Delta y_0]$. In a similar way for the channel height, the sample starting position will be indicated as z_0 and the half width of the IPR as Δz_0. As already anticipated, until Section 5.4.3, $z_0 = h/2$ and $\Delta z_0 = 0$ will be assumed. In the following, as a consequence of the introduction of the IPR concept, acoustophoretic trajectories will not be considered as "lines", but as "areas", as shown for example in Figure 5.3 (a). The microbeads in input to the microfluidic channel from a position within the IPR will move along the channel remaining inside the trajectory area. From the analysis of the trajectory areas, two different parameters can be introduced: the "bandwidth" (BW) and the "displacement" (D), which are shown, for the considered trajectories, in Figure 5.3 (b), (c), respectively. The BW parameter can be defined as the transverse width of the trajectory area at each position, while the D parameter is the average transverse distance (along the y-direction) travelled from the average initial position. As both quantities depend on the x-position along the flowing direction, they should be correctly written as $BW(x)$ and $D(x)$. By indicating the average position in the y-direction as $\langle y(x) \rangle$, the expressions of $BW(x)$ and $D(x)$ in terms of the IPR center and width can be written as:

$$D(x) = \langle y(x) \rangle - y_0 \tag{5.9}$$

$$BW(0) = 2\Delta y_0 \tag{5.10}$$

Figure 5.3 (b) shows the evolution of $BW(x)$ as a function of the flow distance x: it starts from a value equal to $2\Delta y_0$, it increases upon reaching a maximum and then it finally decreases toward zero once the trajectory tends to saturate at the node position. An explanation for the particular shape of the $BW(x)$ curve can be given by observing that the $BW(x)$ parameter can be thought as the evolution of the y-displacement between two microparticles ideally injected, in the same instant, on the "upper" and "lower" borders of the IPR. As the transverse velocity of both microparticles is described by Eq. 5.4, the trajectory lines of these two "extreme microbeads" can be perfectly overlapped by shifting one trajectory line horizontally. This horizontal shift, together with the "S-shape" of the trajectory lines due to the velocity profiles (see Eq. 5.4 and Eq. 5.8), is the motivation for the initial increase and subsequent decrease observed in the $BW(x)$ parameter. The evolution of the $D(x)$ parameter is shown in Figure 5.3 (c): it increases monotonically from zero to a plateau value that is reached in correspondence to the trajectory saturation to the node position.

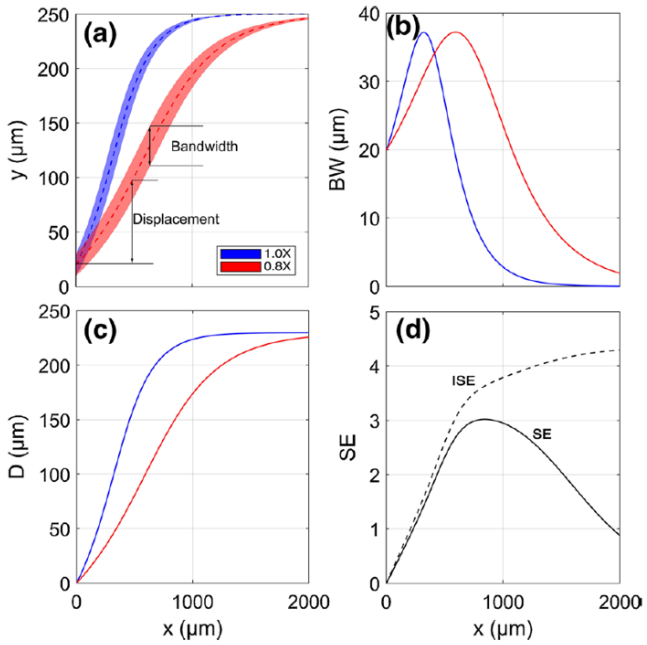

Figure 5.3: Definition of the simulation parameters employed in the following analysis [154]. *A microchannel having a width* $w = 500\ \mu m$ *is considered, so that the microchannel wall is located at* $y = 0$ *and the channel central axis is at* $y = 250\ \mu m$. *(a) Considering a microparticles' IPR with* $y_0 = 20\ \mu m$ *and* $\Delta y_0 = 10\ \mu m$, *the trajectory areas calculated for two different microbead populations having different densities are shown. Blue microbeads are characterized by 100% polystyrene bead density while red microbeads have 80% polystyrene density. The dashed colored lines represent the average position in each* x*-coordinate. (b) The* $BW(x)$ *parameter is shown, which is defined as the width in the* y*-direction of the trajectory area. (c) The* $D(x)$ *parameter is shown, which is defined as the difference between the average trajectory area in each* x*-position and the center of the IPR. (d) Spatial evolution of the* $ISE(x)$ *(dashed line) and* $SE(x)$ *(solid line) parameters, which can be used to quantify the separation efficiency of the considered acoustofluidic system.*

The relative displacement $RD(x)$ between the two particle populations can be then calculated by considering the difference between the two displacement curves $D_1(x)$ and $D_2(x)$, where the subscripts 1 and 2 are used to refer to the two considered particle populations:

$$RD(x) = |D_1(x) - D_2(x)| \tag{5.11}$$

From the above-presented quantities, it is possible to introduce an "ideal separation efficiency" (ISE) parameter, which can be used to estimate the achievable separation between the two particle populations:

$$ISE(x) = 2\frac{RD(x)}{BW_1(x) + BW_2(x)} \tag{5.12}$$

Adopting this definition, $ISE < 1$ indicates that the trajectory areas are partially overlapped, whereas $ISE > 1$ indicates that the two trajectory areas are completely separated. The dashed line in Figure 5.3 (d) shows the $ISE(x)$ evolution during the flow. It must be observed that as both $BW_{1,2}(x)$ parameters tend to zero in correspondence to the microbeads saturation to the node position, the large value assumed by the ISE parameter does not correspond to a real possibility of achieving an efficient microbeads separation, as the microparticle radius is significantly larger than the calculated bandwidths. For this consideration, in the following a more realistic "separation efficiency" (SE) parameter is introduced, in which the impact of the microparticle radius R is included:

$$SE(x) = 2\frac{RD(x)}{BW_1(x) + BW_2(x) + 2R} \tag{5.13}$$

According to this new definition, $SE > 1$ when the two populations are completely separated by a distance larger than one microparticle radius. The solid line in Figure 5.3 (d) shows the evolution of the $SE(x)$ parameter. As it can be seen, the best separation (i.e. the highest SE value) is reached during the transition phase and not when the microbeads are already saturating to the node position.

5.3 Impact of acoustofluidic system design and of sample properties

As it is evident from the previous equations, the acoustophoretic trajectory of a microbead subjected to an external acoustic field is determined by many parameters,

which affect the final separation efficiency. In the following analysis and simulations, the parameters of water (viscosity, density and compressibility) will be considered as reference values for the suspension medium and will be kept fixed, while polystyrene parameters will be considered for the dispersed microparticles and the impact of their variation (in a range [0-20] %) on the resulting separation efficiency will be investigated. In order to give a clear organization to the discussion, all the involved parameters will be divided into two categories: extrinsic and intrinsic factors. Extrinsic factors will be initially considered and then a critical system configuration will be selected to study the role of intrinsic factors.

5.3.1 Extrinsic factors: chip design and operation

All the elements related to the acoustofluidic system design and operation were considered in the group of extrinsic factors, i.e. the microfluidic channel dimensions, the acoustic energy density and the injection position of the microbeads. All these parameters can have a significant impact on the final separation efficiency and therefore should be carefully optimized. The first analyzed parameter is the channel width w. As the considered configuration is the one corresponding to an acoustic standing wave with a single node along the microchannel width, as represented in Figure 5.2, the acoustic wavelength λ is given by $\lambda = 2w$ and the wave frequency can be easily calculated as $f = \nu/\lambda$, with ν being the speed of sound in water. Figure 5.4 shows the acoustic separation results of numerical simulations performed considering microbeads with different compressibilities (80%, 100% and 120% of the polystyrene compressibility) for three different microchannel widths (400, 500 and 600 µm). In all the simulations, the same IPR ($y_0 = 20\ \mu m$ and $\Delta y_0 = 10\ \mu m$) and the same acoustic energy density ($E_{ac} = 1\ J/m^3$) are considered, with all the other parameters defined equal to the values listed in Table 5.1.

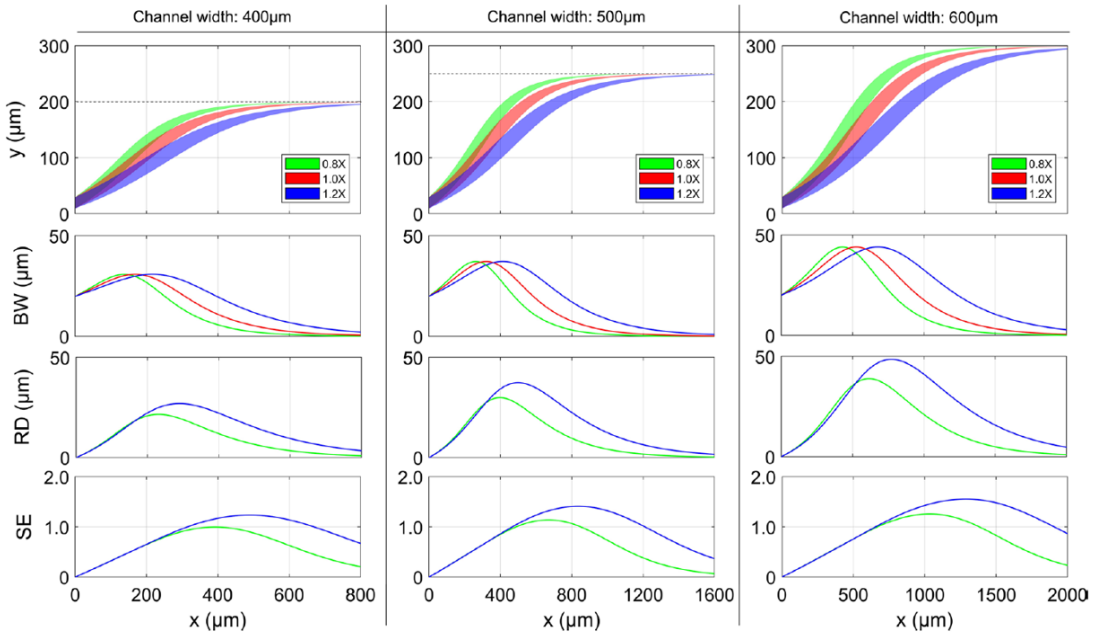

Figure 5.4: Acoustic separation of polystyrene microbead populations with different compressibilities considering different channel widths: 400, 500 and 600 μm [154]. *Compressibility values corresponding to 80, 100 and 120% of polystyrene standard compressibility are considered, indicated by 0.8×, 1.0× and 1.2× in the figure legend. The dashed line in the first row represents the position corresponding to the node of the standing acoustic wave. The IPR is defined by* $y_0 = 20\ \mu m$ *and* $\Delta y_0 = 10\ \mu m$ *for all the three considered channel widths. All the other simulation parameters are reported in Table 5.1. For each channel width, the trajectory area and its corresponding* $BW(x)$ *are shown in the first and second row, respectively. The third and fourth rows show* $RD(x)$ *and* $SE(x)$ *with respect to the 1.0× population.*

The first row of Figure 5.4 shows the trajectory areas calculated for each compressibility, while in the second row the corresponding $BW(x)$ is displayed. To quantify the impact of the different channel widths on the separation efficiency, the third and fourth rows report the calculated $RD(x)$ and $SE(x)$, respectively. By observing the second row in Figure 5.4, the $BW(x)$ parameter shows the same behavior as the one observed in Figure 5.3 (b), but it can even be noticed that the maximum of $BW(x)$ (BW_{MAX}) does not depend on the microparticle compressibility. The motivation can be found in the fact that the compressibility variation only modifies the φ value appearing in Eq. 5.5. Consequently, this variation just introduces a timescale factor between the different microparticle populations, explaining the fact that BW_{MAX} is located at different x-positions along the channel for the different populations, but it does not affect the value of BW_{MAX}. The third row of Figure 5.4 reports the $RD(x)$ parameter calculated between the 0.8× and 1.0× populations (green line) and that between the 1.0× and 1.2× populations (blue line). The observed $RD(x)$ evolution is similar to the one of $BW(x)$, but it must be pointed out that BW is a "single population" parameter, as it can be calculated considering a set of identical

microbeads, whereas RD is a "two-populations" parameter, as it refers to the distinct behavior of two different sets of microbeads input to the same microfluidic channel. In order to achieve a high separation efficiency, a very small BW together with a large RD are desirable, so that the different particle populations can be efficiently collected at different outputs. However, as it is evident from the second and third rows of Figure 5.4, this mutual condition is difficult to be satisfied, and in order to determine the best sample collection position it can be useful to calculate the maximum of the SE parameter. By observing the evolution of $SE(x)$, it can be noted that the highest value of SE is reached when RD is already decreasing, thanks to a trade-off between a small BW and a value of RD still sufficiently large. By comparing the results obtained with the three different microchannel widths, it is evident that the use of wider channels results in an increase of both the BW_{MAX} and RD curves, but, overall, the maximum SE (SE_{MAX}) achievable by each configuration increases when wider channels are considered. Considering that the largest microchannel width of 600 µm emerges as the best configuration among the reported ones, yielding the highest SE_{MAX}, we decided to continue the analysis considering the 500 µm-wide channel. The motivation lies in the fact that, in this way, it is possible to study the impact of the other parameters on the separation efficiency considering a "non-optimal" scenario.

Another design parameter influencing the microparticle trajectory, and hence the resulting separation efficiency, is the IPR. While it is evident that a narrower IPR width (equal to $2\Delta y_0$) allows achieving a higher separation efficiency, as it yields a BW reduction, some non-intuitive results can be derived studying the impact of y_0 (the IPR central position) on SE_{MAX}. The IPR, which is experimentally determined by the inlet geometry, is generally located very close to the channel border in order to have a larger distance between the injection point and the saturation node, and, obviously, the IPR strictly depends on the width of the inlet channel. In order to discuss the role of the IPR, Figure 5.5 shows three different trajectory areas, together with the corresponding $BW(x)$ and $D(x)$, calculated assuming three different IPR central positions y_0: 20, 40 and 60 µm. The acoustophoretic trajectories are calculated considering polystyrene microbeads (see data in Table 5.1). As it can be observed, even if $\Delta y_0 = 10\ \mu m$ is the same for all three cases, the three areas become smaller as the IPR center gets closer to the microchannel central axis. By observing the $BW(x)$ evolution, it can be seen that the BW parameter significantly increases in case the IPR is located in the proximity of the channel border (e.g., $y_0 = 20\mu m$), whereas this behavior is almost non-existent when the IPR gets closer to the channel central axis (e.g., $y_0 = 60\mu m$). The relation between BW and y_0 can be better explained observing that when the IPR is moved toward "higher velocity" positions (i.e. from the channel border toward $w/4$, see Eq. 5.4), the scaling factor required to overlap the top and bottom trajectory lines reduces significantly. Moreover, if $w/4 < y_0 < w/2$ the $BW(x)$ parameter will decrease monotonically, as in that space interval even the

transverse velocity decreases while approaching the node position. By observing the $D(x)$ evolution, it can be seen that when y_0 is increased, the acoustic field-induced motion is initially faster, but the final displacement is smaller.

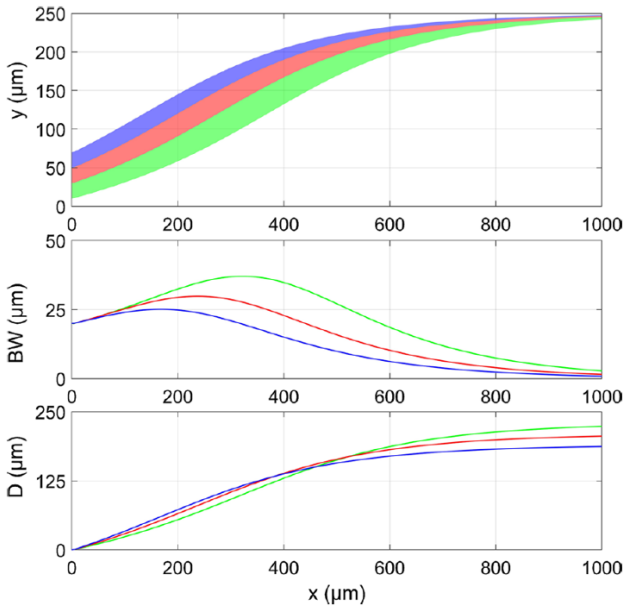

Figure 5.5: Simulation of acoustophoretic trajectories of polystyrene microparticles under the assumption of three different IPR central positions y_0: 20 µm (green), 40 µm (red), 60 µm (blue) [154]*. For all the considered cases $\Delta y_0 = 10$ µm. The trajectory areas are shown together with the corresponding $BW(x)$ and $D(x)$. Channel width $w = 500$ µm, $E_{ac} = 1\,J/m^3$ and all the other parameters are reported in Table 5.1.*

As both $BW(x)$ and $D(x)$ show a certain dependence on y_0, even the SE parameter will be obviously influenced by the IPR center. Therefore, the impact of y_0 and Δy_0 on the BW_{MAX} and SE_{MAX} parameters was investigated. For the simulations, the same three populations considered in Figure 5.4 and a fixed channel width $w = 500\,\mu m$ were assumed. The results of the numerical simulations are shown in Figure 5.6: panel (a) displays the BW_{MAX} and SE_{MAX} parameters as a function of y_0 (for a fixed $\Delta y_0 = 10\,\mu m$), while panel (b) reports their evolution as a function of Δy_0, assuming to have the IPR lower bound (defined as $y_0 - \Delta y_0$) located at 10 µm from the channel border. From Figure 5.6 (a) it can be seen that by slightly changing the value of y_0, from 20 to 50 µm, BW_{MAX} strongly decreases, whereas a small increase of SE_{MAX} can be observed. Specifically, SE_{MAX} increases from 1.42 to 1.48, when the separation between the 1.0× and 1.2× populations is considered, and from 1.15 to 1.19 considering the separation between the 0.8× and 1.0× populations. The BW_{MAX} and SE_{MAX} dependence on Δy_0 is shown in Figure 5.6 (b): for an increase of Δy_0, BW_{MAX} increases almost linearly, while the SE_{MAX} parameter decreases due to the wider areas overlap. The here-presented analysis just gives an idea of the SE-

dependence on the IPR. As this topic requires a more extensive discussion, Section 5.4 will be completely dedicated to the study and optimization of the sample launch position to achieve the highest SE for the considered configuration.

The last extrinsic parameter to be analyzed is the acoustic energy density E_{ac}, which depends on the driving voltage externally applied to the piezoelectric transducer. By observing Eq. 5.4, it can be noticed that the microparticle transverse velocity is directly proportional to this parameter. Therefore, it is possible to conclude that E_{ac} directly affects the particle velocity, but not the resulting SE. By changing the driving voltage applied to the piezoelectric transducer, E_{ac} can be properly selected according to the length of the active separation area of the microchannel and the flowing velocity, which depends on the pressure gradient, to optimize the collection efficiency.

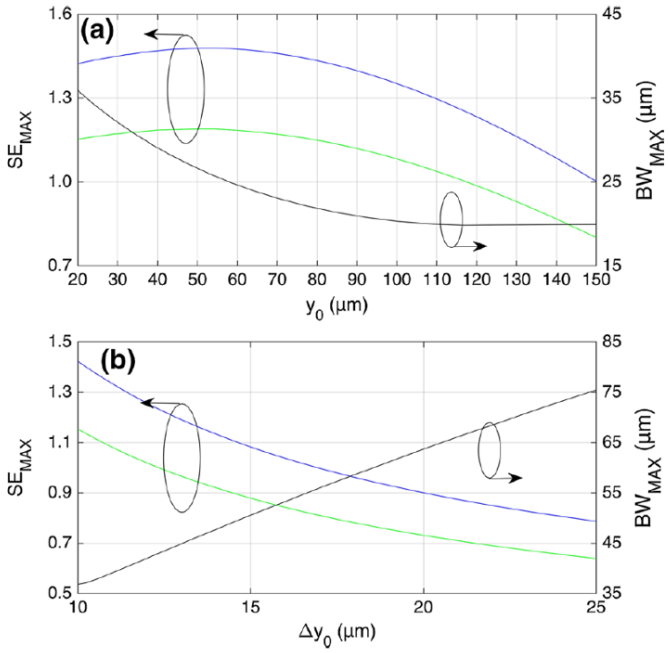

Figure 5.6: Dependence of SE_{MAX} (blue and green lines) and BW_{MAX} (black lines) on the IPR [154]. *Microbeads with different compressibility are considered, as in the case reported in Figure 5.4. (a) Parameters dependence on y_0, by considering a fixed $\Delta y_0 = 10\ \mu m$. (b) Parameters dependence on Δy_0, by considering the lower IPR boundary fixed at 10 µm. Channel width $w = 500\ \mu m$, $E_{ac} = 1\ J/m^3$ and all the other parameters are reported in Table 5.1.*

5.3.2 Intrinsic factors: sample properties

After having studied the impact of the parameters related to the acoustofluidic system design and operation on the acoustic SE, the effect of the sample's intrinsic parameters (i.e. density, compressibility and radius) was investigated. These three factors are all present in the exponential term in Eq. 5.5, but they give different contributions: the density and compressibility are included in the acoustic contrast factor φ, while the radius

squared appears as a time multiplying factor. Figure 5.7 (a) reports the impact of density and compressibility on the acoustic contrast factor φ. Assuming a 20% variation with respect to the nominal polystyrene values, i.e. a range [80-120]% of the standard polystyrene parameters, it can be seen that the value of φ reduces from 0.6 to almost 0.4 when the compressibility is increased, whereas it increases from 0.27 to 0.66 by increasing the density. From this simple calculation, it results clear that the density variation has a stronger impact on the value of φ with respect to the microbead compressibility, considering the same variation range. This implies that microparticles separation based on density would give a higher separation efficiency than compressibility-based acoustic separation. Another method to estimate the impact of the intrinsic parameters on SE is to study how the "response speed" is influenced by the microparticle properties. Specifically, it is possible to introduce a "saturation time" t_{sat}, which can be defined as the time required to move a microparticle from the initial position to $y = 0.995 \times w/2$. Moreover, using this new parameter it is even possible to analyze the impact of the microparticle diameter, which obviously could not be studied by calculating the φ factor. Figure 5.7 (b) shows the evolution of the saturation time t_{sat} as a function of the intrinsic parameters variation in the same variation range [80-120]%. The results of the numerical simulations show once again that the effect of density variation on the microparticles movement is more pronounced than that of compressibility variation. In addition, it can be noticed that the effect of the microparticle diameter variation on t_{sat} is similar to the one resulting from the variation of the microparticle density.

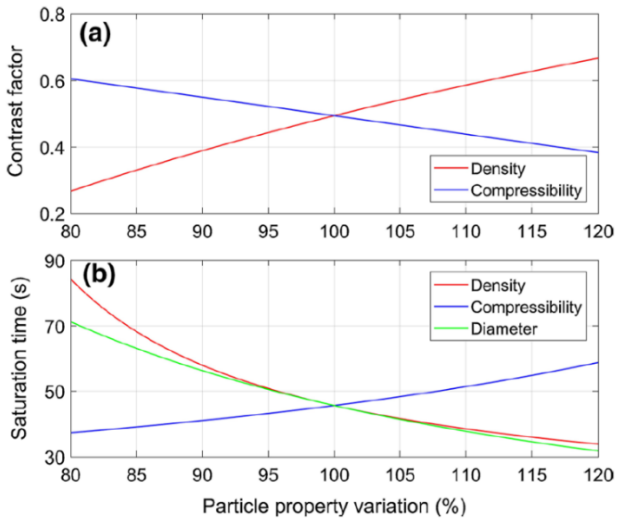

Figure 5.7: Sample properties effect on the acoustic contrast factor (a) and on the saturation time (b), calculated considering $y_0 = 20\ \mu m$ as the initial particle position [154]. *The different curves refer, as indicated by the legend, to variation of different parameters: only one parameter is changed at a time, while the other two are set at the standard polystyrene value (100%). Channel width $w = 500\ \mu m$, $E_{ac} = 1\ J/m^3$ and all the other parameters are reported in Table 5.1.*

In a similar way to the analysis presented for the extrinsic parameters, the study on the intrinsic parameters was extended by using the IPR concept and by investigating the achievable SE. For each microbead intrinsic parameter (compressibility, density and diameter), three different values (80, 100 and 120 %) of the polystyrene nominal properties were considered and the results of the numerical simulations are shown in Figure 5.8. It must be pointed out that the 1.0× value (red color) indicates that there is no variation of the sample properties and, therefore, the trajectory areas are exactly the same in the first row as well as the $BW(x)$ curves reported in the second row. Observing the first row of Figure 5.8 it is evident that the acoustic separation based on different values of the sample compressibility is the most challenging, due to the high trajectory areas overlap, as it could be expected from the previously reported analysis. From the $BW(x)$ curves, reported in the second row, it can be observed that the BW_{MAX} value does not depend on any of the intrinsic factors, but it is only related to the extrinsic ones. Conversely, the positions in which BW_{MAX} is observed are related to the different response speeds associated with different sample property variations. Finally, by analyzing the $SE(x)$ curves (see the third row of Figure 5.8), it can be observed that the SE_{MAX} value is the smallest in case compressibility variations are considered, further confirming the above reported discussion.

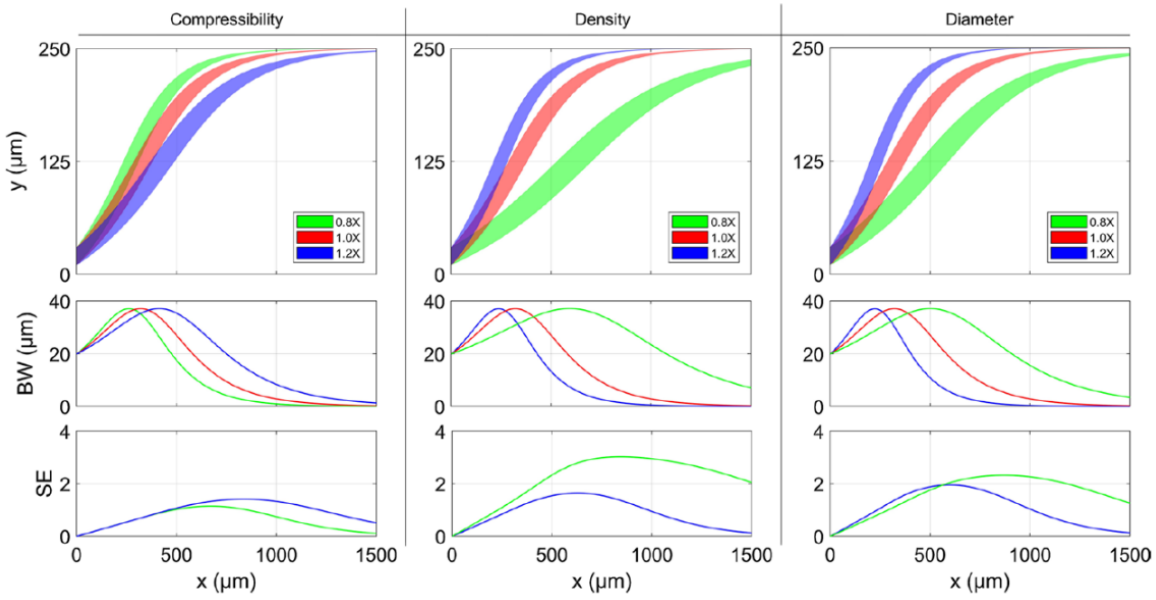

Figure 5.8: Impact of different sample's properties on the acoustofluidic separation [154]*. For each microbead intrinsic parameter (compressibility, density and diameter), three different values (80, 100 and 120 %) of the nominal polystyrene properties are considered, indicated in the figure legend by 0.8×, 1.0× and 1.2×. The channel width w is set equal to 500 μm and the IPR is defined by* $y_0 = 20\ \mu m$ *and* $\Delta y_0 = 10\ \mu m$ *for all the considered cases.* $E_{ac} = 1\ J/m^3$ *and all the other parameters are reported in Table 5.1. For each intrinsic microbead parameter, the trajectory areas are shown in the first row, and the corresponding* $BW(x)$ *and* $SE(x)$ *are displayed in the second and third row, respectively.*

5.4 Study and optimization of the sample launch-position

As it has been discussed in the previous section, the microparticles launch-position into the active area where the acoustophoretic force is present plays a critical role on the achievable acoustic separation. Even if it is commonly recognized that microparticles prefocusing and launch-position optimization have a key role on the acoustofluidic devices performance, a detailed discussion on how these two factors influence the device efficiency is still missing.

The goal of this section is to study how the launch position of the sample inside the microfluidic channel affects the separation efficiency, and to show how the best launch position depends on several factors: the aspect ratio of the microfluidic channel, the cross-section occupied by the microparticles distribution at the channel input and the size of the microparticles to be separated. This analysis will be carried out following different steps. A theoretical study will be initially performed assuming the simplistic hypothesis of a uniform flow speed in the microfluidic channel (1D-systems). Then the results of numerical simulations on more realistic configurations (2D- and 3D-systems) will be presented. For the theoretical analysis and numerical simulations, a rectangular microchannel with a cross-sectional area of 0.09 mm^2 and with variable aspect ratio (defined as the ratio between the microchannel width and height, w/h) will be considered, where a single node acoustic standing wave resonating along the microchannel width is established. In real experiments, the microparticles injection-area yields a certain statistical distribution of the microparticles initial position (y_0, z_0). Therefore, the impact of the initial position uncertainty (Δy_0, Δz_0) on the achievable SE between two microbead populations characterized by slightly different properties will be investigated. As already anticipated, $z_0 = h/2$ and $\Delta z_0 = 0$ will be assumed until Section 5.4.3, in which a certain vertical spreading will be considered in order to mimic common situations experienced in real experiments.

5.4.1 Theoretical analysis: uniform flow speed in 1D-systems

Observing Eq. 5.8 it can be initially noted that if the distance from the channel border is greater than twice the channel's height (i.e. $y > 2h$), the ratio between the two hyperbolic cosine functions tends to zero. Consequently, in this condition the fluid velocity through the microchannel cross-section is independent on the y-coordinate. Considering a microfluidic channel characterized by a large aspect ratio (i.e. $w \gg h$), the region where the flow velocity depends on the y-coordinate ($y < 2h$) represents a negligible portion of the channel cross-section and it is therefore possible to assume that the microparticles motion along the x-direction is independent on the position along the y-direction. As a consequence, the microparticles separation solely depends on Eq. 5.5 and it is possible to

consider this configuration as a 1D-system. In order to simplify the writing of Eq. 5.5, but without losing important dependences, the following factors can be defined:

$$A = \frac{4\varphi\left(k_y R\right)^2 E_{ac}}{9\eta_f} \qquad k = k_y \tag{5.14}$$

According to these new definitions, Eq. 5.5 can be rewritten as:

$$y(t) = k^{-1} arctan\{\tan[k y_0] exp[At]\} \tag{5.15}$$

This compact expression was employed to develop an analytical characterization of the simplified 1D-system, which, although an oversimplification, allows deriving useful insights into the effect of different factors on SE. Adopting this notation, a change in the microbead properties is expressed by a change of the A parameter, and it is therefore possible to define an average A and a deviation ΔA. In order to determine the SE dependence on the y_0 and A factors, two distinct microparticle populations (a "fast" one, F, and a "slow" one, S) can be considered and for each of them three different "injection points" can be selected: the center of the injection area (C), the border of the injection area closer to the channel wall (W) and the border closer to the node of the acoustic standing wave (N). In this way, six equations similar to Eq. 5.15 can be written, in which the parameter A is modified in $A \pm \Delta A$ to include the effect of the "fast" and "slow" populations, and the terms y_0, $y_0 - \Delta y_0$ and $y_0 + \Delta y_0$ are used to indicate the C, W and N injection positions, respectively (see inlet of Figure 5.9):

$$\begin{aligned}
y_{F,C}(t) &= k^{-1}\{\tan[k y_0] exp[(A + \Delta A)t]\} \\
y_{F,N}(t) &= k^{-1}\{\tan[k(y_0 + \Delta y_0)] exp[(A + \Delta A)t]\} \\
y_{F,W}(t) &= k^{-1}\{\tan[k(y_0 - \Delta y_0)] exp[(A + \Delta A)t]\} \\
y_{S,C}(t) &= k^{-1}\{\tan[k y_0] exp[(A - \Delta A)t]\} \\
y_{S,N}(t) &= k^{-1}\{\tan[k(y_0 + \Delta y_0)] exp[(A - \Delta A)t]\} \\
y_{S,W}(t) &= k^{-1}\{\tan[k(y_0 - \Delta y_0)] exp[(A - \Delta A)t]\}
\end{aligned} \tag{5.16}$$

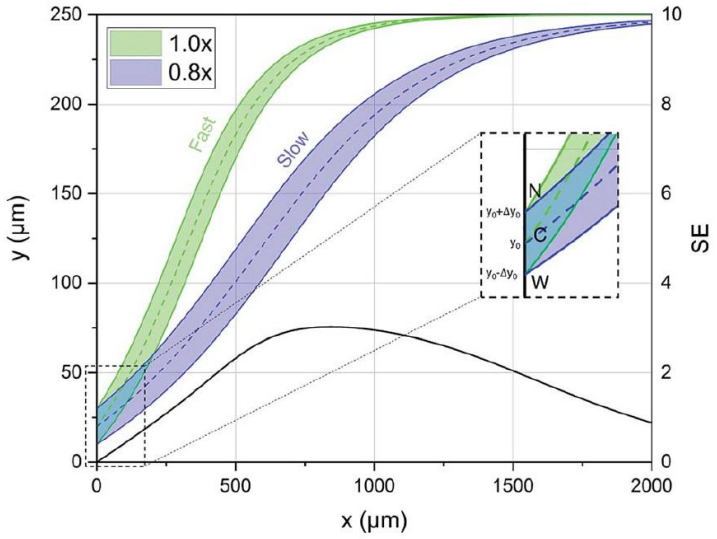

Figure 5.9: Left scale: transverse position along the microchannel width direction y of two microparticle populations with different properties (80% and 100% of the acoustic contrast factor of polystyrene microbeads in water). The microparticles flow along the x-direction. The inset displays a zoomed-in view of the injection area ("C" indicates the center of the injection region, "W" indicates the border of the injection region closer to the microfluidic channel wall and "N" indicates the border of the injection region closer to the node of the acoustic standing wave). Right scale: the resulting separation efficiency as a function of the flowing distance x [155].

Using the previous equations, the SE parameter (see Eq. 5.13), can be rewritten as:

$$SE = \frac{2 \cdot (y_{F,C} - y_{S,C})}{2R + [(y_{F,N} - y_{F,W}) + (y_{S,N} - y_{S,W})]} \tag{5.17}$$

If the differences appearing in Eq. 5.17 are approximated with the corresponding 1st order differential terms, the separation efficiency can be rewritten as:

$$SE = \frac{2\Delta A \frac{dy}{dA}}{R + 2\Delta y_0 \frac{dy}{dy_0}} \tag{5.18}$$

Moreover, it is possible to derive a more useful form of Eq. 5.18 by calculating the two derivatives so as to write an explicit expression for the SE evolution as a function of time, or of flow-distance, as a uniform flow velocity in the microchannel was assumed.

If we then set $\Delta A = \Delta A_r \times A$, where ΔA_r indicates the relative variation of the considered A parameter, after some substitutions SE can be written as:

$$SE(t) = \frac{\Delta A_r}{kR} \frac{At \tan(ky_0) e^{At}}{\left[\frac{1}{2} + \frac{\Delta y_0}{R} e^{At}\right] + \left[\frac{1}{2} e^{2At} + \frac{\Delta y_0}{R} e^{At}\right] \tan^2(ky_0)} \tag{5.19}$$

In the following the values giving the best performance will be indicated with an asterisk (*): y_0^* and t^* are the launch-position and time-instant yielding the maximum separation efficiency (SE^*) obtainable between two microparticle populations. By analyzing Eq. 5.19 some non-trivial considerations about y_0^*, t^* and SE^* can be derived:

i. The role of ΔA_r: according to the given hypothesis, $SE(t)$ (and hence SE^*) is directly proportional to ΔA_r, but ΔA_r has no impact on the y_0 value maximizing SE. This, therefore, means that the optimal injection position y_0^* is independent on how large the sample property variations are.

ii. The maximum separation-instant (t^*): the time-instant yielding the maximum SE cannot be explicitly derived as the resulting equation is transcendental. Nevertheless, it can be noted that the time t always appears in the term At. This has as a result that the maximum separation-instant t^* is inversely proportional to A, i.e. the term At^* is independent on A. It is therefore useful to further rewrite Eq. 5.19 in a more compact form thanks to the definition of the following quantities:

$$\begin{aligned} E &= At^* e^{At^*} \\ F &= \left[\frac{1}{2} + \frac{\Delta y_0}{R} e^{At^*}\right] \\ G &= \left[\frac{1}{2} e^{2At^*} + \frac{\Delta y_0}{R} e^{At^*}\right] \end{aligned} \tag{5.20}$$

The SE value reached at t^* can be calculated according to the following equation, which has two important features: E is a constant while both F and G depend only on the ratio $\Delta y_0/R$:

$$SE(t^*) = \frac{\Delta A_r}{kR} \frac{E \tan(ky_0)}{F + G \tan^2(ky_0)} \tag{5.21}$$

iii. The ratio $\Delta y_0/R$: considering the previous discussion, it can be observed that if both Δy_0 and R are multiplied by the same factor, the optimal injection position y_0^* does not change. Nevertheless, it must be pointed out that even if we keep the ratio

$\Delta y_0/R$ constant, a change in the value of R influences both the value of t^* and that of $SE(t^*)$ due to the fact that they are proportional to R^{-2} and R^{-1}, respectively.

iv. The y_0^* value: in the here-discussed 1D-situation y_0^* depends only on the value of $\Delta y_0/R$. Figure 5.10 shows the ideal injection position normalized to the channel width, y_0^*/w, as a function of the ratio $\Delta y_0/R$. It is interesting to observe that the ideal injection position is close to the channel wall when the value of $\Delta y_0/R$ is almost zero, it rapidly grows when $\Delta y_0/R$ increases from 0 to 1 (increasing from 0% to 12% of w) and finally it almost saturates around 20% of w when $\Delta y_0/R$ becomes much larger than 1.

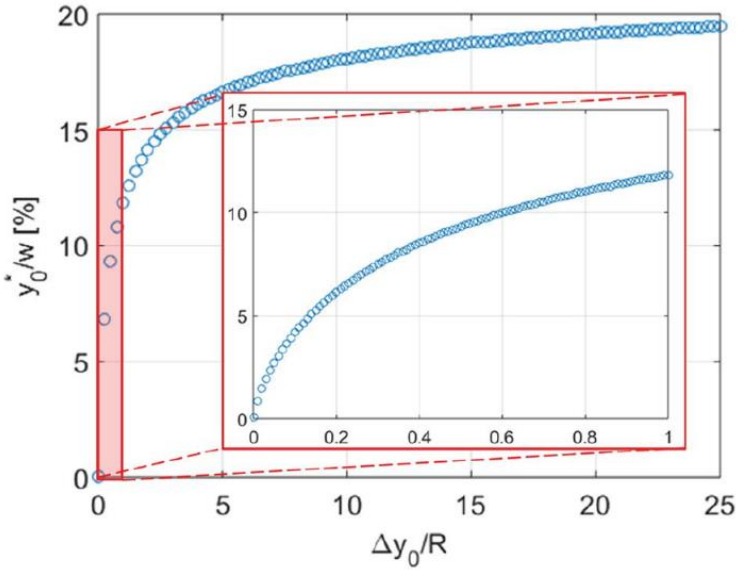

Figure 5.10: Best sample injection-position y_0^*, expressed as a percentage of the microfluidic channel width w, as a function of the ratio $\Delta y_0/R$ [155]*. The inset displays a zoomed-in view of the low-$\Delta y_0/R$ region ($\Delta y_0/R \leq 1$). y_0^* shows a rapid growth in the initial part and then it almost saturates around 20% of the channel width w when $\Delta y_0/R \geq 5$.*

After the analysis of the 1D-system it is interesting to study, by means of numerical simulations, how the system properties are affected by moving to 2D- and 3D-systems, in order to find out if the above considerations are still valid.

5.4.2 Numerical simulations: 2D-systems approximation

The comparison with real acoustic separation experiments, by means of numerical simulations, is performed in a two-step analysis. The first step, which is treated in this section, consists in the introduction of a non-uniform flow speed profile across the channel width (y-direction), with the comparison of the results obtained for different aspect ratios (w/h) of the microchannel cross-section. In this case, the analysis of the results derived at

large aspect ratio can also be employed to estimate the validity of the results derived analytically in the previous section. In this "2D-situation" the dependence of the flow velocity (v_x) on the z-direction is neglected, which corresponds to the assumption that the microbeads are injected at half-height of the channel with no vertical sample dispersion. In the second step, which will be discussed in the next section, the dependence of v_x on the z-direction will be included, $v_x(y, z)$, with a certain vertical dispersion of the microbeads at the channel input (Δz_0) in order to mimic real experiments. This allows us to study the effect on the achievable SE of the vertical position and dispersion at the sample inlet, giving the opportunity to derive some interesting design rules. All the simulations were performed assuming the typical parameters corresponding to a water suspension of polystyrene microbeads (Table 5.1). Even in this case, all the numerical simulations were computed by means of custom MATLAB scripts. Specifically, the microparticles trajectories at the x- y (2D case) and x- y- z (3D case) coordinates as a function of time were derived using Eq. 5.4 and Eq. 5.8, thanks to the use of the "ODE45" MATLAB function. The sample trajectories were computed over a time vector of 2000 uniformly spaced points, whose time-step is related to the sample properties and microchannel geometry, as they impact on the time required by the particles to reach the channel center. To have a general idea, the calculation of each point appearing in the graphs from Figure 5.11 to Figure 5.13 required about 30 minutes of computation time on a 4-cores processor at 3.50 GHz and with 16 GB of RAM. The impact of different microchannel aspect ratios can be studied in two different ways: keeping one dimension fixed and changing the other one (for example fixed height and variable width), or by simultaneously changing both dimensions in order to maintain the cross-sectional area constant. In the following analysis, unless otherwise stated, the microfluidic channel area is kept fixed at 9×10^{-2} mm^2, which corresponds to a microchannel with a square cross-section having a side of 300 µm. It is worth underlying that the dependencies and trends derived for this specific choice of the area are of general validity.

The first step of the numerical simulations always consisted in the determination of the proper time-interval to be considered and of the appropriate temporal- and spatial-resolution. For each combination of the microchannel-microbeads system, different launch positions y_0 were considered and for each of them the corresponding SE was calculated, thus allowing to determine the best launch position y_0^*. The numerical study was initially performed to verify if the considerations reported in the previous section are still valid in the 2D-case. In order to prove the previously written consideration (i), in the 2D-numerical simulations different microbead populations characterized by a φ value different from that of standard polystyrene beads were considered. Figure 5.11 shows the y_0^* values, as a percentage of the channel width, as a function of the channel aspect ratio for four different microbead population pairs. The first pair is constituted by microparticles characterized by

a φ value equal to 98% and 102% of the nominal polystyrene φ-value in water, and it is therefore indicated as $\Delta\varphi = \pm 2\%$ in the legend (corresponding to the ΔA_r value in the previous section). In the exact same way, population-pairs with an increased difference of the acoustic contrast factor up to the $\Delta\varphi = \pm 20\%$ case were considered, corresponding to microparticle-populations characterized by a φ value equal to 80% and 120% of that of polystyrene microbeads in water. As reported in the 1D-system analysis, observing Figure 5.11 it can be noted that y_0^* does not depend on how large the microparticle property variations are, provided that the difference is not too pronounced. As it is clear analyzing the $\Delta\varphi = \pm 20\%$ case, if the φ variation becomes too big the y_0^* position may start to change, and this is due to the fact that the first-order approximation employed to derive Eq. 5.18 is not sufficient anymore. Nevertheless, as the most challenging acoustic separation situation is when microparticle populations with small differences are considered, this limitation is not particularly important for the here-reported analysis. It is even interesting to observe that the y_0^* value depends on the aspect ratio w/h of the channel cross-section, but it becomes almost constant for $w > 10h$, as the configuration approaches the 1D-system previously studied. Finally, it is remarkable to notice that the data used to realize Figure 5.11 are characterized by a ratio $\Delta y_0/R \approx 2.7$, which corresponds in Figure 5.10 to $y_0^* \approx 15\%$, perfectly matching the numerically computed optimal injection position for large aspect ratios ($w > 10h$) in the 2D-systems.

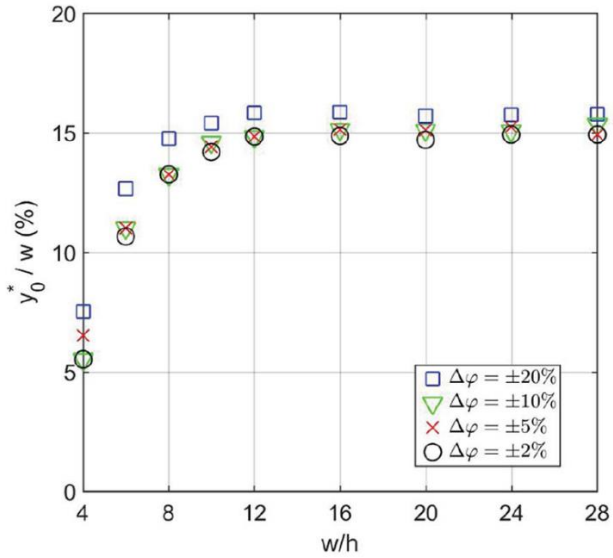

Figure 5.11: y_0^*/w (optimal injection position expressed as a percentage of the channel width) as a function of the microchannel aspect ratio [155]. *Parameters used for these numerical simulations: $R = 3.75\ \mu m$; $\varphi = 0.5$; $\Delta y_0 = 10\ \mu m$. The values reported in the legend correspond to the ΔA_r value in Eq. 5.19.*

The second step was the verification that the y_0^* value does not depend on the absolute value of φ. To prove this points, three different microparticle population pairs with significantly different values of the nominal φ factor (0.05, 0.5 and 5) were considered, while keeping $\Delta\varphi = \pm 5\%$. The results, graphically shown in Figure 5.12, confirm that no change of the y_0^* value results from the modification of the nominal φ of the populations, independently of the microchannel aspect ratio.

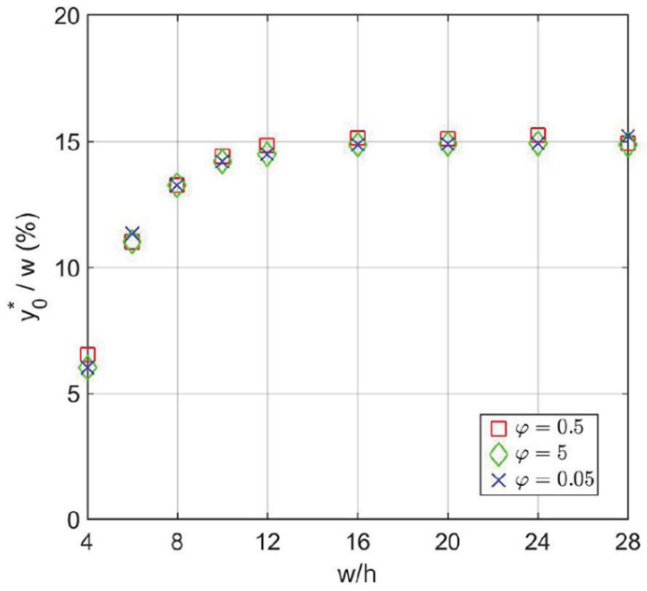

Figure 5.12: y_0^*/w as a function of the microchannel aspect ratio w/h numerically calculated for three different values of φ: 0.5, 5 and 0.05 [155]*. Other parameters used for these numerical simulations: $R = 3.75\ \mu m$; $\Delta\varphi = \pm 5\%$; $\Delta y_0 = 10\ \mu m$.*

The next step of the analysis was to verify the dependence of y_0^* on the Δy_0 and R parameters (i.e. consideration (iii) of the previous section). According to the previous discussion, we expect that the y_0^* value depends on $\Delta y_0/R$, but not on Δy_0 and R separately. In order to prove this dependence, the ideal y_0^* values for five different combinations of Δy_0 and R (schematically reported in Table 5.2) were compared, while maintaining constant the acoustic contrast factors of the two microbead populations ($\varphi = 0.5$; $\Delta\varphi = \pm 5\%$). Three different combinations of Δy_0 and R giving the same $\Delta y_0/R$ ratio (8/3), and two different combinations giving a four-times increase and decrease of the $\Delta y_0/R$ ratio (32/3 and 2/3, respectively) were selected.

Table 5.2: Simulation parameters employed to assess the dependence of y_0^* on Δy_0 and R.

Color	Symbol	Δy_0 [10^{-6} m]	R [10^{-6} m]	$\Delta y_0/R$
Blue	Triangle	10	3.75	2.67
Red	Diamond	20	7.5	2.67
Green	Square	5	1.875	2.67
Black	Circle	20	1.875	10.67
Cyan	Triangle	5	7.5	0.67

The results of the numerical simulations, displayed in Figure 5.13, show that in this case, as in the previously described 1D-system, the best launch position depends on $\Delta y_0/R$, and therefore it does not change if both values are multiplied by the same factor.

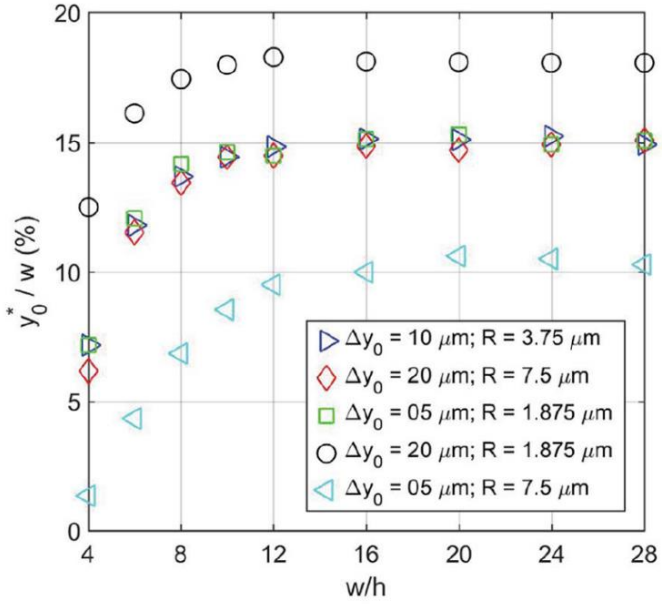

Figure 5.13: y_0^*/w as a function of the microchannel cross-section w/h in case different $\Delta y_0/R$ combinations are considered [155]*. The values of Δy_0 and R used for the numerical simulations are as reported in Table 5.2. Other simulation parameters: $\varphi = 0.5$; $\Delta\varphi = \pm 5\%$.*

To complete the numerical simulations campaign on the 2D-system it is possible to create a figure showing the overall dependence of y_0^* on $\Delta y_0/R$ and w/h, which are the only two factors influencing the y_0^* value. Figure 5.14 shows the results of the numerical simulations as a color map. The simulations were performed assuming a nominal $\varphi = 0.5$, $\Delta\varphi = \pm 5\%$ and $R = 5\ \mu m$, but the here-presented results have a much more general validity, as confirmed by the above reported discussion. In the same conditions the best value of SE (SE^*), achievable by a proper selection of the injection position, was also determined as a function of $\Delta y_0/R$ and w/h. The obtained results, shown in Figure 5.14 (b), highlight the benefits of using channels characterized by large aspect ratios and the

advantages resulting from the reduction of Δy_0, which can be accomplished, for example, by using a proper prefocusing section. The results of this study reveal two important points: (i) the importance of optimizing the injection position (y_0^*) to achieve the maximum SE value (SE^*) and (ii) that the y_0^* value, expressed as a percentage of w, depends only on the channel aspect ratio (w/h) and $\Delta y_0/R$ ratio, but not on other sample parameters. However, it must be pointed out that the entire analysis reported up to this point completely neglects the vertical dimension of the channel and the vertical sample distribution at the sample inlet.

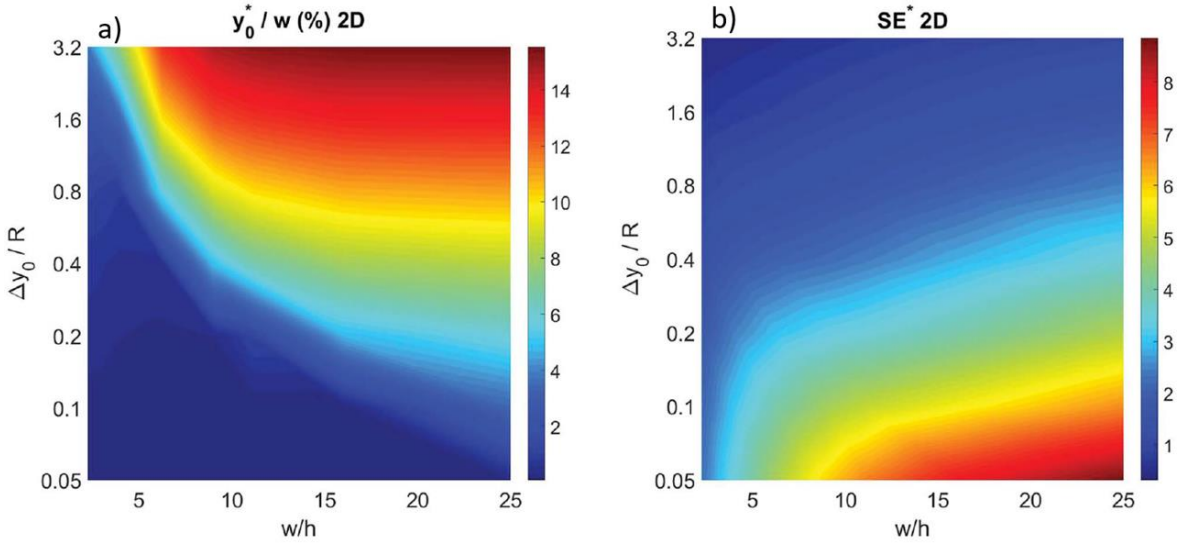

Figure 5.14: a) Optimal injection position (y_0^*) and b) corresponding separation efficiency (SE^*) as a function of $\Delta y_0/R$ and of the microchannel aspect ratio w/h in the 2D case [155].

5.4.3 Numerical simulations: extension to 3D-systems

In this last section a realistic 3D-system will be studied by considering also the effect played by the microchannel vertical dimension on the resulting SE. In particular, two important contributions will be included in the numerical simulations: the dependence of the flow velocity on the z-coordinate and the fact that the microparticle distribution is characterized by a non-zero dimension also along the z-direction. As a first step, a proper redefinition of the SE parameter is required as microparticles flowing at different microchannel heights are characterized by different speeds. Therefore, even if a rectangular distribution of microparticles at the sample inlet is assumed, the positions occupied while flowing along the microchannel create a curved distribution of microparticles at any other section, as it is shown in Figure 5.15. As the goal of this study is to have a realistic estimation of the system performance, the cross-section of the "sample-extraction" outlet is assumed to have a rectangular shape, independently of the curved distributions corresponding to the microparticles positions. The definition of the SE

parameter is thus kept the same as in Eq. 5.13, and the effect of the curved microparticles distribution is accounted by redefining the BW and relative displacement $|D_1 - D_2|$ values (see Figure 5.15). Specifically, the BW parameter of each microparticle population is defined as the maximum distance (along the y-axis) between two microbeads, i.e. considering at each section along the x-direction the microbead closer to the channel wall (at $z = h/2$) and the one closer to the channel center (and closer to the channel floor). The relative displacement $|D_1 - D_2|$, representing the distance between the "centers" of the two microparticle distributions, is simply calculated as the distance between the centers of the two population-bands. It must be highlighted that, as it is clear observing Figure 5.15, selecting an injection height different from the channel center can only worsen the system performance. As a matter of fact, the flow velocity gradient becomes larger moving apart from the middle-height position and therefore the microparticles distribution becomes wider. Consequently, in the following analysis the impact of a vertical spreading Δz_0 is investigated while maintaining the center of the injection channel fixed at half height of the microchannel ($z = h/2$). Relatively to the Δz_0 parameter, it can be defined as a given percentage of the microchannel height or by its own value (in µm).

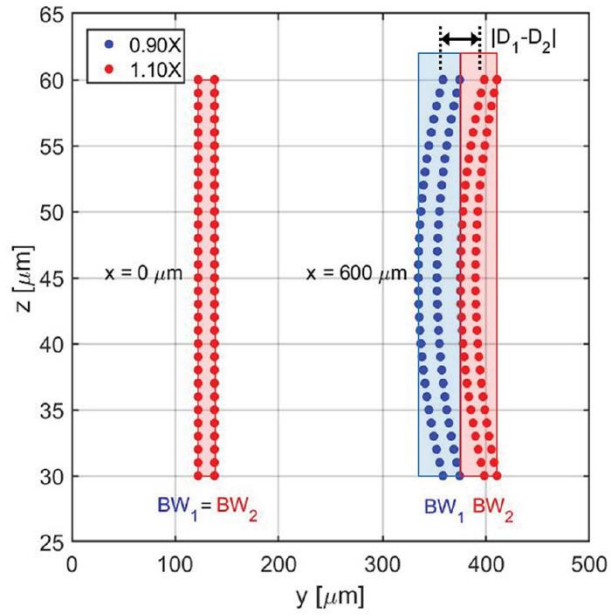

Figure 5.15: Schematic representation of microparticles acoustic separation in the 3D case [155]. *Parameters used in the simulation:* $w = 1000\ \mu m$; $h = 90\ \mu m$; *water medium; compressibility and density of polystyrene* ($\varphi = 0.5$); $\Delta\varphi = \pm 10\%$; $R = 5\ \mu m$; $\Delta y_0 = 8\ \mu m$; $\Delta z_0 = 15\ \mu m$.

In order to be consistent with the previously reported study, the case of a vertical spreading Δz_0 defined as a fixed percentage of the microchannel height is initially analyzed. In particular, a Δz_0 equal to 5% of the microchannel height is initially considered, while keeping all the other parameters set as for the final 2D numerical simulations: nominal $\varphi =$

0.5, $\Delta\varphi = \pm 5\%$ and $R = 5\ \mu m$. As for the 2D-system, both the optimal launch position y_0^* and the corresponding separation efficiency SE^* were computed as a function of the channel aspect ratio w/h and $\Delta y_0/R$ ratio. The results, shown in Figure 5.16, reveal two partially surprising findings: the y_0^* obtained in the 3D case is exactly the same as the one resulting from the 2D approximation and even the SE^* matches the one obtained in the 2D configuration, once properly rescaled by a constant factor. These results can be explained considering that the presence of a vertical spreading has as a result the presence of microparticles flowing at different heights, where the flow velocity is simply scaled (by a factor smaller than 1) with respect to the flow velocity at half height of the channel. As no distortion of the velocity profile is introduced, the y_0^* value for microparticles flowing at half height of the channel and for those flowing at any distance from the channel bottom is the same, under the assumption that the microparticles interaction with the channel bottom surface can be neglected. Consequently, even simulations performed using a larger vertical spreading (e.g. Δz_0 equal to 10% or 15%) would give the same results and therefore do not add any additional information.

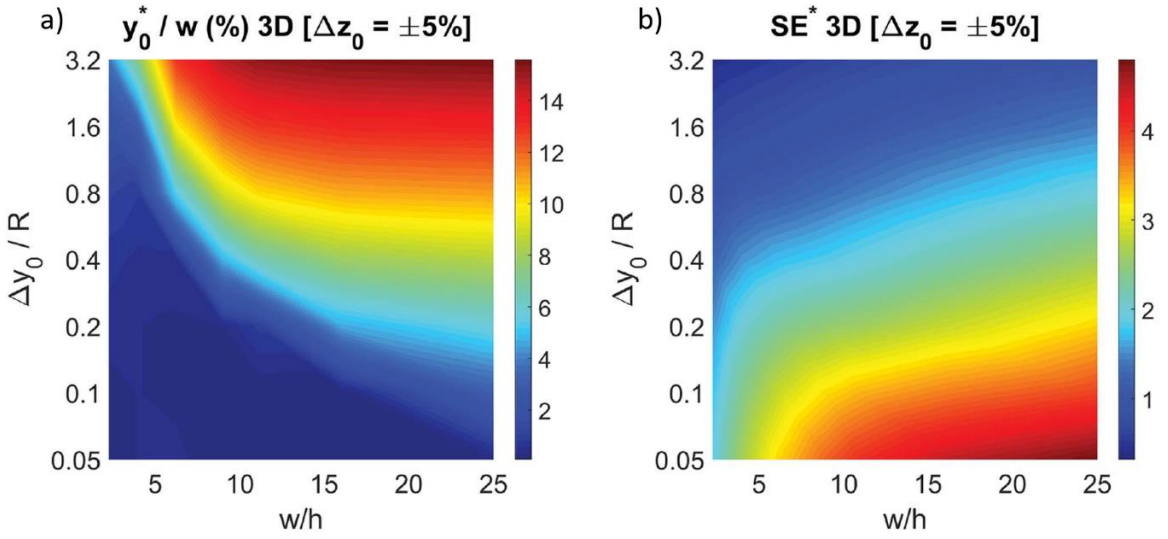

Figure 5.16: Assume the microbeads having a certain vertical distribution around the half height of the microchannel. The vertical spread is set to $\pm 5\%$ of the microchannel height h. a) Best injection position y_0^* as a function of the ratio $\Delta y_0/R$ and w/h in the 3D case. b) Corresponding value of SE^* as a function of the ratio $\Delta y_0/R$ and w/h in the 3D case [155].

The results reported in Figure 5.16 b) show that even a small vertical spreading can have a strong effect on the achievable SE^* when microchannels with high aspect ratio are considered: as an example, a 5% vertical spreading in a microchannel with an aspect ratio of 25 corresponds to a Δz_0 as small as $\pm 3\ \mu m$ and results in a significant SE^* reduction almost by a factor of 2. Conversely, the use of microchannels characterized by a smaller aspect ratio, although yielding a lower SE^* value in the ideal situation corresponding to

$\Delta z_0 = 0$, is expected to be significantly more tolerant to the sample vertical spreading. The next step was the study of the performance of microchannels with different aspect ratios in the situation of a fixed vertical spreading Δz_0 equal to $\pm 5\ \mu m$ and $\pm 10\ \mu m$. The y_0^* color maps calculated in these conditions do not bring any relevant information with respect to the one shown in Figure 5.16 a) and are therefore not reported. On the other side, it is interesting to observe the results shown in Figure 5.17, reporting SE^* in the above described conditions of a fixed Δz_0 value. The two color maps show that, once $\Delta y_0/R$ and Δz_0 are given, it is possible to determine the ideal microchannel cross-section and hence the achievable SE^*. It is interesting to observe that while in the 2D situation an aspect ratio as large as possible was desirable (see Figure 5.14 b)), in the 3D-system the presence of a non-negligible Δz_0 suggests the employment of higher microchannels, in order to mitigate the impact of the sample vertical spreading. In conclusion, the achievement of a high separation efficiency requires to find a trade-off between the mitigation of horizontal and vertical sample spreading, resulting in a non-obvious dependence of the ideal aspect ratio on both $\Delta y_0/R$ and Δz_0.

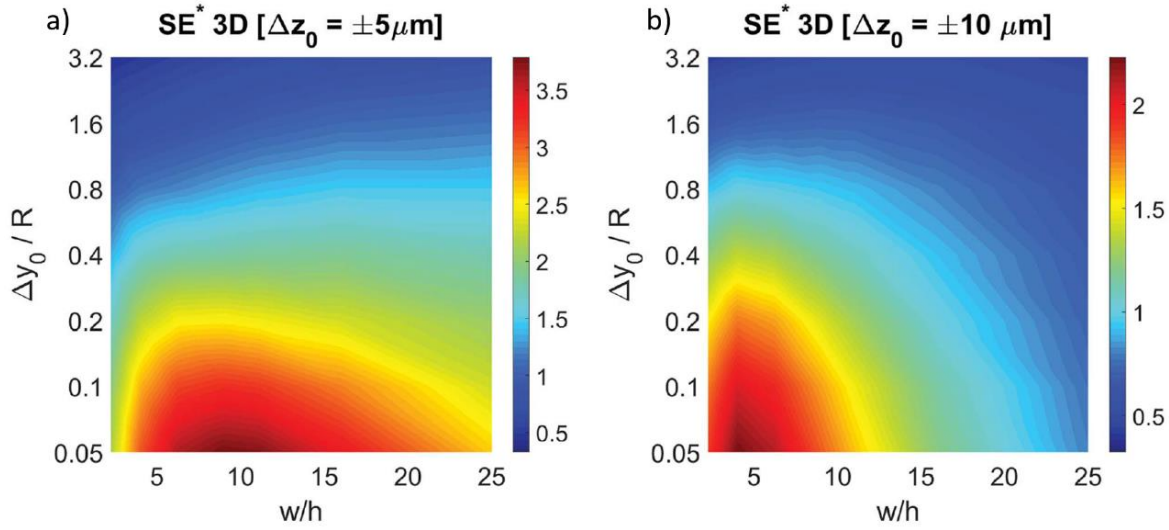

Figure 5.17: a) Assume the microbeads having a certain vertical distribution around the half height of the microchannel. The vertical spread is equal to $\pm 5\ \mu m$. SE^* as a function of the ratio $\Delta y_0/R$ and of w/h in the 3D case. b) Assume the microbeads having a certain vertical distribution around the half height of the microchannel. The vertical spread is equal to $\pm 10\ \mu m$. SE^* as a function of the ratio $\Delta y_0/R$ and of w/h in the 3D case [155].

In addition, it is important to mention that in the above reported analysis only the acoustic radiation force, which is applied on the flowing microbeads due to the sound-waves scattering, was considered, whereas the acoustic streaming effect and the related drag-force were completely neglected. According to the study performed by Muller et

al. [67], it is possible to demonstrate that in order to neglect the acoustic streaming effect, the particle radius must exceed by a few times the boundary-layer thickness δ:

$$R > \sqrt{\frac{9\Psi}{\varphi}}\delta \tag{5.22}$$

where Ψ is a factor related to the channel geometry and that in case of planar walls is equal to $3/8$. After some simple mathematical passages, this condition can be expressed as a limitation on the channel width w, given by the following equation:

$$w < \frac{4\rho\pi c_0}{27\eta}R^2\varphi \tag{5.23}$$

where η is the dynamic viscosity of the fluid, ρ is the fluid density and c_0 is the sound-wave velocity in the fluid. Considering for example cells characterized by $\varphi = 0.15$ and $R = 3\ \mu m$, the maximum microchannel width allowing to neglect the acoustic streaming effect is $w \approx 1000\ \mu m$, which may therefore set a limit on the achievable channel aspect ratio w/h.

In conclusion, it was shown that the optimal sample injection position depends on different parameters (the aspect ratio of the microchannel, the cross-section occupied by the particles distribution at the sample inlet and the radius of the particle). The optimization approach discussed in this chapter allowed finding interesting design rules, which can be applied to free-flow acoustofluidic separation devices independently of the presence or absence of pre-focusing strategies. It must be noted that thanks to a proper optimization of the sample injection point, high SE values can be obtained even if no prefocusing techniques are employed. This consideration allows a significant simplification of the design and operation of the acoustofluidic systems.

Conclusions

The main objective of this thesis has been the realization of an on-chip optical microrheometer conceived for measuring a wide range of materials (from simple Newtonian fluids and soft gels to stiffer materials) in their linear and nonlinear rheological regimes. Besides that, during my PhD activity I worked on a minor project concerning the theoretical study, by means of numerical simulations, of the separation efficiency achievable in acoustofluidic systems.

Three aspects were mainly considered:

1. The realization of an integrated microrheometer for shooting microrheology and the characterization of the Newtonian to non-Newtonian crossover of a DNA hydrogel.
2. The development of an integrated microrheometer for oscillatory microrheology able to characterize the viscoelastic properties of materials at different frequencies, temperatures and optical forces.
3. The theoretical study of the acoustofluidic separation of microparticles and the impact of different parameters on the achievable separation efficiency in order to derive useful design rules for the system optimization.

Regarding the first research line, the aim was the realization of an integrated optical microrheometer able to overcome the limitations of microscope-based single-beam optical tweezers (limited force range, need for optical alignment and lack of integration of optical and microfluidic parts). In the framework of a collaboration between my group, the Fastgroup and the Complex Fluids and Molecular Biophysics group of the University of Milan, we proposed an integrated optofluidic microrheometer based on a dual beam laser trap geometry. The device consists of an optofluidic chip fabricated on a glass substrate by direct inscription of facing optical waveguides in a commercial microfluidic chip. Thanks to the optical power emitted by two facing waveguides it is possible to trap and actively move a microbead in the fluid under test. By monitoring the movement of the microbead it is then possible to infer the rheological properties of the surrounding medium. The trapping position of the microbead can be controlled with high precision and stability thanks to the monolithic integration of the device. Moreover, this system allows obtaining higher optical forces when compared to conventional single-beam optical tweezers. The adopted technique consists in applying a step optical force on a microbead, which moves in the surrounding medium, thereby imposing a stress on it. In particular, the on-chip microrheometer was calibrated by performing experiments on water and validated by measuring water-glycerol mixtures at different concentrations. As a second step, the

viscosity of non-Newtonian fluids has been measured. In particular, the characterization of a DNA hydrogel provided a significant insight into the complex viscous behavior of network forming systems. The most important finding of the measurement campaign was the experimental observation that the transition from Newtonian to non-Newtonian behavior (strong shear thinning viscosity) of this model transient network takes place through a continuous set of power-law fluid regimes. The optical shooting procedure was then successfully employed for performing creep-recovery tests of yield stress fluids, whose experimental characterization is difficult to be carried out with conventional single-beam optical tweezers due to the high forces required to study these materials.

The second activity was dedicated to the realization of an integrated microrheometer for oscillatory microrheology in order to characterize the viscoelastic properties of materials in the frequency domain. The microrheometer was realized by connecting a custom Mach-Zehnder optical modulator to the optofluidic chip. Thanks to the actuation of the optical modulator it was possible to sinusoidally oscillate the trapped microbead and consequently retrieve the viscoelastic properties of the material under test at different oscillation frequencies. The integrated device allowed performing active microrheological measurements in the frequency range from 0.01 Hz to 10 Hz with temperature setting capability. The microrheometer was validated by performing oscillatory measurements of aqueous worm-like micellar solutions, at different concentrations and temperatures, and comparing the obtained results with those acquired using a conventional rheometer. Although only the validation of the oscillatory microrheometer has been reported, the proposed device could be employed to carry out stress-controlled active measurements, both in linear and nonlinear regime, on bio-based or bio-inspired materials. In conclusion, the precise control and wide range of achievable optical forces ensure a flexible use of the microrheometer, both in the optical shooting and oscillatory configurations, thus opening the way to the realization of a miniaturized, automatized and fully-integrated device.

As a minor project, a numerical investigation regarding the acoustic separation of micro-objects in acoustofluidic systems was carried out. Understanding the impact of different parameters on the achievable separation efficiency is the starting point to design and realize better acoustofluidic systems, as well as to further improve the device performance. The effect of many factors was analyzed, including extrinsic parameters (related to the acoustofluidic system design and operation: channel width, sample-launch position in the channel and acoustic energy density) and intrinsic parameters (samples' density, compressibility and diameter). This theoretical study highlighted some important results. In particular, it was shown that the microchannel width is a key factor for acoustofluidic separation (larger channel yielding a higher separation efficiency) and that, differently from the commonly exploited configurations, the separation efficiency can be

improved by injecting the sample in a position relatively distant from the channel border. Specifically, it was demonstrated by means of numerical simulations that the best sample injection position (i.e. the injection position yielding the maximum separation efficiency for a given configuration) depends on different parameters (the aspect ratio of the microchannel, the cross section occupied by the microparticles distribution at the sample inlet and the radius of the microparticles). Taking into account all these relations, it is possible to carefully optimize the acoustofluidic system even in the challenging situation where the micro-objects to be separated are characterized by a small deviation of their intrinsic properties from the other micro-objects flowing along the microchannel. In conclusion, the optimization method developed in this thesis allowed to derive interesting design rules that can be applied to free-flow acoustofluidic separation systems independently on the presence or absence of pre-focusing stages.

Bibliography

1. D. J. Beebe, G. A. Mensing, and G. M. Walker, "Physics and applications of microfluidics in biology," Annu. Rev. Biomed. Eng. **4**, 261–286 (2002).

2. D. L. Polla, "BioMEMS applications in medicine," in *MHS2001. Proceedings of 2001 International Symposium on Micromechatronics and Human Science (Cat. No. 01TH8583)* (IEEE, 2001), pp. 13–15.

3. K. Ohno, K. Tachikawa, and A. Manz, "Microfluidics: applications for analytical purposes in chemistry and biochemistry," Electrophoresis **29**, 4443–4453 (2008).

4. T. A. Waigh, "Microrheology of complex fluids," Reports Prog. Phys. (2005).

5. T. A. Waigh, "Advances in the microrheology of complex fluids," Reports Prog. Phys. **79**, 74601 (2016).

6. F. C. MacKintosh and C. F. Schmidt, "Microrheology," Curr. Opin. Colloid Interface Sci. **4**, 300–307 (1999).

7. G. M. Whitesides, "The origins and the future of microfluidics," Nature **442**, 368 (2006).

8. P. Abgrall and A. M. Gue, "Lab-on-chip technologies: making a microfluidic network and coupling it into a complete microsystem—a review," J. micromechanics microengineering **17**, R15 (2007).

9. D. Figeys and D. Pinto, "Lab-on-a-chip: a revolution in biological and medical sciences.," (2000).

10. R. B. Fair, "Digital microfluidics: is a true lab-on-a-chip possible?," Microfluid. Nanofluidics **3**, 245–281 (2007).

11. R. B. Fair, A. Khlystov, T. D. Tailor, V. Ivanov, R. D. Evans, V. Srinivasan, V. K. Pamula, M. G. Pollack, P. B. Griffin, and J. Zhou, "Chemical and biological applications of digital-microfluidic devices," IEEE Des. Test Comput. **24**, 10–24 (2007).

12. Y. Zheng, J. Nguyen, Y. Wei, and Y. Sun, "Recent advances in microfluidic techniques for single-cell biophysical characterization," Lab Chip **13**, 2464–2483 (2013).

13. J. Chen, J. Li, and Y. Sun, "Microfluidic approaches for cancer cell detection, characterization, and separation," Lab Chip **12**, 1753–1767 (2012).

14. T. A. Duncombe, A. M. Tentori, and A. E. Herr, "Microfluidics: reframing biological enquiry," Nat. Rev. Mol. Cell Biol. **16**, 554 (2015).

15. J. Guck, R. Ananthakrishnan, H. Mahmood, T. J. Moon, C. C. Cunningham, and J. Käs, "The Optical Stretcher: A Novel Laser Tool to Micromanipulate Cells," Biophys. J. **81**, 767–784 (2001).

16. J. Guck, S. Schinkinger, B. Lincoln, F. Wottawah, S. Ebert, M. Romeyke, D. Lenz, H. M.

Erickson, R. Ananthakrishnan, D. Mitchell, and others, "Optical deformability as an inherent cell marker for testing malignant transformation and metastatic competence," Biophys. J. **88**, 3689–3698 (2005).

17. T. Yang, F. Bragheri, G. Nava, I. Chiodi, C. Mondello, R. Osellame, K. Berg-Sørensen, I. Cristiani, and P. Minzioni, "A comprehensive strategy for the analysis of acoustic compressibility and optical deformability on single cells," Sci. Rep. **6**, 23946 (2016).

18. P. Minzioni, R. Osellame, C. Sada, S. Zhao, F. G. Omenetto, K. B. Gylfason, T. Haraldsson, Y. Zhang, A. Ozcan, A. Wax, and others, "Roadmap for optofluidics," J. Opt. **19**, 93003 (2017).

19. M. M. Crane, K. Chung, J. Stirman, and H. Lu, "Microfluidics-enabled phenotyping, imaging, and screening of multicellular organisms," Lab Chip **10**, 1509–1517 (2010).

20. B. Kuswandi, J. Huskens, and W. Verboom, "Optical sensing systems for microfluidic devices: a review," Anal. Chim. Acta **601**, 141–155 (2007).

21. Y.-C. Tung, N.-T. Huang, B.-R. Oh, B. Patra, C.-C. Pan, T. Qiu, P. K. Chu, W. Zhang, and K. Kurabayashi, "Optofluidic detection for cellular phenotyping," Lab Chip **12**, 3552–3565 (2012).

22. A. A. Yanik, M. Huang, O. Kamohara, A. Artar, T. W. Geisbert, J. H. Connor, and H. Altug, "An optofluidic nanoplasmonic biosensor for direct detection of live viruses from biological media," Nano Lett. **10**, 4962–4969 (2010).

23. J. Guo, X. Liu, K. Kang, Y. Ai, Z. Wang, and Y. Kang, "A compact optofluidic cytometer for detection and enumeration of tumor cells," J. Light. Technol. **33**, 3433–3438 (2015).

24. C. C. Stemple, S. V Angus, T. S. Park, and J.-Y. Yoon, "Smartphone-based optofluidic lab-on-a-chip for detecting pathogens from blood," J. Lab. Autom. **19**, 35–41 (2014).

25. A. Greenbaum, W. Luo, T.-W. Su, Z. Göröcs, L. Xue, S. O. Isikman, A. F. Coskun, O. Mudanyali, and A. Ozcan, "Imaging without lenses: achievements and remaining challenges of wide-field on-chip microscopy," Nat. Methods **9**, 889 (2012).

26. S. O. Isikman, W. Bishara, O. Mudanyali, I. Sencan, T.-W. Su, D. K. Tseng, O. Yaglidere, U. Sikora, and A. Ozcan, "Lensfree on-chip microscopy and tomography for biomedical applications," IEEE J. Sel. Top. Quantum Electron. **18**, 1059–1072 (2011).

27. X. Cui, L. M. Lee, X. Heng, W. Zhong, P. W. Sternberg, D. Psaltis, and C. Yang, "Lensless high-resolution on-chip optofluidic microscopes for Caenorhabditis elegans and cell imaging," Proc. Natl. Acad. Sci. **105**, 10670–10675 (2008).

28. Y. Sung, N. Lue, B. Hamza, J. Martel, D. Irimia, R. R. Dasari, W. Choi, Z. Yaqoob, and P. So, "Three-dimensional holographic refractive-index measurement of continuously flowing cells in a microfluidic channel," Phys. Rev. Appl. **1**, 14002 (2014).

29. K. Mishra, D. van den Ende, and F. Mugele, "Recent developments in optofluidic lens technology," Micromachines **7**, 102 (2016).

30. K. Mishra, C. Murade, B. Carreel, I. Roghair, J. M. Oh, G. Manukyan, D. Van Den Ende, and F. Mugele, "Optofluidic lens with tunable focal length and asphericity," Sci. Rep. **4**, 6378 (2014).

31. A. Huebner, M. Srisa-Art, D. Holt, C. Abell, F. Hollfelder, A. J. Demello, and J. B. Edel, "Quantitative detection of protein expression in single cells using droplet microfluidics," Chem. Commun. 1218–1220 (2007).

32. B. Fan, X. Li, D. Chen, H. Peng, J. Wang, and J. Chen, "Development of microfluidic systems enabling high-throughput single-cell protein characterization," Sensors **16**, 232 (2016).

33. C. Dongre, J. Van Weerd, G. A. J. Besselink, R. van Weeghel, R. M. Vazquez, R. Osellame, G. Cerullo, M. Cretich, M. Chiari, and H. J. W. M. Hoekstra, "High-resolution electrophoretic separation and integrated-waveguide excitation of fluorescent DNA molecules in a lab on a chip," Electrophoresis **31**, 2584–2588 (2010).

34. C. Dongre, J. van Weerd, G. A. J. Besselink, R. M. Vazquez, R. Osellame, G. Cerullo, R. van Weeghel, H. H. van den Vlekkert, H. J. W. M. Hoekstra, and M. Pollnau, "Modulation-frequency encoded multi-color fluorescent DNA analysis in an optofluidic chip," Lab Chip **11**, 679–683 (2011).

35. A. Bamshad, A. Nikfarjam, and M. H. Sabour, "Capillary-based micro-optofluidic viscometer," Meas. Sci. Technol. **29**, 95901 (2018).

36. X. Zeng, K. Zhang, J. Pan, G. Chen, A.-Q. Liu, S.-K. Fan, and J. Zhou, "Chemiluminescence detector based on a single planar transparent digital microfluidic device," Lab Chip **13**, 2714–2720 (2013).

37. J.-L. He, D.-S. Wang, and S.-K. Fan, "Opto-microfluidic immunosensors: From colorimetric to plasmonic," Micromachines **7**, 29 (2016).

38. D. Sinton, "Energy: the microfluidic frontier," Lab Chip **14**, 3127–3134 (2014).

39. D. Erickson, D. Sinton, and D. Psaltis, "Optofluidics for energy applications," Nat. Photonics **5**, 583 (2011).

40. K. C. Neuman and S. M. Block, "Optical trapping," Rev. Sci. Instrum. **75**, 2787–2809 (2004).

41. A. Ashkin and J. M. Dziedzic, "Optical trapping and manipulation of viruses and bacteria," Science (80-.). **235**, 1517–1520 (1987).

42. A. Ashkin, "Forces of a single-beam gradient laser trap on a dielectric sphere in the ray optics regime," Biophys. J. **61**, 569–582 (1992).

43. A. Ashkin, "Optical trapping and manipulation of neutral particles using lasers," Proc. Natl. Acad. Sci. **94**, 4853–4860 (1997).

44. A. Ashkin, J. M. Dziedzic, J. E. Bjorkholm, and S. Chu, "Observation of a single-beam gradient force optical trap for dielectric particles," Opt. Lett. **11**, 288–290 (1986).

45. A. Ashkin, "Acceleration and trapping of particles by radiation pressure," Phys. Rev.

Lett. **24**, 156 (1970).

46. A. Ashkin, J. M. Dziedzic, and T. Yamane, "Optical trapping and manipulation of single cells using infrared laser beams," Nature **330**, 769 (1987).

47. L. Ferrara, E. Baldini, P. Minzioni, F. Bragheri, C. Liberale, E. Di Fabrizio, and I. Cristiani, "Experimental study of the optical forces exerted by a Gaussian beam within the Rayleigh range," J. Opt. **13**, 75712 (2011).

48. L. Novotny and B. Hecht, *Principles of Nano-Optics* (Cambridge university press, 2012).

49. T. Yang, F. Bragheri, and P. Minzioni, "A Comprehensive Review of Optical Stretcher for Cell Mechanical Characterization at Single-Cell Level," Micromachines **7**, 90 (2016).

50. E. Sidick, S. D. Collins, and A. Knoesen, "Trapping forces in a multiple-beam fiber-optic trap," Appl. Opt. **36**, 6423–6433 (1997).

51. G. Destgeer and H. J. Sung, "Recent advances in microfluidic actuation and micro-object manipulation via surface acoustic waves," Lab Chip **15**, 2722–2738 (2015).

52. J. Friend and L. Y. Yeo, "Microscale acoustofluidics: Microfluidics driven via acoustics and ultrasonics," Rev. Mod. Phys. **83**, 647 (2011).

53. H. Bruus, J. Dual, J. Hawkes, M. Hill, T. Laurell, J. Nilsson, S. Radel, S. Sadhal, and M. Wiklund, "Forthcoming Lab on a Chip tutorial series on acoustofluidics: Acoustofluidics—exploiting ultrasonic standing wave forces and acoustic streaming in microfluidic systems for cell and particle manipulation," Lab Chip **11**, 3579–3580 (2011).

54. H. Bruus, *Theoretical Microfluidics* (Oxford university press Oxford, 2008), Vol. 18.

55. D. J. Collins, A. Neild, and Y. Ai, "Highly focused high-frequency travelling surface acoustic waves (SAW) for rapid single-particle sorting," Lab Chip **16**, 471–479 (2016).

56. G. Nava, F. Bragheri, T. Yang, P. Minzioni, R. Osellame, I. Cristiani, and K. Berg-Sørensen, "All-silica microfluidic optical stretcher with acoustophoretic prefocusing," Microfluid. Nanofluidics **19**, 837–844 (2015).

57. J. Shi, H. Huang, Z. Stratton, Y. Huang, and T. J. Huang, "Continuous particle separation in a microfluidic channel via standing surface acoustic waves (SSAW)," Lab Chip **9**, 3354–3359 (2009).

58. C. Devendran, I. Gralinski, and A. Neild, "Separation of particles using acoustic streaming and radiation forces in an open microfluidic channel," Microfluid. Nanofluidics **17**, 879–890 (2014).

59. C. Devendran, N. R. Gunasekara, D. J. Collins, and A. Neild, "Batch process particle separation using surface acoustic waves (SAW): integration of travelling and standing SAW," RSC Adv. **6**, 5856–5864 (2016).

60. M. K. Tan, L. Y. Yeo, and J. R. Friend, "Rapid fluid flow and mixing induced in

microchannels using surface acoustic waves," EPL (Europhysics Lett. **87**, 47003 (2009).

61. X. Ding, J. Shi, S.-C. S. Lin, S. Yazdi, B. Kiraly, and T. J. Huang, "Tunable patterning of microparticles and cells using standing surface acoustic waves," Lab Chip **12**, 2491–2497 (2012).

62. C. E. Owens, C. W. Shields, D. F. Cruz, P. Charbonneau, and G. P. López, "Highly parallel acoustic assembly of microparticles into well-ordered colloidal crystallites," Soft Matter **12**, 717–728 (2016).

63. S. H. Kim, M. Antfolk, M. Kobayashi, S. Kaneda, T. Laurell, and T. Fujii, "Highly efficient single cell arraying by integrating acoustophoretic cell pre-concentration and dielectrophoretic cell trapping," Lab Chip **15**, (2015).

64. J. C. Brenker, D. J. Collins, H. Van Phan, T. Alan, and A. Neild, "On-chip droplet production regimes using surface acoustic waves," Lab Chip **16**, 1675–1683 (2016).

65. Y. N. Cheung, N. T. Nguyen, and T. N. Wong, "Droplet manipulation in a microfluidic chamber with acoustic radiation pressure and acoustic streaming," Soft Matter **10**, 8122–8132 (2014).

66. I. Leibacher, P. Reichert, and J. Dual, "Microfluidic droplet handling by bulk acoustic wave (BAW) acoustophoresis," Lab Chip **15**, (2015).

67. P. B. Muller, R. Barnkob, M. J. H. Jensen, and H. Bruus, "A numerical study of microparticle acoustophoresis driven by acoustic radiation forces and streaming-induced drag forces," Lab Chip **12**, 4617–4627 (2012).

68. A. Lenshof, M. Evander, T. Laurell, and J. Nilsson, "Acoustofluidics 5: Building microfluidic acoustic resonators," Lab Chip **12**, 684–695 (2012).

69. R. Barnkob and H. Bruus, "Acoustofluidics: theory and simulation of radiation forces at ultrasound resonances in microfluidic devices," in *Proceedings of Meetings on Acoustics 157ASA* (ASA, 2009), Vol. 6, p. 20001.

70. K. Sugioka, J. Xu, D. Wu, Y. Hanada, Z. Wang, Y. Cheng, and K. Midorikawa, "Femtosecond laser 3D micromachining: a powerful tool for the fabrication of microfluidic, optofluidic, and electrofluidic devices based on glass," Lab Chip **14**, 3447–3458 (2014).

71. R. Osellame, G. Cerullo, and R. Ramponi, *Femtosecond Laser Micromachining: Photonic and Microfluidic Devices in Transparent Materials* (Springer Science & Business Media, 2012), Vol. 123.

72. F. Bragheri, L. Ferrara, N. Bellini, K. C. Vishnubhatla, P. Minzioni, R. Ramponi, R. Osellame, and I. Cristiani, "Optofluidic chip for single cell trapping and stretching fabricated by a femtosecond laser," J. Biophotonics **3**, 234–243 (2010).

73. K. Sugioka and Y. Cheng, "Femtosecond laser processing for optofluidic fabrication," Lab Chip **12**, 3576–3589 (2012).

74. F. He, Y. Liao, J. Lin, J. Song, L. Qiao, Y. Cheng, and K. Sugioka, "Femtosecond laser

fabrication of monolithically integrated microfluidic sensors in glass," Sensors **14**, 19402–19440 (2014).

75. T. Somer and H. J. Meiselman, "Disorders of blood viscosity," Ann. Med. **25**, 31–39 (1993).

76. G. Tomaiuolo, "Biomechanical properties of red blood cells in health and disease towards microfluidics," Biomicrofluidics **8**, 51501 (2014).

77. P. Coussot, *Rheophysics* (Springer, 2016).

78. P. Kelly, "Solid mechanics part I: An introduction to solid mechanics," A Creat. Commons Attrib. Mt. View, CA **94042**, (2013).

79. H. A. Barnes, J. F. Hutton, and K. Walters, *An Introduction to Rheology* (Elsevier, 1989).

80. K. Walters, "History of rheology," Hist. Philos. Sci. Technol. III 91 (2010).

81. M. Reiner, "The deborah number," Phys. Today **17**, 62 (1964).

82. C. D. Chapman and R. M. Robertson-Anderson, "Nonlinear microrheology reveals entanglement-driven molecular-level viscoelasticity of concentrated DNA," Phys. Rev. Lett. **113**, 1–5 (2014).

83. M. J. Taormina, E. A. Hay, and R. Parthasarathy, "Passive and active microrheology of the intestinal fluid of the larval zebrafish," Biophys. J. **113**, 957–965 (2017).

84. A. Rigato, A. Miyagi, S. Scheuring, and F. Rico, "High-frequency microrheology reveals cytoskeleton dynamics in living cells," Nat. Phys. **13**, 771 (2017).

85. P. Cicuta and A. M. Donald, "Microrheology: A review of the method and applications," Soft Matter **3**, 1449–1455 (2007).

86. G. Pesce, L. Selvaggi, A. Caporali, A. C. De Luca, A. Puppo, G. Rusciano, and A. Sasso, "Mechanical changes of living oocytes at maturation investigated by multiple particle tracking," Appl. Phys. Lett. **95**, 93702 (2009).

87. L. Selvaggi, M. Salemme, C. Vaccaro, G. Pesce, G. Rusciano, A. Sasso, C. Campanella, and R. Carotenuto, "Multiple-particle-tracking to investigate viscoelastic properties in living cells," Methods **51**, 20–26 (2010).

88. P. Edera, D. Bergamini, V. Trappe, F. Giavazzi, and R. Cerbino, "Differential dynamic microscopy microrheology of soft materials: A tracking-free determination of the frequency-dependent loss and storage moduli," Phys. Rev. Mater. **1**, 73804 (2017).

89. T. G. Mason and D. A. Weitz, "Optical measurements of frequency-dependent linear viscoelastic moduli of complex fluids," Phys. Rev. Lett. **74**, 1250–1253 (1995).

90. J. Rother, H. Nöding, I. Mey, and A. Janshoff, "Atomic force microscopy-based microrheology reveals significant differences in the viscoelastic response between malign and benign cell lines," Open Biol. **4**, 140046 (2014).

91. J. Alcaraz, L. Buscemi, M. Grabulosa, X. Trepat, B. Fabry, R. Farré, and D. Navajas,

"Microrheology of human lung epithelial cells measured by atomic force microscopy," Biophys. J. **84**, 2071–2079 (2003).

92. T. Yang, Y. Chen, and P. Minzioni, "A review on optical actuators for microfluidic systems," J. Micromechanics Microengineering **27**, 123001 (2017).

93. P. Paiè, T. Zandrini, R. Vázquez, R. Osellame, and F. Bragheri, "Particle manipulation by optical forces in microfluidic devices," Micromachines **9**, 200 (2018).

94. R. Sarkar and V. V Rybenkov, "A guide to magnetic tweezers and their applications," Front. Phys. **4**, 48 (2016).

95. A. Yao, M. Tassieri, M. Padgett, and J. Cooper, "Microrheology with optical tweezers," Lab Chip **9**, 2568–2575 (2009).

96. D. Preece, R. Warren, R. M. L. Evans, G. M. Gibson, M. J. Padgett, J. M. Cooper, and M. Tassieri, "Optical tweezers: Wideband microrheology," J. Opt. **13**, (2011).

97. M. Tassieri, R. M. L. Evans, R. L. Warren, N. J. Bailey, and J. M. Cooper, "Microrheology with optical tweezers: data analysis," New J. Phys. **14**, 115032 (2012).

98. R. R. Brau, J. M. Ferrer, H. Lee, C. E. Castro, B. K. Tam, P. B. Tarsa, P. Matsudaira, M. C. Boyce, R. D. Kamm, and M. J. Lang, "Passive and active microrheology with optical tweezers," J. Opt. A Pure Appl. Opt. **9**, (2007).

99. B. H. Blehm, A. Devine, J. R. Staunton, and K. Tanner, "In vivo tissue has non-linear rheological behavior distinct from 3D biomimetic hydrogels, as determined by AMOTIV microscopy," Biomaterials **83**, 66–78 (2016).

100. M. Tassieri, F. Del Giudice, E. J. Robertson, N. Jain, B. Fries, R. Wilson, A. Glidle, F. Greco, P. A. Netti, and P. L. Maffettone, "Microrheology with Optical Tweezers: Measuring the relative viscosity of solutions 'at a glance,'" Sci. Rep. **5**, 8831 (2015).

101. F. Ziemann, J. Rädler, and E. Sackmann, "Local measurements of viscoelastic moduli of entangled actin networks using an oscillating magnetic bead micro-rheometer," Biophys. J. **66**, 2210–2216 (1994).

102. T. Yang, G. Nava, V. Vitali, F. Bragheri, R. Osellame, T. Bellini, I. Cristiani, and P. Minzioni, "Integrated Optofluidic Chip for Low-Volume Fluid Viscosity Measurement," Micromachines **8**, 65 (2017).

103. G. Nava, T. Yang, V. Vitali, P. Minzioni, I. Cristiani, F. Bragheri, R. Osellame, L. Bethge, S. Klussmann, E. M. Paraboschi, and others, "Newtonian to non-newtonian fluid transition of a model transient network," Soft Matter **14**, 3288–3295 (2018).

104. G. Pesce, A. C. De Luca, G. Rusciano, P. A. Netti, S. Fusco, and A. Sasso, "Microrheology of complex fluids using optical tweezers: a comparison with macrorheological measurements," J. Opt. A Pure Appl. Opt. **11**, 34016 (2009).

105. N. Bellini, F. Bragheri, I. Cristiani, J. Guck, R. Osellame, and G. Whyte, "Validation and perspectives of a femtosecond laser fabricated monolithic optical stretcher.," Biomed. Opt. Express **3**, 2658–68 (2012).

106. K. Svoboda and S. M. Block, "Biological applications of optical forces," Annu.Rev.Biophys.Biomol.Struct. **23**, 247–285 (1994).

107. N. S. Cheng, "Formula for the viscosity of a glycerol-water mixture," Ind. Eng. Chem. Res. **47**, 3285–3288 (2008).

108. D. T. N. Chen, Q. Wen, P. A. Janmey, J. C. Crocker, and A. G. Yodh, "Rheology of soft materials," Annu. Rev. Condens. Matter Phys. **1**, 301–322 (2010).

109. P. Sollich, "Rheological constitutive equation for a model of soft glassy materials," Phys. Rev. E **58**, 738 (1998).

110. M. Guvendiren, H. D. Lu, and J. A. Burdick, "Shear-thinning hydrogels for biomedical applications," Soft Matter **8**, 260–272 (2012).

111. B. Kronberg and B. Lindman, *Surfactants and Polymers in Aqueous Solution* (John Wiley & Sons Ltd., Chichester, 2003).

112. R. D. Jenkins, C. A. Silebi, and M. S. El-Aasser, "Steady-shear and linear-viscoelastic material properties of model associative polymer solutions," in (ACS Publications, 1991).

113. T. Annable, R. Buscall, R. Ettelaie, and D. Whittlestone, "The rheology of solutions of associating polymers: Comparison of experimental behavior with transient network theory," J. Rheol. (N. Y. N. Y). **37**, 695–726 (1993).

114. I. Kunita, K. Sato, Y. Tanaka, Y. Takikawa, H. Orihara, and T. Nakagaki, "Shear banding in an F-actin solution," Phys. Rev. Lett. **109**, 248303 (2012).

115. R. E. Buxbaum, T. Dennerll, and S. Weiss, "F-actin and microtubule suspensions as indeterminate fluids," Science (80-.). **235**, 1511–1514 (1987).

116. B. Huber, M. Harasim, B. Wunderlich, M. Kröger, and A. R. Bausch, "Microscopic origin of the non-Newtonian viscosity of semiflexible polymer solutions in the semidilute regime," ACS Macro Lett. **3**, 136–140 (2014).

117. B. J. Gold, C. H. Hövelmann, N. Lühmann, W. Pyckhout-Hintzen, A. Wischnewski, and D. Richter, "The microscopic origin of the rheology in supramolecular entangled polymer networks," J. Rheol. (N. Y. N. Y). **61**, 1211–1226 (2017).

118. D. Xu and S. L. Craig, "Strain hardening and strain softening of reversibly cross-linked supramolecular polymer networks," Macromolecules **44**, 7478–7488 (2011).

119. S. Biffi, R. Cerbino, F. Bomboi, E. M. Paraboschi, R. Asselta, F. Sciortino, and T. Bellini, "Phase behavior and critical activated dynamics of limited-valence DNA nanostars," Proc. Natl. Acad. Sci. **110**, 15633–15637 (2013).

120. J. SantaLucia Jr and D. Hicks, "The thermodynamics of DNA structural motifs," Annu. Rev. Biophys. Biomol. Struct. **33**, 415–440 (2004).

121. S. Biffi, R. Cerbino, G. Nava, F. Bomboi, F. Sciortino, and T. Bellini, "Equilibrium gels of low-valence DNA nanostars: a colloidal model for strong glass formers," Soft Matter **11**, 3132–3138 (2015).

122. W. B. Russel, W. B. Russel, D. A. Saville, and W. R. Schowalter, *Colloidal Dispersions* (Cambridge university press, 1991).

123. R. P. Chhabra and J. F. Richardson, "Non-newtonian fluid behaviour. Non-newtonian flow and applied rheology," (2008).

124. M. J. Whitney and G. J. Rodin, "Force–velocity relationships for rigid bodies translating through unbounded shear-thinning power-law fluids," Int. J. Non. Linear. Mech. **36**, 947–953 (2001).

125. R. G. Larson, *The Structure and Rheology of Complex Fluids* (Oxford university press New York, 1999), Vol. 150.

126. M. M. Cross, "Relation between viscoelasticity and shear-thinning behaviour in liquids," Rheol. Acta **18**, 609–614 (1979).

127. A. Ziegenhagen, "The very slow flow of a Powell-Eyring fluid around a sphere," Appl. Sci. Res. Sect. A **14**, 43–56 (1965).

128. M. M. Cross, "Polymer rheology: influence of molecular weight and polydispersity," J. Appl. Polym. Sci. **13**, 765–774 (1969).

129. G. Nava, M. Rossi, S. Biffi, F. Sciortino, and T. Bellini, "Fluctuating elasticity mode in transient molecular networks," Phys. Rev. Lett. **119**, 78002 (2017).

130. N. F. Dupuis, E. D. Holmstrom, and D. J. Nesbitt, "Single-molecule kinetics reveal cation-promoted DNA duplex formation through ordering of single-stranded helices," Biophys. J. **105**, 756–766 (2013).

131. I. Farnan and J. F. Stebbins, "The nature of the glass transition in a silica-rich oxide melt," Science (80-.). **265**, 1206–1209 (1994).

132. E. Guyon, J.-P. Hulin, L. Petit, and C. D. Mitescu, *Physical Hydrodynamics* (Oxford University Press, 2015).

133. N. J. Balmforth, I. A. Frigaard, and G. Ovarlez, "Yielding to stress: recent developments in viscoplastic fluid mechanics," Annu. Rev. Fluid Mech. **46**, 121–146 (2014).

134. P. Coussot, "Slow flows of yield stress fluids: yielding liquids or flowing solids?," Rheol. Acta **57**, 1–14 (2018).

135. D. Bonn, M. M. Denn, L. Berthier, T. Divoux, and S. Manneville, "Yield stress materials in soft condensed matter," Rev. Mod. Phys. **89**, 35005 (2017).

136. J. P. Rich, J. Lammerding, G. H. McKinley, and P. S. Doyle, "Nonlinear microrheology of an aging, yield stress fluid using magnetic tweezers," Soft Matter **7**, 9933–9943 (2011).

137. J. N. Wilking and T. G. Mason, "Optically driven nonlinear microrheology of gelatin," Phys. Rev. E **77**, 55101 (2008).

138. P. Coussot, "Yield stress fluid flows: A review of experimental data," J. Nonnewton. Fluid Mech. **211**, 31–49 (2014).

139. P. Coussot, H. Tabuteau, X. Chateau, L. Tocquer, and G. Ovarlez, "Aging and solid or liquid behavior in pastes," J. Rheol. (N. Y. N. Y). **50**, 975–994 (2006).

140. A. N. Beris, J. A. Tsamopoulos, R. C. Armstrong, and R. A. Brown, "Creeping motion of a sphere through a Bingham plastic," J. Fluid Mech. **158**, 219–244 (1985).

141. G. Zanchetta, S. Mirzaagha, V. Guida, F. Zonfrilli, M. Caggioni, N. Grizzuti, R. Pasquino, and V. Trappe, "Colloidal fibers as structurant for worm-like micellar solutions," Colloid Polym. Sci. **296**, 1379–1385 (2018).

142. N. De Meirleir, W. Broeckx, P. Van Puyvelde, and W. De Malsche, "Surfactant assisted emulsion crystallization of hydrogenated castor oil," Cryst. Growth Des. **15**, 635–641 (2015).

143. N. De Meirleir, L. Pellens, W. Broeckx, G. van Assche, and W. De Malsche, "The rheological properties of hydrogenated castor oil crystals," Colloid Polym. Sci. **292**, 2539–2547 (2014).

144. D. Yang and A. N. Hrymak, "Rheology of aqueous dispersions of hydrogenated castor oil," Appl. Rheol. **23**, 1–9 (2013).

145. F. Flamini, L. Magrini, A. S. Rab, N. Spagnolo, V. D'ambrosio, P. Mataloni, F. Sciarrino, T. Zandrini, A. Crespi, R. Ramponi, and others, "Thermally reconfigurable quantum photonic circuits at telecom wavelength by femtosecond laser micromachining," Light Sci. Appl. **4**, e354 (2015).

146. I. P. Kaminow and E. H. Turner, "Electrooptic light modulators," Appl. Opt. **5**, 1612–1628 (1966).

147. E. L. Wooten, K. M. Kissa, A. Yi-Yan, E. J. Murphy, D. A. Lafaw, P. F. Hallemeier, D. Maack, D. V Attanasio, D. J. Fritz, G. J. McBrien, and others, "A review of lithium niobate modulators for fiber-optic communications systems," IEEE J. Sel. Top. Quantum Electron. **6**, 69–82 (2000).

148. D. Ross, M. Gaitan, and L. E. Locascio, "Temperature measurement in microfluidic systems using a temperature-dependent fluorescent dye," Anal. Chem. **73**, 4117–4123 (2001).

149. T. L. Arbeloa, M. J. T. Estévez, F. L. Arbeloa, I. U. Aguirresacona, and I. L. Arbeloa, "Luminescence properties of rhodamines in water/ethanol mixtures," J. Lumin. **48**, 400–404 (1991).

150. S. Ebert, K. Travis, B. Lincoln, and J. Guck, "Fluorescence ratio thermometry in a microfluidic dual-beam laser trap," Opt. Express **15**, 15493–15499 (2007).

151. C. A. Dreiss, "Wormlike micelles: where do we stand? Recent developments, linear rheology and scattering techniques," Soft Matter **3**, 956–970 (2007).

152. M. E. Cates and S. J. Candau, "Statics and dynamics of worm-like surfactant micelles," J. Phys. Condens. Matter **2**, 6869 (1990).

153. C. Oelschlaeger, M. Schopferer, F. Scheffold, and N. Willenbacher, "Linear-to-branched micelles transition: A rheometry and diffusing wave spectroscopy (DWS)

study," Langmuir **25**, 716–723 (2008).

154. T. Yang, V. Vitali, and P. Minzioni, "Acoustofluidic separation: impact of microfluidic system design and of sample properties," Microfluid. Nanofluidics **22**, 44 (2018).

155. V. Vitali, T. Yang, and P. Minzioni, "Separation efficiency maximization in acoustofluidic systems: Study of the sample launch-position," RSC Adv. **8**, 38955–38964 (2018).

156. N. De Souza, "Single-cell methods," Nat. Methods **9**, 35 (2011).

157. P. Mishra, M. Hill, and P. Glynne-Jones, "Deformation of red blood cells using acoustic radiation forces," Biomicrofluidics **8**, 34109 (2014).

158. X. Ding, S.-C. S. Lin, M. I. Lapsley, S. Li, X. Guo, C. Y. Chan, I.-K. Chiang, L. Wang, J. P. McCoy, and T. J. Huang, "Standing surface acoustic wave (SSAW) based multichannel cell sorting," Lab Chip **12**, 4228–4231 (2012).

159. I. Iranmanesh, H. Ramachandraiah, A. Russom, and M. Wiklund, "On-chip ultrasonic sample preparation for cell based assays," RSC Adv. **5**, 74304–74311 (2015).

160. O. Jakobsson, M. Antfolk, and T. Laurell, "Continuous flow two-dimensional acoustic orientation of nonspherical cells," Anal. Chem. **86**, 6111–6114 (2014).

161. M. Ohlin, I. Iranmanesh, A. E. Christakou, and M. Wiklund, "Temperature-controlled MPa-pressure ultrasonic cell manipulation in a microfluidic chip," Lab Chip **15**, 3341–3349 (2015).

162. F. Guo, P. Li, J. B. French, Z. Mao, H. Zhao, S. Li, N. Nama, J. R. Fick, S. J. Benkovic, and T. J. Huang, "Controlling cell–cell interactions using surface acoustic waves," Proc. Natl. Acad. Sci. **112**, 43–48 (2015).

163. D. Hartono, Y. Liu, P. L. Tan, X. Y. S. Then, L.-Y. L. Yung, and K.-M. Lim, "On-chip measurements of cell compressibility via acoustic radiation," Lab Chip **11**, 4072–4080 (2011).

164. G. R. Goddard, C. K. Sanders, J. C. Martin, G. Kaduchak, and S. W. Graves, "Analytical performance of an ultrasonic particle focusing flow cytometer," Anal. Chem. **79**, 8740–8746 (2007).

165. F. Petersson, L. Åberg, A.-M. Swärd-Nilsson, and T. Laurell, "Free flow acoustophoresis: microfluidic-based mode of particle and cell separation," Anal. Chem. **79**, 5117–5123 (2007).

166. A. H. J. Yang and H. T. Soh, "Acoustophoretic sorting of viable mammalian cells in a microfluidic device," Anal. Chem. **84**, 10756–10762 (2012).

167. X. Ding, Z. Peng, S.-C. S. Lin, M. Geri, S. Li, P. Li, Y. Chen, M. Dao, S. Suresh, and T. J. Huang, "Cell separation using tilted-angle standing surface acoustic waves," Proc. Natl. Acad. Sci. **111**, 12992–12997 (2014).

168. M. Antfolk, C. Magnusson, P. Augustsson, H. Lilja, and T. Laurell, "Acoustofluidic, label-free separation and simultaneous concentration of rare tumor cells from white

blood cells.," Anal. Chem. **87**, 9322–8 (2015).

169. P. Augustsson, C. Magnusson, M. Nordin, H. Lilja, and T. Laurell, "Microfluidic, label-free enrichment of prostate cancer cells in blood based on acoustophoresis," Anal. Chem. **84**, 7954–7962 (2012).

170. M. Antfolk, C. Antfolk, H. Lilja, T. Laurell, and P. Augustsson, "A single inlet two-stage acoustophoresis chip enabling tumor cell enrichment from white blood cells," Lab Chip **15**, 2102–2109 (2015).

171. F. Garofalo, "Analytical characterization of particle kinematics and transverse dispersion in free-flow acoustophoretic devices," Microfluid. Nanofluidics **18**, 367–382 (2015).

172. F. Garofalo, "Quantifying acoustophoretic separation of microparticle populations by mean-and-covariance dynamics for Gaussians in mixture models," arXiv Prepr. arXiv1802.09790 (2018).

173. T. Kanazaki and T. Okada, "Two-dimensional particle separation in coupled acoustic-gravity-flow field vertically by composition and laterally by size," Anal. Chem. **84**, 10750–10755 (2012).

Publications

Peer-reviewed journal articles

1. R. Marchetti, **V. Vitali**, C. Lacava, I. Cristiani, G. Giuliani, V. Muffato, M. Fournier, S. Abrate, R. Gaudino, E. Temporiti, L. Carroll, and P. Minzioni*, "Low-Loss Micro-Resonator Filters Fabricated in Silicon by CMOS-Compatible Lithographic Techniques: Design and Characterization," *MDPI Applied Sciences*, 7(2), 174 (2017).
2. T. Yang, G. Nava, **V. Vitali**, F. Bragheri, R. Osellame, T. Bellini, I. Cristiani, and P. Minzioni*, "Integrated Optofluidic Chip for Low-Volume Fluid Viscosity Measurement," *Micromachines*, 8(3), 65 (2017).
3. R. Marchetti, **V. Vitali**, C. Lacava, I. Cristiani, B. Charbonnier, V. Muffato, M. Fournier, and P. Minzioni*, "Group-velocity dispersion in SOI-based channel waveguides with reduced-height," *Opt. Express*, 25(9), 9761 (2017).
4. T. Yang, **V. Vitali**, P. Minzioni*, "Acoustofluidic separation: impact of microfluidic system design and of sample properties," *Microfluidics and Nanofluidics*, 22(4), 44 (2018).
5. G. Nava, T. Yang, **V. Vitali**, P. Minzioni, I. Cristiani, F. Bragheri, R. Osellame, L. Bethge, S. Klussmann, E. M. Paraboschi, R. Asselta, and T. Bellini*, "Newtonian to non-Newtonian fluid transition of a model transient network," *Soft Matter*, 14(17), 3288 (2018).
6. **V. Vitali**, T. Yang, P. Minzioni*, "Separation Efficiency Maximization in Acoustofluidic Systems: study of the sample launch-position," *RSC Advances*, 8(68), 38955 (2018).
7. **V. Vitali**, G. Nava, G. Zanchetta, F. Bragheri, A. Crespi, R. Osellame, T. Bellini, I. Cristiani, and P. Minzioni*, "Integrated Optofluidic Chip for Oscillatory Microrheology," *submitted to Scientific Reports*.

Selected conference contributions

1. G. Nava*, T. Yang, **V. Vitali**, P. Minzioni, F. Bragheri, R. Osellame, and T. Bellini, "Newtonian to Non-Newtonian transition of a DNA transient network," Flowing matter 2017, 23-27 January 2017, Porto, Portugal.
2. R. Marchetti*, **V. Vitali**, C. Lacava, I. Cristiani, G. Giuliani, L. Adelmini, M. Fournier, and P. Minzioni, "Low-Loss Integrated Ring-Resonators Filters Realized by CMOS Fabrication Process," CLEO Europe 2017, 25-29 June 2017, Munich, Germany (CI-P.2).

3. T. Yang, **V. Vitali***, F. Bragheri, G. Nava, I. Chiodi, C. Mondello, R. Osellame, K. Berg-Sørensen, I. Cristiani, and P. Minzioni, "A Micro-Opto-Acousto-Fluidic Chip for Single Cell Mechanics Evaluation," CLEO Europe 2017, 25-29 June 2017, Munich, Germany (JSIII-1.4).
4. **V. Vitali***, G. Nava, T. Yang, F. Bragheri, R. Osellame, T. Bellini, I. Cristiani, and P. Minzioni, "Rheological Study of a DNA Transient Network by Optophoresis," CLEO Europe 2017, 25-29 June 2017, Munich, Germany (CL-4.5).
5. G. Nava*, T. Yang, **V. Vitali**, P. Minzioni, F. Bragheri, R. Osellame, and T. Bellini, "Onset of non-Newtonian viscosity in a DNA transient network," Liquids 2017, the 10th Liquid Matter Conference, 17-21 July 2017, Ljubljana, Slovenia (O9.6).
6. G. Nava, T. Yang, **V. Vitali**, F. Bragheri, R. Osellame, T. Bellini, and P. Minzioni*, "Optofluidic Microrheometer: study of viscosity behavior in transient networks," The 7th International Multidisciplinary Conference on Optofluidics 2017, 25-28 July 2017, Singapore (Session 16: Lab on a chip).
7. G. Zanchetta*, A. Corno, G. Nava, **V. Vitali**, F. Bragheri, R. Osellame, P. Minzioni, T. Bellini, "A microscale approach to yield stress materials: investigation of nonlinearity and yielding with an optofluidic micro-rheometer," The 5th International Soft Matter Conference (ISMC2019), 3-7 June 2019, Edinburgh, United Kingdom (PR17).
8. **V. Vitali***, G. Nava, G. Zanchetta, F. Bragheri, R. Osellame, T. Bellini, I. Cristiani, P. Minzioni, "Viscoelasticity Measurements by an Optofluidic Micro-Rheometer," CLEO Europe 2019, 23-27 June 2019, Munich, Germany (CH-P.27).